Synthesis and Characterization of Novel Two-Dimensional Materials

DISSERTATION

Presented in Partial Fulfillment of the Requirements for the Degree Doctor of Philosophy in the Graduate School of The Ohio State University

By

Justin R. Young

Graduate Program in Physics

The Ohio State University

2016

Dissertation Committee:

Professor Ezekiel Johnston-Halperin, Advisor

Professor Jay Gupta

Professor Nandini Trivedi

Professor Andrew Heckler

Abstract

As van der Waals layered materials are reduced from bulk crystals to monolayer sheets, a host of electronic, optoelectronic, and mechanical properties emerge which differ from those of the parent materials. This variety of materials properties—coupled to the atomically thin form factor—has attracted interest from all research sectors in the past decade due to potential applications in flexible, transparent, and low-power electronics. The two-dimensional nature of these materials makes them extremely sensitive to any surface interactions presenting both a unique opportunity to tune materials properties through surface modification and also a challenge whereby any surface contaminants can dramatically degrade the material quality. In this dissertation, we investigate and utilize this surface sensitivity in three different material systems.

First, we investigate electronic transport in germanane, a germanium analog of graphane, through a combination of electronic measurements on multi-layer crystals and finite-element modeling. In addition to doping this 2D material, we uncover a sensitivity of this transport to the presence of water-vapor, as well as an anisotropy between inter- and intra-layer resistivity of up to eleven orders of magnitude. The strong water sensitivity and weak inter-layer coupling mean that the transport in these samples is dominated by the

topmost layer and suggests that it may be possible to measure the effects of 2D materials in bulk materials by making electrical contact to only the topmost layer.

Second, we report on a templated MoS_2 growth technique wherein Mo is deposited onto atomically-stepped sapphire substrates through a SiN stencil with feature sizes down to 100 nm and subsequently sulfurized at high temperature. These films have a quality comparable to the best MoS_2 prepared by other methodologies, and the thickness of the resulting MoS_2 patterns can be tuned layer-by-layer by controlling the initial Mo deposition. This approach critically enables the creation of patterned single-layer MoS_2 films with pristine surfaces suitable for subsequent modification via functionalization and mechanical stacking. Further, we anticipate that this growth technique should be broadly applicable within the family of transition metal dichalcogenides.

Third and finally, we present progress toward understanding how local changes to graphene's crystal structure, such as defects, adatoms, and electromagnetic fields, affect the observable electronic and spin transport. We developed experimental methods to perform scanning probe and scanning tunneling microscopy with the simultaneous measurement of electrical transport in graphene Hall bar devices synthesized from graphene grown by chemical vapor deposition. Through the combination of these powerful experimental techniques, we plan to investigate the connection between localized surface modifications of graphene and the electronic and spin transport in these devices with eventual expansion of this technique to other 2D materials.

Dedication

Dedicated to the memory of my grandfather Victor R. Brown.

Acknowledgments

The past six years of my graduate school education have been an experience full of challenges I never would have been able to meet without the support of my family, friends, and colleagues.

First and foremost I would thank my advisor, Professor Ezekiel Johnston-Halperin. Without his guidance, resources, and support I never would have succeeded in this endeavor. He constantly pushed me to challenge myself and has worked hard to see that I succeeded not only in this endeavor, but also gain the tools necessary in any future endeavors I should choose to tackle. I am truly thankful for the opportunity to work in a lab that pursues high-quality, interesting, and relevant physics research.

I would also like to thank my many colleagues here at OSU. The past and present members of the Johnston-Halperin group: Yu-Sheng Ou, Mike Chilcote, Matt Sheffield, Andrew Franson, Ariel Wurm, Ethel Perez-Hoyos, Kurtis Wickey, Yi-Hsin Chiu, Howard Yu, Megan Harberts, and Dongkyun Ko have all helped to make my time at OSU a positive experience. Additionally, my many collaborators at OSU: Roland Kawakami, Joshua Goldberger, Jay Gupta, Andy Berger, Jyoti Katoch, Jinsong Xu, Beth Bushong, Sara Mueller, Nick Cultrara, Shishi Jiang, Grady Gambrel for the time and efforts they've spent

working together. And also to the undergraduates I've worked with: Matt Barone and Nicholas Crescimanno.

To Shawna Hollen, for consistently being an excellent example of what a scientist should be, and for always making herself available to explore a physics problem, or provide much needed perspective. I would also thank Jan Jacob of Hamburg, Germany for hosting me during my brief stay at the University of Hamburg, his constant guidance in learning the intricacies of LabVIEW, and for his constant friendship and advice.

In addition, the NSL, NanoTech West staff, and other technical staff at OSU: Denis Pelekhov, Camelia Selcu, Billy Kelly, Paul Steffan, Jon Carlin, Aimee Price, Derek Ditmer, Lisa Hommel, and Gordon Renkes for helping me constantly learn the ins-and-outs of the user facilities and being on-hand in case of issues. And of course, to Mark Studor and the late Bob Wells for help, friendship, and many entertaining conversations.

I also thank the physics support staff, in particular, Kris Dunlap, Amanda Zuurdeeg, and Jaimie Mollison for helping me navigate the tedious Ohio State bureaucracy.

I would never have made it to the end of this degree without the love and support of my friends and family. To my friends: Jack Brangham, Zac Henderson, Orey Wilson, Aaron Boothby, Justin Eldridge, Brandon Moss, and many others, thank you for tolerating the late nights and long weekends in the lab as well as me just generally being late most of the time. Without you around to relieve the tedium and stress of the lab, I probably would have gone insane.

And above all, my loving and supportive family. My parents, Brad and Amy Young, for constant support, endless encouragement, and raising me to work for what I love, I can't thank you enough. Finally, thanks to my sister, Cara Young, who is always there for me when I need her.

Vita

June 2006 ..... Triway High School, Wooster, OH

June 2010 ..... B.S. Physics and Mathematics, Otterbein College, Westerville, OH

2010 to present ..... Graduate Teaching and Research Associate Department of Physics, The Ohio State University, Columbus, OH

August 2013 ..... M.S. Physics, The Ohio State University, Columbus, OH

Publications

Young, J. R.; Chitara, B.; Cultrara, N. D.; Arguilla, M. Q.; Jiang, S.; Fan, F.; Johnston-halperin, E.; Goldberger, J. E., *Water activated doping and transport in multilayered germanane crystals.* Journal of Physics: Condensed Matter. **28**: p. 34001-34001. 2016. http://dx.doi.org/10.1088/0953-8984/28/3/034001

Berger, A. J.; Page, M. R.; Jacob, J.; **Young, J. R**.; Lewis, J.; Wenzel, L.; Bhallamudi, V. P.; Johnston-Halperin, E.; Pelekhov, D. V.; Hammel, P. C., *A versatile LabVIEW and field-programmable gate array-based scanning probe microscope for in operando electronic device characterization.* Review of Scientific Instruments. **85**: p. 123702. 2014. http://dx.doi.org/10.1063/1.4902934

Johnson, S. D.; **Young, J. R**.; Zieve, R. J.; Cooley, J. C., *Superconductivity in single-crystal YIn_3.* Solid State Communication. **152**(6): P. 513-515. http://dx.doi.org/10.1016/j.ssc.2011.12.040

Fields of Study

Major Field: Physics

Table of Contents

List of Tables

List of Figures

Chapter 1: Introduction

The emerging class of two-dimensional (2D) materials represents the ultimate limit for material thickness, with thicknesses of only a single atomic layer, which are attainable in graphene and its analogues. Further, the increasing number of members in this materials class offers a rich variety of functionalities and material properties which differ dramatically from their bulk counterparts and can further be tuned and combined to create complex architectures. A prime example of this variety is seen in the family of 2D transition metal dichalcogenides (TMDs) which, depending on the atomic composition, exhibit a full range of electronic and optical properties, including insulating, metallic, semiconducting, and superconducting behavior. When combined with the extremely high mobility properties of graphene, or the spin-orbit and band-gap tunability of the group IV graphene and graphane analogs, the potential for both new physics and device applications is immense.

This dissertation investigates not only this potential, but also the many challenges involved in exploring the functionality of this new class of materials and the development of novel growth techniques. First though, an introduction to the field of 2D materials is required. In **Chapter 2**, we provides the historical background, recent progress, and future challenges of both graphene and several 2D materials beyond graphene.

The remainder of this dissertation details the progress in the investigation and utilization of the unique surface sensitivity of 2D materials systems using three distinct approaches. In **Chapter 3**, we investigate electronic transport in germanane, a germanium analog of graphane, through a combination of electronic measurements on multi-layer crystals and finite-element modeling. These crystals are synthesized by doping the precursor, $CaGe_2$, with phosphorous. In addition to doping this 2D material with phosphorous, we uncover a sensitivity of this transport to the presence of water-vapor, as well as an anisotropy between inter- and intra-layer resistivity of up to eleven orders of magnitude. The strong water sensitivity and weak inter-layer coupling mean that the transport in these samples is dominated by the topmost layer and suggests that it may be possible to measure the effects of 2D materials in bulk materials by making electrical contact to only the topmost layer.

In **Chapter 4** we introduce a novel templated MoS_2 growth technique wherein Mo is deposited onto atomically-stepped sapphire substrates through a SiN stencil with feature sizes down to 100 nm and subsequently sulfurized at high temperature. These films have a quality comparable to the best MoS_2 prepared by other methodologies, and the thickness of the resulting MoS_2 patterns can be tuned layer-by-layer by controlling the initial Mo deposition. This approach critically enables the creation of patterned single-layer MoS_2 films with pristine surfaces suitable for subsequent modification via functionalization and mechanical stacking. Further, we anticipate that this growth technique should be broadly applicable within the family of transition metal dichalcogenides.

In **Chapter 5** we introduces the use of custom scanning probe and scanning tunneling microscopy instruments and techniques on electronically active graphene field effect transistors. This combined approach allows us to investigate the macroscopic transport characteristics of graphene which is locally modified by these microscopy techniques. In order to make these simultaneous measurements several challenges must be overcome, including device fabrication from chemical vapor deposition grown graphene, locating these micron scale devices on millimeter scale substrates, and the cleanliness of these devices. Significant progress is made towards this work, and several successful proof-of-concept measurements are performed with simultaneous microscopy and electronic measurements of these graphene field effect transistor devices.

Finally, in **Chapter 6** we conclude and summarize this dissertation. Two additional appendices are also including detailing the lithographic processes used (**Appendix A)** and the MoS_2 growth preparation (**Appendix B)**.

Chapter 2: 2D Materials

2.1 2D Materials – Graphene

2.1.1 The Rise of Graphene

Graphene's isolation in 2004 by Geim and Noveslov [1] not only triggered a race to investigate this particular system, but has also led to an explosion of discovery and research of other similar 2D materials. Graphene is a gapless-semiconductor composed of a single atomic layer of carbon atoms covalently bonded together in a honeycomb lattice. It is the thinnest material system discovered to date and is the fundamental building block for many of the other allotropes of carbon found in nature (**Figure 2.1**(a)). It exhibits many excellent electronic, optoelectronic, and mechanical properties. These, added to its relatively cheap entry point—requiring only Scotch tape and some patience—have attracted immense attention from all research sectors including academic institutions, governmental labs and agencies, as well as industrial corporations (See Refs [2-8] for general reviews on the topic).

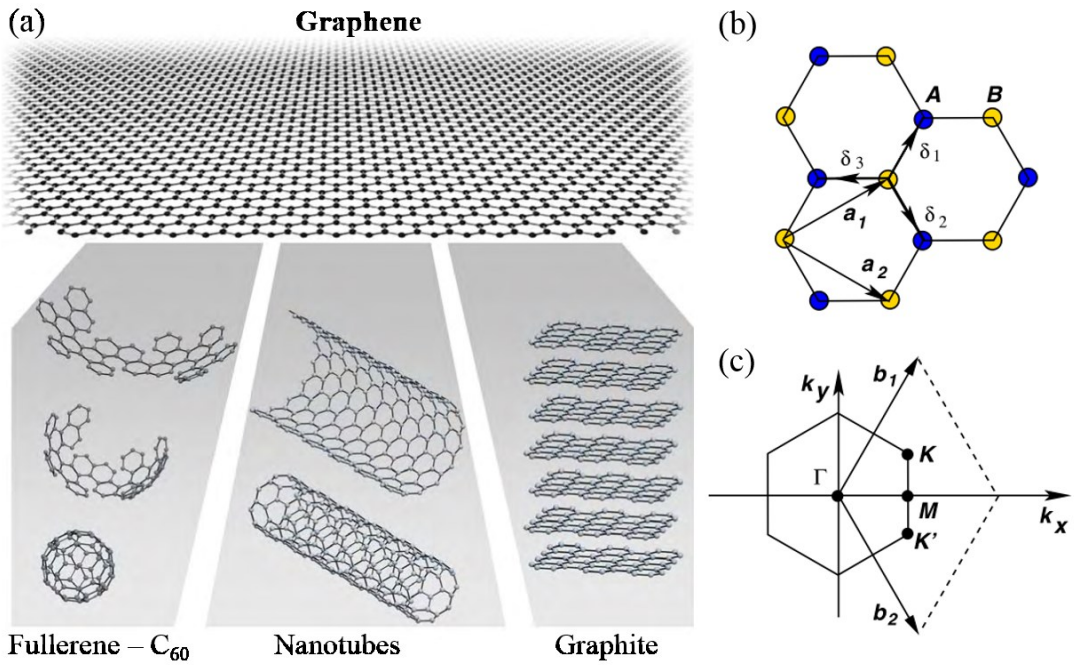

Figure 2.1 *Graphene Structure.*

(a) Graphene is the most basic allotrope of carbon from which carbon materials of other dimensionalities can be built. Reproduced from Ref [2]. (b) Schematic of graphene's crystal structure, showing the two triangular sublattices in blue and yellow. (c) Graphene's Brillouin zone. (b) and (c) reproduced from Ref. [8].

Much of the interest in this "miracle material" is due to the ways in which its various properties deviate from its 3D parent material, graphite. Many of these properties are a result of the graphene's atomic and electronic configuration. The carbon atoms of a graphene sheet are joined together by strong in-plane sp^2 covalent bonds. An additional delocalized π-orbital acts as a 2D electron gas (2DEG) across its surfaces [8]. When stacked together as bulk material (graphite), these π-orbitals interact with each other via weak van der Waals forces. However, when thinned out to a single-layer, the band structure transitions to a unique linear and gap-less band structure at the K and K′ points (charge neutrality points, known as "Dirac-points") of its Brillouin zone (**Figure 2.2**(a)-(c)). Around these points, the electrons behave as massless Fermi-Dirac particles [8, 9].

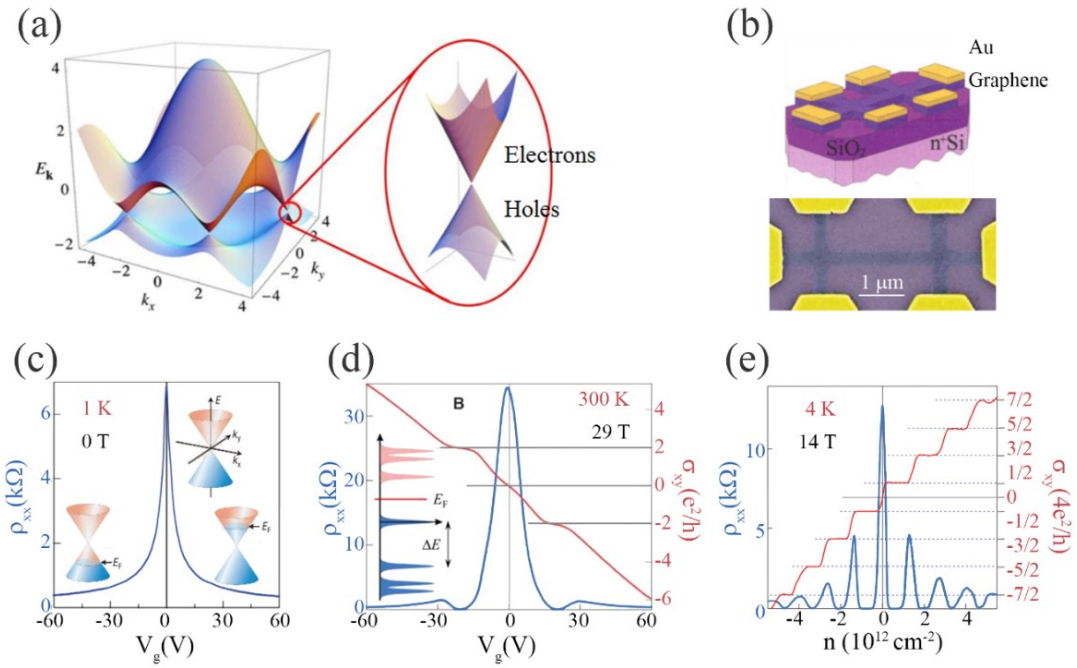

Figure 2.2 *Electronic Properties of Graphene.*

(a) Electronic band structure of graphene with a zoomed in view of band structure around the K/K′ Dirac point. Adapted from Ref. [3]. (b) Schematic (top) and optical micrograph (bottom) of graphene device. Adapted from [1] and [10], respectively. (c) Ambipolar field effect in single layer graphene, showing the Dirac peak. Insets show the change of Fermi energy as gate voltage is changed. Adapted from Ref [2]. Quantum Hall effect in monolayer graphene with ρ_{xx} (blue) and σ_{xy} (red) as a functions of gate voltage (and consequently carrier density) at room temperature (d) and 4K (e). (d) Inset: illustration of the quantized spectrum of graphene. Adapted from [11] and [10].

Graphene's unique band structure and the 2DEG nature of the π-orbitals results in carrier mobilities in excess of 200 000 $cm^2V^{-1}s^{-1}$, more than two orders of magnitude greater than silicon [12-14]. This high mobility allows the observation of both integer [10, 15] and fractional [16] quantum Hall effects (**Figure 2.2**(c) and (d), respectively). The integer quantum Hall effect is even present at room temperature. Additionally, the gapless nature of this material allows the carrier density and type to easily be tuned through the simple application of a gate voltage (**Figure 2.2**(c)). However, this mobility (along with the doping) can vary dramatically based both on the quality of the film and the substrate

that it's sitting on due to the extreme sensitivity of the delocalized π-orbitals to the surroundings of this essentially all-surface material [4].

A consequence of Graphene's sensitivity to its surroundings is that contact with other materials typically degrades its high-mobility. For instance, SiO_2 is a common substrate for graphene and other 2D materials due to its natural use as a gate dielectric. However, it typically has many surface defects, charge impurities, and adsorbates which act as scattering centers and limit graphene's mobility to less than 10^4 $cm^2V^{-1}s^{-1}$ [17]. The most straightforward solution to this problem is to synthesize suspended graphene devices where the graphene is either draped over existing holes in substrates or the substrate is etched out from under portions of the graphene. It's in these devices that electron mobilities above 10^5 $cm^2V^{-1}s^{-1}$ were first achieved [14]. Unfortunately, suspended graphene's device architecture imposes severe limitations upon device design and fabrication. This has led to a shift toward using insulating hexagonal boron nitride (*h*-BN, an electronically inactive 2D material, see section 2.2.3) as a substrate to achieve electronic transport similar to that of suspended graphene [18].

In the past several years, this technique of isolating the graphene from potential scattering centers through the use of inert *h*-BN has been taken a step further and graphene has been fully encapsulated by *h*-BN (**Figure 2.3**(a)) [19]. Complete encapsulation has the effect of both protecting the sensitive graphene sheet from atmospheric interactions and providing *h*-BN for use as an ultrathin top-gate dielectric. The complete isolation of graphene from potential environmental interactions has also been successfully combined with the development of a true one-dimensional edge contact (**Figure 2.3**(b)) [20]. This

has recently resulted in several exciting results such as ballistic transport over 28 μm—limited only by the device dimensions (**Figure 2.3**(b))—and mobilities up to 10^6 $cm^2V^{-1}s^{-1}$ [21].

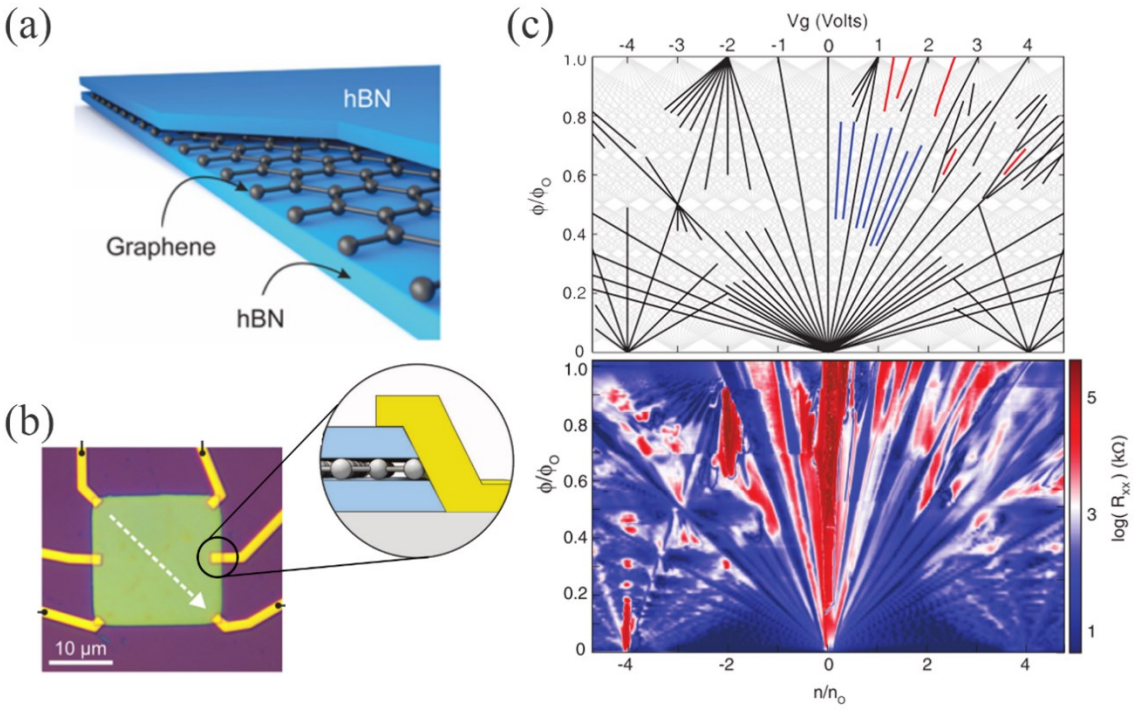

Figure 2.3 *Encapsulated Graphene.*

(a) Schematic of graphene encapsulated in *h*-BN. Adapted from Ref. [21]. (b) Optical micrograph of encapsulated graphene device with 1D edge contacts (inset). Adapted from Ref. [21] and [20]. (c) Bottom: Hall resistance plotted as a function of normalized magnetic field and carrier density, showing the Hofstadter energy spectrum. Top: Diagram showing the visible states in the data from the bottom figure. Here, black lines show the Bloch splitting and integer quantum Hall states, blue lines indicate the fractional quantum Hall states, and the red lines correspond to anomalous fractional Bloch states. Adapted from Ref. [22].

Using these techniques, Wang, *et al.* recently took advantage of this high-quality encapsulation to measure a complete unit cell of the Hofstadter energy spectrum (Hofstadter butterfly) [22]. This consists of the integer and fractional quantum hall states as well as an additional Bloch splitting (including a new previously unobserved fractional

Bloch splitting) due to the moiré-super-lattice which exists between the graphene and *h*-BN atomic structures (**Figure 2.3**(c)) [22]. The exploration of extremely high-quality, high-mobility, encapsulated graphene is only scratching the surface of the potential this material has as a platform for exploring unique electronic properties and potential device applications [23-26].

In addition to its exciting electronic properties, graphene exhibits a high thermal conductivity of 3 000 $W \cdot m^{-1}K^{-1}$, nearly ten times that of Cu [27, 28] and has attracted considerable attention in the field of spintronics because of its long spin lifetime (1-6 ns at 4 K, and 0.5-2 ns at 300 K) and spin diffusion length (3-12 μm at 300 K) [29]. Due to the large energies of the covalent carbon-carbon bonds, graphene has a strength close to 130 GPa—greater than any other material—and a Young's modulus of 1 TPa [30]. Graphene is oxidation resistant and stable at temperatures up to 1000 °C, making it attractive as a protective coating for other materials [31]. It is also impermeable to most gases [32]. Optically, monolayer graphene is 97.7% transparent in the visible and IR spectrums making it an excellent candidate for transparent 2D contacts and solar cell applications [33-35]. Yet, despite this optical transparency, it can be easily identified as a single-layer on SiO_2 substrates of specific thicknesses [36-38]. This visibility on SiO_2 substrates (see **Figure 2.2**(b) for example) along with the ease of the Scotch tape exfoliation technique have been the key ingredients to graphene's discovery and the speed at which this material has been adopted by research groups across the world.

2.1.2 Graphene Growth

The initial work of Novoselov and Geim (as well as much that followed) was conducted on graphene exfoliated from bulk crystals of highly ordered pyrolytic graphite (HOPG) [1]. This was made possible by the fact that graphene layers are only weakly bonded together by van der Waals forces. The exfoliation technique and an example of some results are shown in **Figure 2.4**(a)-(c). This method is surprisingly simple—requiring nothing more sophisticated then Scotch tape, an optical microscope, and some patience—and produces graphene of excellent crystalline and electronic quality [2, 12]. Due to the limited throughput, small dimensions (less than 1 mm^2), and lack of control over the flake location, exfoliation is not a suitable candidate for scaling to large samples, large numbers of devices, or for industrial applications. It is useful primarily for fundamental scientific research requiring small-area, high-quality material.

In the time since graphene's discovery, a large number of potentially scalable growth procedures have been developed [2, 4, 34, 39-52]. In particular, graphene growth via chemical vapor deposition (CVD) on Cu has emerged as one of the most convenient and promising routes toward high-quality, single layer graphene [39, 40, 50]. Copper as a substrate for graphene is not particularly useful, so generally after growth graphene is transferred to a substrate of choice by one of several methods [53-61]. The typical CVD growth and poly(methyl methacrylate) (PMMA) assisted transfer are shown in **Figure 2.4**(d) and (e) (methods from Refs. [50, 51]). Examples of good and bad large-area (~1 mm^2) graphene transfers can be seen in **Figure 2.4**(f) and (g), respectively. The CVD graphene used in this dissertation is synthesized using these growth and transfer techniques.

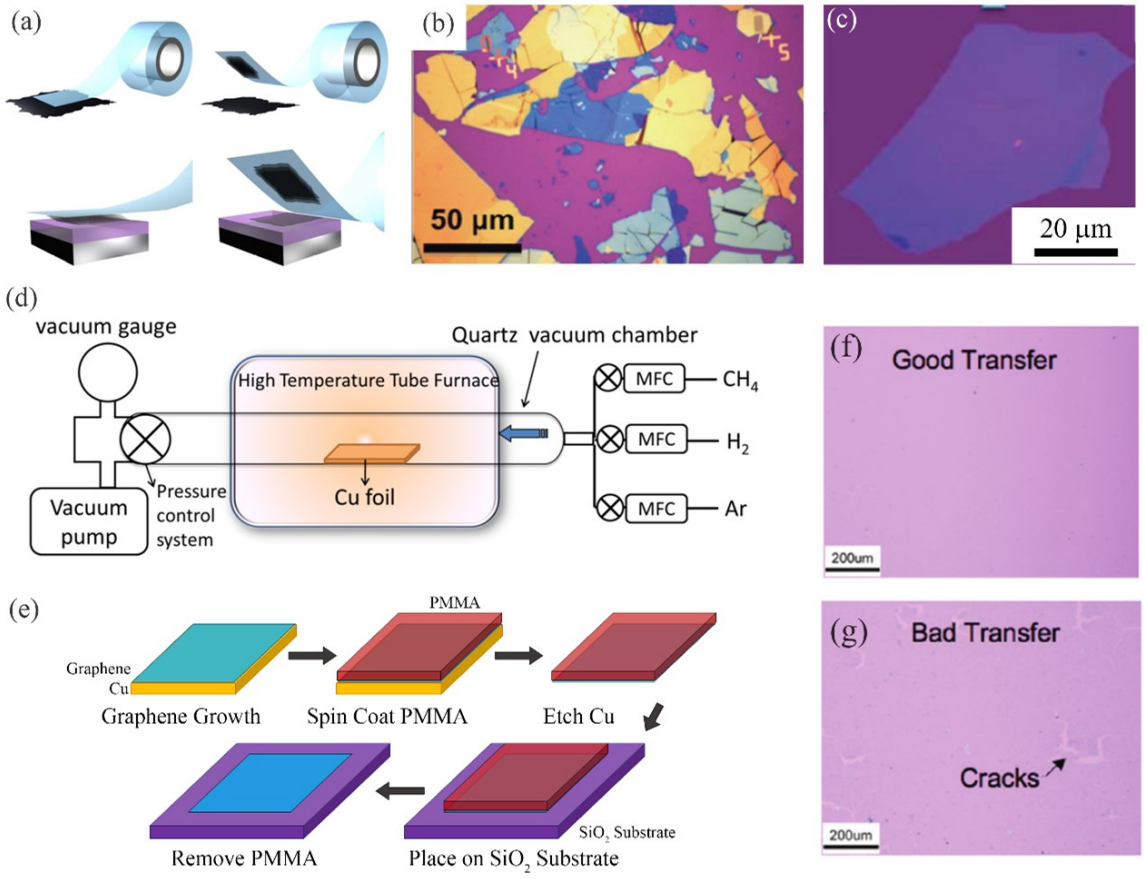

Figure 2.4 *Graphene Growth*.

(a) Schematic of graphene exfoliation. Scotch tape is stuck to a large HOPG crystal and then slowly peeled off taking several layers of graphite with the tape. The tape is then placed on clean SiO_2/Si substrates and removed, leaving behind patches of graphite/graphene of various layers. Adapted from Ref. [62]. (b) Optical micrographs of a patch of exfoliated graphene showing different crystals varying in thickness from few- to many-layers. Adapted from Ref. [53]. (c) Optical micrograph showing a few-layer exfoliated graphene flake on SiO_2. Adapted from Ref [53]. (d) Schematic showing the setup for CVD growth of graphene on Cu foil. Adapted from Ref [63]. (e) Schematic of the standard CVD grown graphene transfer process. Optical micrographs showing (f) the result of a good graphene transfer process with a uniform film and no cracks and (g) the result of a bad transfer with visible cracks in the graphene film. Adapted from Ref. [60].

In brief, Cu foil is chemically cleaned and loaded into the CVD furnace. It is then heated to a temperature near 1000 °C (near the Cu melting temperature of 1085 °C) and exposed to a methane (CH_4) and hydrogen (H_2) atmosphere. The Cu surface acts as a catalyst [64] for the decomposition of the methane into constituent carbon and diatomic hydrogen. This resulting carbon then bonds to create crystalline graphene on the copper surface. While

other metals have been used as growth substrates [43], the growth process on Cu is self-limiting and preferentially forms single layer graphene. Much work has gone into tuning the various parameters involved in this growth process to achieve large grain sizes [55, 65-67] as well as highly oriented grains [68, 69]. The CVD growth and subsequent transfer of graphene onto an arbitrary substrate is also the first method to be scaled up for potential industrial applications with the development of a roll-to-roll transfer process capable of growing and transferring continuous graphene sheets of up to nearly 1 m^2 to flexible substrates [51].

The quality of graphene grown via CVD methods is continuing to increase. However, many of the methodologies involved in transferring the graphene from the initial Cu foils to more useful substrates degrade the graphene. In the primary method of graphene transfer, the as-grown graphene on Cu is coated in a protective sacrificial layer of PMMA. The Cu foil is subsequently etched away, the remaining graphene/PMMA stack is rinsed in water, and is placed on the substrate of choice (normally SiO_2 on doped Si). Once the sample has dried, the PMMA is removed using acetone. While efforts are taken to protect the graphene, this process still degrades the graphene either through tears and wrinkling from the Cu etching and physical transfer process or through contamination from the organic resists used in the process.

Significant work has gone into post-transfer cleaning [56, 58, 60, 61, 70-72], resist-less transfers [56, 57], and etch-free transfers [54, 55, 73]. These cleaning and improved transfer techniques, combined with the *h*-BN encapsulation discussed in the previous Section 2.1.1 were used to synthesize the device shown in **Figure 2.3**(b), which exhibited

ballistic transport up to 28 μm and carrier mobilities at least as large as those measured in exfoliated flakes [21]. However, unfortunately many of these ultra-clean transfer methods are only viable for small graphene flakes, bringing us back to the original problem of scalability.

2.1.3 Graphene Challenges and Outlook

Graphene's optical and mechanical properties, high mobility, and ballistic transport make it a fascinating material. It can be employed as a stage to investigate unique regimes of physics [22, 23, 26] and has the potential for industrial applications, such as flexible electronics, high-frequency transistors, logic transistors, and energy applications [7]. However, there are still two primary challenges for graphene research to overcome:

> **Challenge 1: Scalability –** Many of the exciting properties discussed in Section 2.1.1 are only achievable in the highly crystalline, pristine graphene that can currently only be achieved on an extremely small scale (typically exfoliation). While synthesis techniques are rapidly improving, the best examples of mass-produced graphene are currently well below the quality of that obtained using small-scale laboratory growth techniques.
>
> **Challenge 2: Tunability of electrical and chemical structure –** Graphene natively lacks several important electronic properties, such as opening a band gap, inducing correlated electron phenomena, or increasing the spin-orbit coupling. While some of these properties can be induced through surface modifications, this process typically destroys it's sought after carrier mobility [7, 74-76]. This

dramatically reduces its graphene's utility in optoelectronics, spintronics, and other emerging fields.

Challenge 1 is an extremely active area of research and the major results and current directions are described briefly in Section 2.1.2. While this dissertation doesn't focus on the scalability of graphene growth, in **Chapter 4** we do investigate novel growth techniques for MoS_2, another 2D material introduced in Section 2.2.1. Primarily however, the remainder of this work focuses on Challenge 2.

There are two primary routes toward a solution for Challenge 2. The first is to **deepen** the understanding of graphene itself. In particular, we ask the question: *"How do microscopic, local changes to graphene's chemical structure affect the macroscopic properties and electronic transport?"* Significant effort has been dedicated to the task of investigating the chemical modification of graphene [77]. Some promising examples are the hydrogenation and fluorination of graphene (graphane and fluorographene respectively) [78, 79] as well as the doping of graphene via transition metal adatoms [80]. However, in these and other cases, the chemical modification is done on a substrate wide scale. **Chapter 5** introduces a combination of transport devices (from CVD grown graphene) and custom scanning probe and tunneling microscopy (SPM and STM, respectively) instruments and techniques [81]. These are used to investigate macroscopic transport characteristics of graphene as it is actively scanned or modified by STM or SPM techniques [82].

The second route to exploring the tunability of graphene's electronic properties is to **broaden** the investigation to similar materials. Since the discovery of graphene in 2004,

the number of available 2D materials to study has gone from one—graphene itself—to an ever lengthening list. Indeed, by expanding the breadth of the search for tunability in 2D crystals to materials beyond graphene, a plethora of materials are revealed. These include metals, semiconductors, insulators, superconductors, topological insulators, as well as various forms of magnetic materials. In addition, many of these materials have tunable optical and electronic properties. In the next section we briefly explore several of these different classes of two-dimensional materials that have been uncovered in the past decade.

2.2 Beyond Graphene: Exploring the Periodic Table

Less than a year after the isolation of graphene via exfoliation in 2004, Geim and Novoselov used the same technique to exfoliate single layers of the semiconducting transition metal dichalcogenides (TMDs) MoS_2 and $NbSe_2$ from bulk geological crystals [83]. It would be nearly another five years before the scientific community widely began investigating other 2D materials, but once the transition began, an extraordinary number of new members of the 2D materials family emerged, including group IV graphene and graphane analogs, the insulating *h*-BN, a number of additional TMD materials, and more recently oxides, perovskites, and phosphorene (see **Figure 2.5**, as well as Refs. [84-87] for reviews on materials beyond graphene). The remainder of this chapter explores several of these different 2D materials families, some of the defining characteristics, and finally, how these materials might be (and are currently being) combined into new and unique heterostructures.

(a)

Graphene family	Graphene & Graphene Oxide		Insulating *h*-BN	Graphane & Group IV Graphane Analogs	Phosphorene / Group IV Graphene Analogs: Silicene, Germanene
2D chalcogenides	MoS_2, WS_2, $MoSe_2$, WSe_2		Semiconducting dichalcogenides: $MoTe_2$, WTe_2, ZrS_2, $ZrSe_2$, and so on		Metallic dichalcogenides: $NbSe_2$, NbS_2, TaS_2, TiS_2, $NiSe_2$ and so on Layered Semiconductors: GaSe, GaTe, InSe, Bi_2Se_3 and so on
2D oxides	Micas, BSCCO	MoO_3, WO_3	Perovskite-type: $LaNb_2O_7$, $(Ca,Sr)_2Nb_3O_{10}$, $Bi_4Ti_3O_{12}$, $Ca_2Ta_2TiO_{10}$ and so on		Hydroxides: $Ni(OH)_2$, $Eu(OH)_2$ and so on
	Layered Cu oxides	TiO_2, MnO_2, V_2O_5, TaO_3, RuO_2 and so on			others

(b)

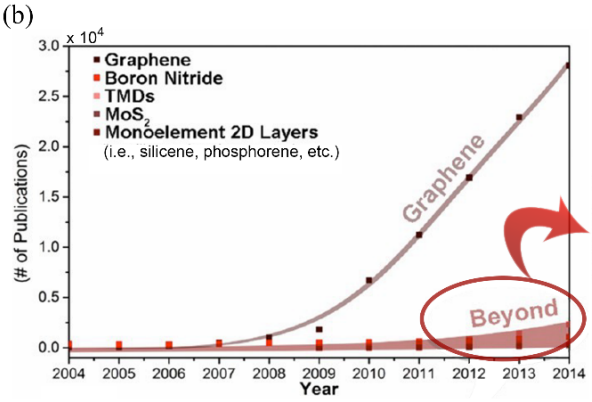

(c)

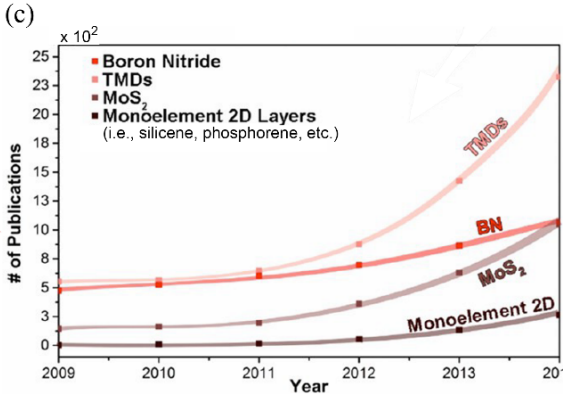

Figure 2.5 *2D Materials Beyond Graphene.*

(a) Some families of 2D materials. Blue shading represents air stable for long periods of time, green corresponds to materials that are mostly stable in air, but often for shorter periods of time, and orange indicates materials that are unstable in air. Grey shading means that single layers of these materials have been observed, but little else is known of them. Adapted from Ref. [88]. (b) Trends in publications of graphene and 2D materials beyond graphene and (c) Zoomed in plot of materials beyond graphene. Adapted from Ref. [84].

2.2.1 Transition Metal Dichalcogenides

Aside from graphene, TMDs are the most studied 2D materials to date. This is because: (a) Many of the TMD bulk forms are found in nature and exfoliation techniques are easily applied to them [83], (b) the growth and properties of many bulk TMD materials were studied, primarily in the timeframe of 1950-1970, giving researchers a point from which to start from in characterizing and growing these materials [89], and (c) the enormous variety

of nearly forty 2D TMD materials found or at least predicted provide researchers with a wide variety of materials to choose from [90] (**Figure 2.6**(a), for general reviews on TMDs see additionally Refs. [5, 91-93]). This family of materials has the stoichiometry of MX_2 (where M= transition metal, X= chalcogen), and exhibit one of two different modified honeycomb lattice structures (**Figure 2.6**(b) and (c)). The wide range of material properties, seen both in the bulk materials [89] and monolayer sheets [91] (**Table 2.1**), arise from the different coordination environments, a varying number of *d*-electrons present in the different TMD compounds, and the two possible crystal structures (some TMD compounds can be stable in either 2H or 1T crystal structures).

Table 2.1 *TMD Characteristics.*

Electronic properties of several of the most studied TMD materials. Band gaps are listed for both monolayer (1L) and bulk samples (Bulk). CDW stands for charge density wave. Adapted from [91].

Transition Metal	**· S_2**	**· Se_2**	**· Te_2**
Nb	Metal Superconducting CDW	Metal Superconducting CDW	Metal
Ta	Metal Superconducting CDW	Metal Superconducting CDW	Metal
Mo	Semiconducting 1L: 1.8 eV Bulk: 1.2 eV	Semiconducting 1L: 1.5 eV Bulk: 1.7 eV	Semiconducting 1L: 1.1 eV Bulk: 1.0 eV
W	Semiconducting 1L: 1.9-2.1 eV Bulk: 1.4 eV	Semiconducting 1L: 1.7 eV Bulk: 1.2 eV	Semiconducting 1L: 1.1 eV

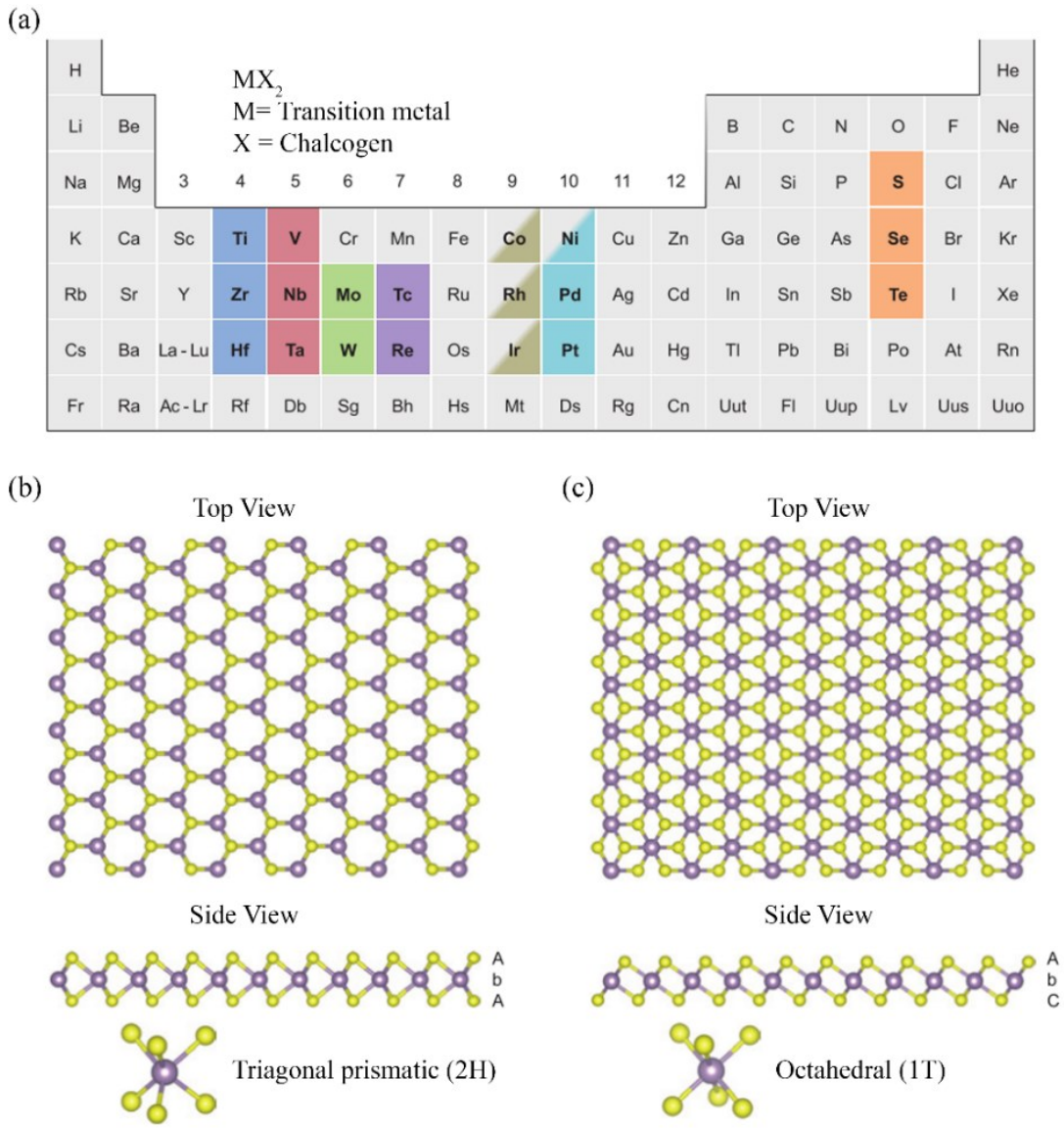

Figure 2.6 *TMD Structure*.

(a) Periodic table highlighting the various combinations of TMD compounds. Co, Rh, Ir, and Ni are partially shaded to indicate that only some of the dichalcogenide compounds form layer materials (for example NiS_2 is not a layered structure, while $NiTe_2$ is. (b) and (c) show top views and side views of the two different TMD crystal structures: (b) triagonal prismatic (2H), and (c) octahedral (1T). Adapted from Ref. [92]

MoS_2 has emerged as one of the most thoroughly investigated members of the TMD family, providing a good example for discussion here. MoS_2 has a wide variety of useful electrical and optoelectronic device applications [94-99], mechanical properties [100, 101],

and applications in flexible and transparent electronics [102, 103]. For example, bulk crystalline MoS_2 is a semiconductor with an indirect band gap of 1.2 eV [104]. When this three-dimensional crystal is reduced to a single layer [83, 105], a direct-gap of 1.8 eV emerges (**Figure 2.7**(a) and (b)), which can subsequently be tuned via strain [94, 106-108]. This emergence of a direct, tunable, optically-active band gap is not uncommon among monolayer TMD crystals, and is one of the reasons they have attracted so much attention as single-layer, semi-transparent transistors for flexible electronic applications [99, 109-111].

Another emergent feature is that when thinned to single layer, the breaking of inversion symmetry leads to a coupling of the spin and valley degrees of freedom, resulting in valley-dependent optical selection rules [112, 113]. This effect, as well as strong spin-orbit coupling makes this material attractive for spintronics and valleytronics applications [113-115]. Few-layer and monolayer TMDs can be distinguished reliably through not only optical and atomic force microscopy [116], but also through the shifting of Raman-active phonon modes [117, 118] and photoluminescence spectra [94, 95, 119] as a function of layer thickness (**Figure 2.7**(c)-(e)). This set of tunable properties in a 2D material are a large part of the reason that interest in them has grown over the past years. However, much like graphene, these materials are still very new, and one of the largest struggles in the field is synthesizing high quality, clean material.

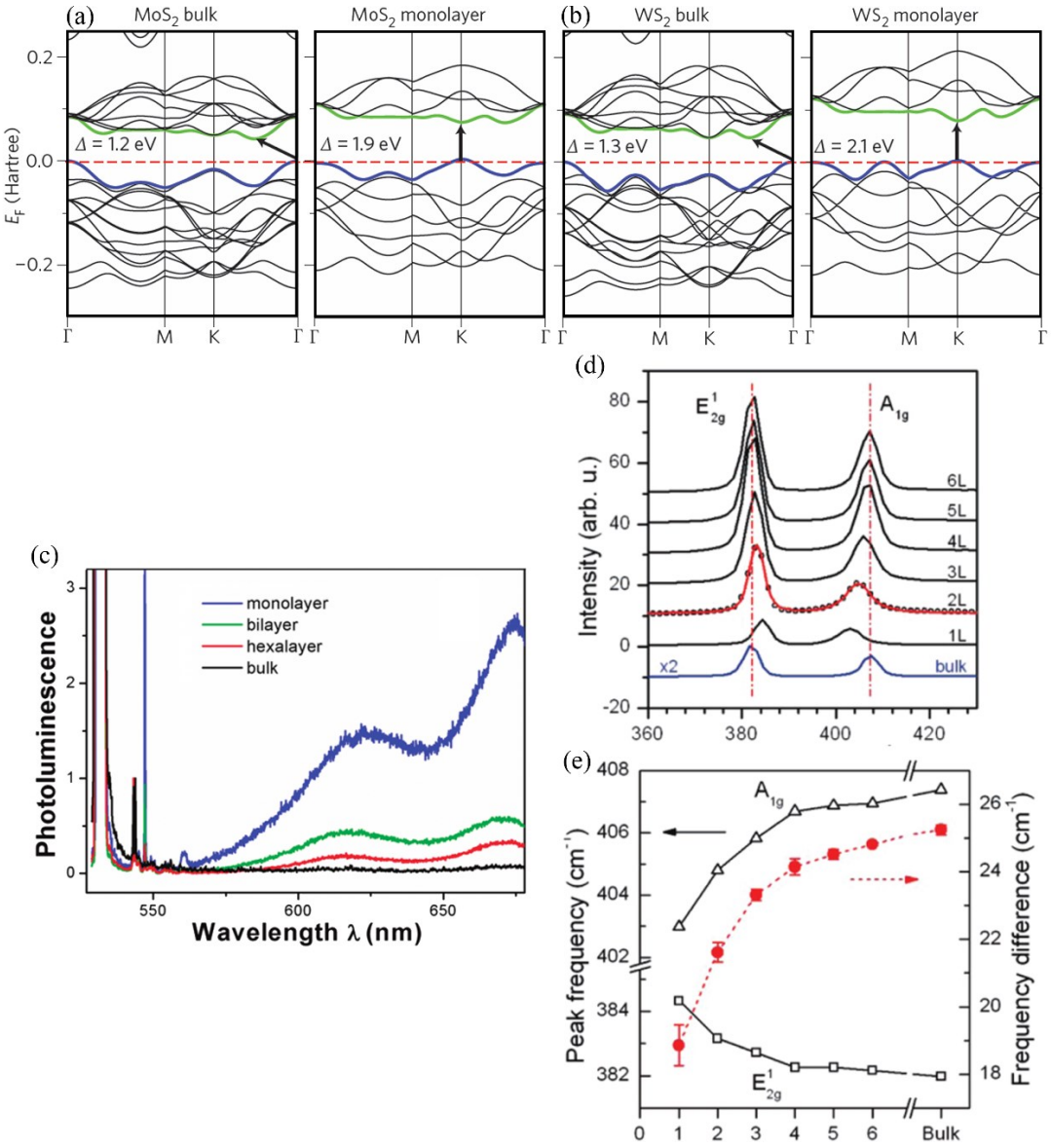

Figure 2.7 *TMD Electronic and Optical Characteristics.*

Calculated band structures of MoS_2 (a) and WS_2 (b) showing the transition from a bulk indirect gap, to a direct gap in the monolayer. Adapted from Ref. [108]. The evolution of the photoluminescence (PL) (c) and Raman (d) and (e) spectra as MoS_2 layer thickness is reduced to single layer. (c) Adapted from [95], (d) and (e) adapted from [117].

Similar to graphene, much of the initial work with TMDs was done using exfoliated material. However in the last several years, many more scalable methodologies for TMD growth have been developed. Again, using MoS_2 as an example case, these techniques

include sputtering [120-122], vapor-solid growth [123], thermal decomposition of thiomolybdate [124], chemical vapor deposition (CVD) [125-134] and recently metal-organic CVD [135, 136] and atomic layer deposition [137] (See **Figure 2.8**). In particular, the CVD techniques—where MoO_3 and S precursors are typically evaporated upstream of a heated growth substrate—produce very high-quality, triangular, monolayer MoS_2 islands on the order of 10-100 μm laterally. These can merge together in isolated areas of the growth substrate forming local, continuous films [125-134]. Recently, pre-treated, c-axis sapphire has been used as a growth substrates for CVD growth [131-133]. This promotes MoS_2 flake growth in the same lattice orientation, greatly reducing the number of domains present in these convergent crystalline films.

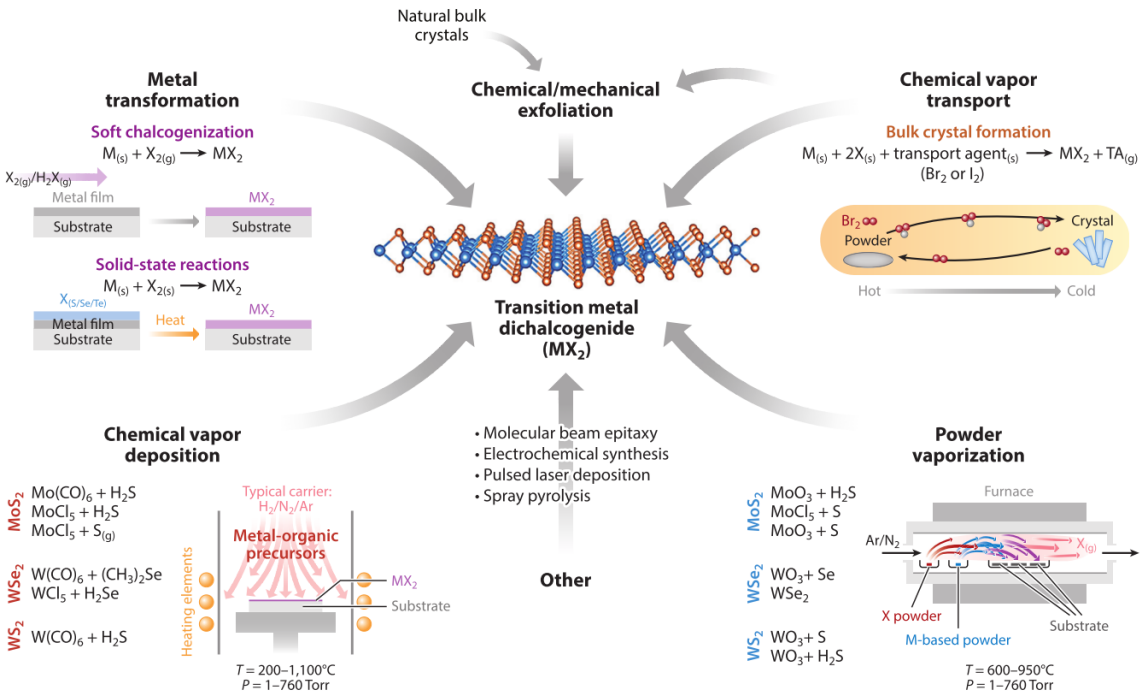

Figure 2.8 *TMD Growth techniques*.

Schematic showing the primary growth methods of TMDs. From [85].

An alternative to the CVD growth technique which is both straight-forward and inexpensive is through the sulfurization of either Mo [138-143] or MoO_3 [144] films. This sulfurization method produces uniform large-area films limited only by the location of the pre-deposited Mo or MoO_3. The thickness of these films also determine the final MoS_2 film thickness. While easy to use and highly tunable, these resulting films are polycrystalline and multi-layer. In several cases, both the CVD and sulfurization growth methods have been augmented to grow MoS_2 in predetermined locations by seeding [127, 145, 146] or patterning [128, 147] the initial substrate, and by templating the pre-deposited S film prior to sulfurization [141, 146]. In **Chapter 4** we introduce a novel bottom-up approach to grow templated, monolayer MoS_2 with sub-micron feature sizes—without need of resists—through the use of a SiN membrane stencil through which Mo films are deposited onto atomically stepped sapphire substrates and subsequently sulfurized. The result is templated, high-quality, MoS_2, with pristine interfaces which we believe will be useful in the creation of vertically stacked heterostructures.

2.2.2 Group IV Graphane Analogs

Another family of 2D materials are the group IV analogs to graphane (the hydrogenated version of graphene [78]). While graphene is an incredibly stable material, its analogs based on the other group IV elements silicon, germanium, and tin—known respectively as silicene, germanene, and stanene—are less stable, and thus far have only recently been reportedly synthesized in ultrahigh vacuum systems [5, 148-154]. The instability of these materials arises because the electrons tend to form sp^3-hybridzied orbitals (one of the

causes of the buckled lattice in these materials), rather than the more stable sp^2 configuration of graphene. In the graphene analogs, these sp^3 orbitals are bonded to other in-plane atoms, while the fourth, out-of-plane bond, is left empty causing these materials to be extremely reactive, and hence unstable in air.

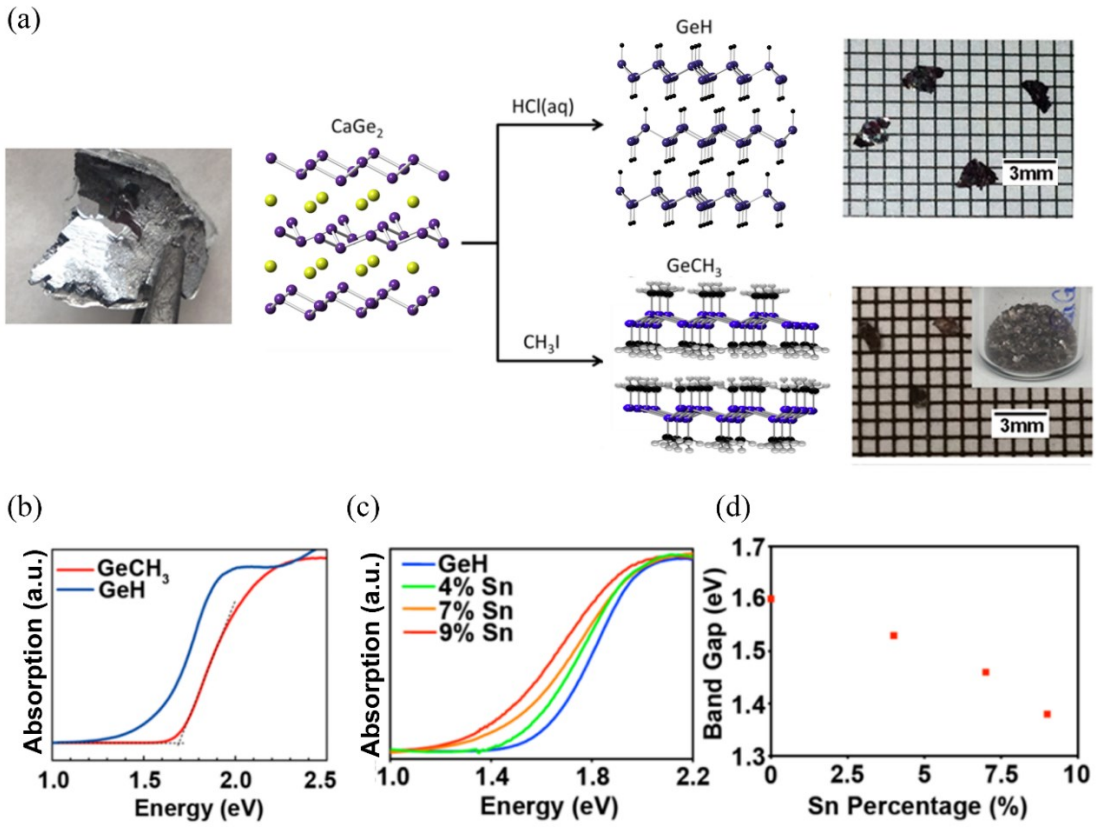

Figure 2.9 *Germanane Synthesis and Electronic Characteristics.*

(a) Schematic of the synthesis route from the $CaGe_2$ precursor (left) to the hydrogen- or methyl-terminated germanane. Light absorbance at different energies demonstrating the change in band-gap as the terminating ligand (b) and Ge-Sn alloy (c) is changed. (d) Extracted band-gap energy from (c) as a function of the Sn percentage in the Ge-Sn alloy. Adapted from Refs. [155-158]

The group IV graphane analogues (silicane, germanane, and stannanane) are by nature much more stable because this out-of-plane sp^3-orbital is now terminated by a ligand.

These materials are uniquely poised for the investigation of novel electronic, spintronic, and optical phenomena due to tunability of their band gap, spin-orbit coupling, and many-body interactions through either manipulation of the covalent termination of the out-of-plane sp^3 orbital or via alloying of the group IV elemental backbone. As an example, for the hydrogen-terminated materials, as the atomic number of the group IV material is increased, the spin-orbit coupling is predicted to increase (Si: ~ 1 meV, Ge: ~24 meV, and Sn: ~ 300 meV) while the band-gap is predicted to decrease (Si: ~2.9 eV, Ge: ~1.5 eV, and Sn: ~300 meV) [86, 159-161].

Though this particular family of 2D materials is much younger than graphene and TMD crystals, some early work with germanium based materials is showing promising results. The air-stable germanane (GeH), is synthesized using a two stage process [155]. Initially the β-$CaGe_2$ (Zintl phase) crystal is synthesized via either bulk crystal growth [155], or molecular beam epitaxy (MBE) growth [162, 163]. This precursor is subsequently converted into GeH by immersion in concentrated hydrochloric acid (HCl). This process is shown in **Figure 2.9**(a). GeH is optically active and indeed, when the terminating ligand is changed from hydrogen to a methyl group (through a slightly modified conversion process), the band gap is observed to shift up by 0.15 eV (**Figure 2.9**(b)) [156]. Further, by alloying the initial $CaGe_2$ precursor with Sn, the band-gap shifts downward by 0.2 eV at a 10% Sn concentration (**Figure 2.9**(c) and (d)) [157]. In **Chapter 3**, we investigate the electronic properties of phosphorous doped GeH crystals through electronic transport measurements and finite element modeling. We find that while the electronic quality needs improvement, the material exhibits a photoconductivity signal matching the optical

absorbance. Also an increase in current signal by up to three orders-of-magnitude under air exposure and an anisotropy between in-plane and out-of-plane resistivity by as much as 11 orders-of-magnitude are both observed.

2.2.3 Other 2D materials

The number of 2D materials being investigated across the world has been increasing over the past decade and while graphene, TMDs, and group IV graphene and graphane analogs cover a large area of the playing field, there are still a great number of 2D materials that have not been mentioned (see Refs. [84-87]). Before moving forward, it's worth briefly mentioning two additional 2D materials.

Hexagonal boron nitride (*h*-BN), mentioned briefly in Section 2.1.1, is an analogue of graphene but has alternating B and N atoms in place of the carbon atoms [164]. Similar to graphene, it is a single atomic layer thick and can be obtained either through exfoliation or various CVD methods [112, 165]. Electronically, *h*-BN is an insulator with a band-gap of 5.97 eV, and is ideal for use as a substrate for graphene since it provides an inert, uniform electronic environment [18]. Additionally, it can be used to fully encapsulate graphene, which dramatically improves the observed transport qualities [19, 21, 22].

Phosphorene (Shown in **Figure 2.10**), is a phosphorous analog of graphene with a unique armchair style crystal structure and was only recently isolated in 2014 by nearly simultaneously by two different research groups by exfoliation of black phosphorous [166, 167]. The armchair crystal structure creates an angular dependence in the transport properties of the material (**Figure 2.10**(b)-(c)). While it is more stable than the group IV

graphene analogs, it is only stable in air for a limited amount of time before degrading [168]. Phosphorene is particularly attractive because both its band-gap and mobility are highly tunable by the number of layers present [169]. To date, mobilities up to 10^3 $cm^2V^{-1}s^{-1}$ have been observed, with band-gap values varying between 0.3-2 eV [167, 169]. Despite its youth, phosphorene is a promising material that combines many of the best properties of TMD semiconductors (such as a tunable band-gap), with the higher mobilities found in graphene.

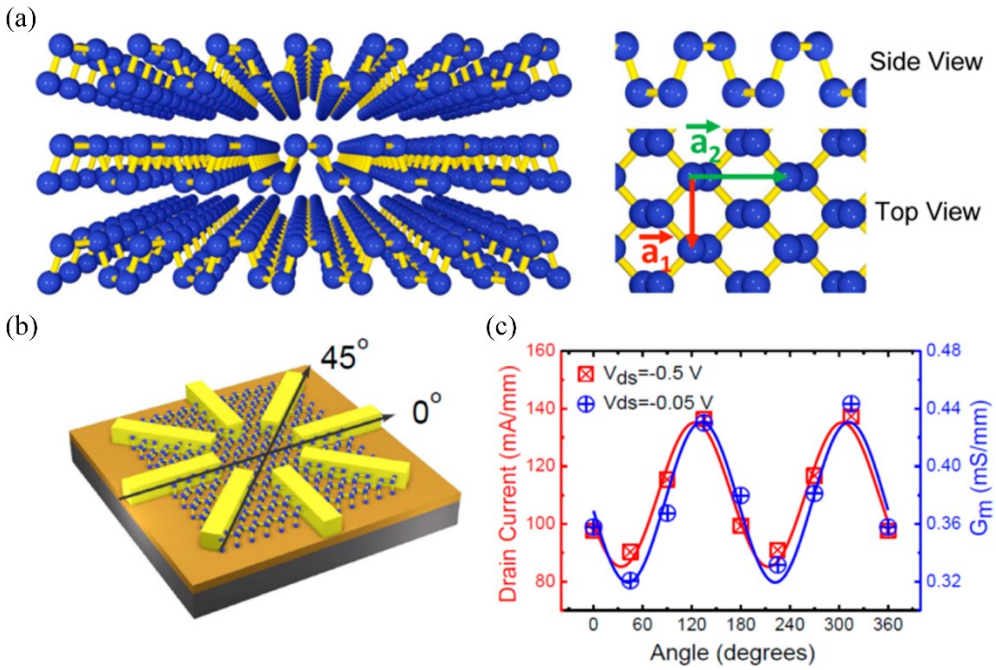

Figure 2.10 *Phosphorene.*

(a) Armchair crystal structure of phosphorene showing a 3D side view of bulk (left), and a side and top view (right). (b) Phosphorene device schematic (c) Angular dependence of the drain current and conductance (G_m) of a 10nm thick device, which is a result of the unique symmetry breaking crystal structure of the material. Adapted from [166]

2.2.4 Outlook

The growing field of 2D materials—started by the isolation of graphene in 2004—has already produced a great number of 2D materials with a unique tunable array of properties and this search for materials and properties shows no signs of stopping, or even slowing. However, it's also clear that a new trend is emerging from this field: the combination of individual elements from this large library of 2D materials (50+ and growing) into vertically stacked van der Waals heterostructures. Geim & Grigorieva coined the idea of treating 2D materials as "Legos" in their 2013 review article [170] when they said:

> "If one considers 2D crystals to be analogous to Lego blocks...the construction of a huge variety of layered structures becomes possible. Conceptually, this atomic-scale Lego resembles molecular beam epitaxy but employs different 'construction' rules and a distinct set of materials."

This idea of treating various 2D materials as Legos has gained traction in the field over the past several years. While several routes toward this idea have been introduced (see Refs. [84, 103, 170-172] for topical reviews), one particularly powerful technique of polymer-free 2D heterostructure assembly has emerged; taking the idea of Legos literally and creating heterostructures by physically stacking materials together [20, 102]. This technique is the one used to create the *h*-BN encapsulated, ultra-high mobility graphene devices [21] discussed in Section 2.1.1 (**Figure 2.3**). Recently, it has been used to fabricate an all-2D p-n junction from MoS_2, WSe_2 and graphene [173] and the dual-gated, encapsulated, MoS_2 transistor [96], shown in **Figure 2.11**.

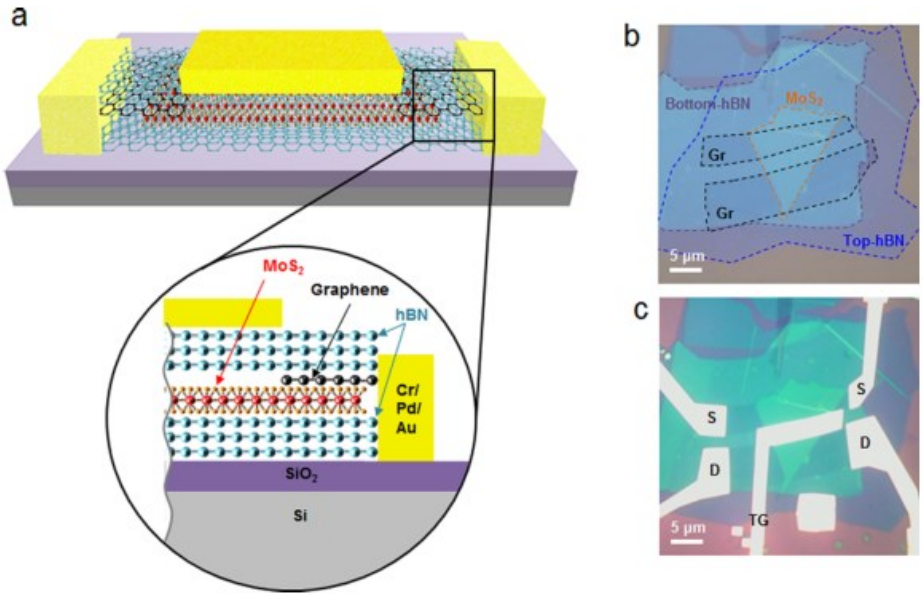

Figure 2.11 *h-BN Encapsulated MoS_2 Field-Effect Transistor.*

(a) Schematic of encapsulated MoS_2 transistor with graphene edge contacted electrodes. (b) Optical micrograph of the stack of *h*-BN/gr/MoS_2/*h*-BN before device fabrication. (c) Optical micrograph of the completed device. From Ref. [96]

This is a very exciting time to be active in this field of 2D materials research. While an immense amount of work has been accomplished in the past decade toward the exploration of these new material systems, there are still many challenges ahead. These include the continued search for tunability in 2D material properties—for example, 2D ferromagnetism, a property of fundamental interest to the spintronic community—and for scalable, high-quality material growth methods.

2.3 References

1. Novoselov, K.S., *et al.*, *Electric field effect in atomically thin carbon films.* Science. **306**(5696): p. 666-669. 2004. http://dx.doi.org/10.1126/science.1102896

2. Geim, A.K. and K.S. Novoselov, *The rise of graphene.* Nature Materials. **6**(3): p. 183-191. 2007. http://dx.doi.org/10.1038/nmat1849

3. Castro Neto, A.H., *et al.*, *The electronic properties of graphene.* Reviews of Modern Physics. **81**(1): p. 109-162. 2009. http://dx.doi.org/10.1103/RevModPhys.81.109

4. Cooper, D.R. and B. D'Anjou, *Experimental review of graphene.* ISRN Condensed Matter Physics. p. 501686-501686. 2012. http://dx.doi.org/10.5402/2012/501686

5. Xu, M., *et al.*, *Graphene-Like Two-Dimensional Materials.* Chemical Reviews. **113**(5): p. 3766-3798. 2013. http://dx.doi.org/10.1021/cr300263a

6. Geim, A.K., *Graphene: status and prospects.* Science. **324**(5934): p. 1530-4. 2009. http://dx.doi.org/10.1126/science.1158877

7. Novoselov, K.S., *et al.*, *A roadmap for graphene.* Nature. **490**(7419): p. 192-200. 2012. http://dx.doi.org/10.1038/nature11458

8. Das Sarma, S., *et al.*, *Electronic transport in two-dimensional graphene.* Reviews of Modern Physics. **83**(2): p. 407-470. 2011. http://dx.doi.org/10.1103/RevModPhys.83.407

9. Katsnelson, M.I., K.S. Novoselov, and a.K. Geim, *Chirial tunnelling and the Klein paradox in graphene.* Nature Physics. **2**(September): p. 620-625. 2006. http://dx.doi.org/10.1038/nphys384

10. Novoselov, K.S., *et al.*, *Two-Dimensional Gas of Massless Dirac Fermions in Graphene.* Nature. **438**(7065): p. 197-200. 2005. http://dx.doi.org/10.1038/nature04233

11. Novoselov, K.S., *et al.*, *Room-Temperature Quantum Hall Effect in Graphene.* Science. **315**(5817): p. 1379-1379. 2007. http://dx.doi.org/10.1126/science.1137201

12. Bolotin, K.I., *et al.*, *Ultrahigh electron mobility in suspended graphene.* Solid State Communications. **146**(9-10): p. 351-355. 2008. http://dx.doi.org/10.1016/j.ssc.2008.02.024

13. Morozov, S., *et al.*, *Giant Intrinsic Carrier Mobilities in Graphene and Its Bilayer.* Physical Review Letters. **100**(1): p. 016602-016602. 2008. http://dx.doi.org/10.1103/PhysRevLett.100.016602

14. Lau, C.N., W. Bao, and J. Velasco, *Properties of suspended graphene membranes.* Materials Today. **15**(6): p. 238-245. 2012. http://dx.doi.org/10.1016/S1369-7021(12)70114-1

15. Zhang, Y., *et al.*, *Experimental observation of the quantum Hall effect and Berry's phase in graphene.* Nature. **438**(7065): p. 201-204. 2005. http://dx.doi.org/10.1038/nature04235

16. Du, X., *et al.*, *Fractional quantum Hall effect and insulating phase of Dirac electrons in graphene.* Nature. **462**(7270): p. 192-5. 2009. http://dx.doi.org/10.1038/nature08522

17. Nagashio, K., *et al.*, *Electrical transport properties of graphene on SiO2 with specific surface structures.* Journal of Applied Physics. **110**(2). 2011. http://dx.doi.org/10.1063/1.3611394

18. Dean, C.R., *et al.*, *Boron nitride substrates for high-quality graphene electronics.* Nature Nanotechnology. **5**(10): p. 722-6. 2010. http://dx.doi.org/10.1038/nnano.2010.172

19. Mayorov, A.S., *et al.*, *Direct evidence for micron-scale ballistic transport in encapsulated graphene at room temperature.* Nano Letters. **11**: p. 2396-2399. 2011. http://dx.doi.org/10.1021/nl200758b

20. Wang, L., *et al.*, *One-dimensional electrical contact to a two-dimensional material.* Science. **342**(6158): p. 614-7. 2013. http://dx.doi.org/10.1126/science.1244358

21. Banszerus, L., *et al.*, *Ballistic transport exceeding 28 um in CVD grown graphene.* Nano Letters. **16**: p. 1387-1391. 2015. http://dx.doi.org/10.1021/acs.nanolett.5b04840

22. Wang, L., *et al.*, *Fractional fractal quantum Hall effect in graphene superlattices.* Science. **350**(6265): p. 1231-1231. 2015. http://dx.doi.org/10.1126/science.aad2102

23. Hynes, J.T., *et al.*, *The Focusing of Electron Flow and a Veselago Lens in Graphene p-n Junctions.* Science. **315**: p. 1252-1256. 2007. http://dx.doi.org/10.1126/science.1138020

24. Rickhaus, P., *et al.*, *Guiding of Electrons in a Few-Mode Ballistic Graphene Channel.* Nano Letters. **15**(9): p. 5819-5825. 2015. http://dx.doi.org/10.1021/acs.nanolett.5b01877

25. Singh, A.K., *et al.*, *Graphene based ballistic rectifiers.* Carbon. **84**(1): p. 124-129. 2015. http://dx.doi.org/10.1016/j.carbon.2014.11.064

26. Wilmart, Q., *et al.*, *A Klein-tunneling transistor with ballistic graphene.* 2D Materials. **1**(1): p. 011006-011006. 2014. http://dx.doi.org/10.1088/2053-1583/1/1/011006

27. Balandin, A.A., *Thermal properties of graphene and nanostructured carbon materials.* Nature Materials. **10**(8): p. 569-569. 2011. http://dx.doi.org/10.1038/nmat3064

28. Balandin, A.a., *et al.*, *Superior Thermal Conductivity of Single-Layer Graphene.* Nano Letters. **8**(3): p. 902-907. 2008. http://dx.doi.org/10.1021/nl0731872

29. Han, W., *et al.*, *Graphene spintronics.* Nature Nanotechnology. **9**(10): p. 794-807. 2014. http://dx.doi.org/10.1038/nnano.2014.214

30. Lee, C., *et al.*, *Measurement of the Elastic Properties and Intrinsic Strength of Monolayer Graphene.* Science. **321**(July): p. 385-388. 2008. http://dx.doi.org/10.1126/science.1157996

31. Chen, S., *et al.*, *Oxidation resistance of graphene-coated Cu and Cu Ni alloy.* ACS nano. **5**(2): p. 1321-7. 2011. http://dx.doi.org/10.1021/nn103028d

32. Bunch, J.S., *et al.*, *Impermeable atomic membranes from graphene sheets.* Nano Letters. **8**(8): p. 2458-2462. 2008. http://dx.doi.org/10.1021/nl801457b

33. Bonaccorso, F., *et al.*, *2D materials. Graphene, related two-dimensional crystals, and hybrid systems for energy conversion and storage.* Science. **347**(6217): p. 1246501-1246501. 2015. http://dx.doi.org/10.1126/science.1246501

34. Das, S., *et al.*, *Graphene synthesis and application for solar cells.* Journal of Materials Research. **29**(03): p. 299-319. 2014. http://dx.doi.org/10.1557/jmr.2013.297

35. Yin, Z., *et al.*, *Graphene-Based materials for solar cell applications.* Advanced Energy Materials. **4**(1): p. 1-19. 2014. http://dx.doi.org/10.1002/aenm.201300574

36. Blake, P., *et al.*, *Making graphene visible.* Applied Physics Letters. **91**(6): p. 33-36. 2007. http://dx.doi.org/10.1063/1.2768624

37. Nair, R.R., *et al.*, *Fine structure constant defines visual transparency of graphene.* Science. **320**(5881): p. 1308-1308. 2008. http://dx.doi.org/10.1126/science.1156965

38. Bonaccorso, F., *et al.*, *Graphene Photonics and Optoelectronics.* Nature Photonics. **4**(9): p. 611-622. 2010. http://dx.doi.org/10.1038/nphoton.2010.186

39. Zhang, Y., L. Zhang, and C. Zhou, *Review of chemical vapor deposition of graphene and related applications.* Accounts of Chemical Research. **46**(10): p. 2329-2339. 2013. http://dx.doi.org/10.1021/ar300203n

40. Mattevi, C., H. Kim, and M. Chhowalla, *A review of chemical vapour deposition of graphene on copper.* Journal of Materials Chemistry. **21**(10): p. 3324-3334. 2011. http://dx.doi.org/10.1039/C0JM02126A

41. Kosynkin, D.V., *et al.*, *Longitudinal unzipping of carbon nanotubes to form graphene nanoribbons.* Nature. **458**(7240): p. 872-876. 2009. http://dx.doi.org/10.1038/nature07872

42. Dreyer, D.R., R.S. Ruoff, and C.W. Bielawski, *From conception to realization: An historial account of graphene and some perspectives for its future.* Angewandte Chemie - International Edition. **49**(49): p. 9336-9344. 2010. http://dx.doi.org/10.1002/anie.201003024

43. Wintterlin, J. and M.L. Bocquet, *Graphene on metal surfaces.* Surface Science. **603**(10-12): p. 1841-1852. 2009. http://dx.doi.org/10.1016/j.susc.2008.08.037

44. Hernandez, Y., *et al.*, *High-yield production of graphene by liquid-phase exfoliation of graphite.* Nature Nanotechnology. **3**(9): p. 563-568. 2008. http://dx.doi.org/10.1038/nnano.2008.215

45. Hackley, J., *et al.*, *Graphitic carbon growth on Si(111) using solid source molecular beam epitaxy.* Applied Physics Letters. **95**(13): p. 1-4. 2009. http://dx.doi.org/10.1063/1.3242029

46. Virojanadara, C., *et al.*, *Homogeneous large-area graphene layer growth on 6H-SiC(0001).* Physical Review B. **78**(24): p. 1-6. 2008. http://dx.doi.org/10.1103/PhysRevB.78.245403

47. Segal, M., *Selling graphene by the ton.* Nature Nanotechnology. **4**(10): p. 612-614. 2009. http://dx.doi.org/10.1038/nnano.2009.279

48. Riedl, C., C. Coletti, and U. Starke, *Structural and electronic properties of epitaxial graphene on SiC(0001): a review of growth, characterization, transfer doping and hydrogen intercalation.* Journal of Physics D: Applied Physics. **43**(37): p. 374009-374009. 2010. http://dx.doi.org/10.1088/0022-3727/43/37/374009

49. Yan, Z., *et al.*, *Toward the synthesis of wafer-scale single-crystal graphene on copper foils.* ACS Nano. **6**(10): p. 9110-9117. 2012. http://dx.doi.org/10.1021/nn303352k

50. Kunkes, E.L., *et al.*, *Large-Area Synthesis of High-Quality and Uniform Graphene Films on Copper Foil.* Science. **1381**(2002): p. 3-6. 2008. http://dx.doi.org/10.1126/science.1171245

51. Bae, S., *et al.*, *Roll-to-roll production of 30-inch graphene films for transparent electrodes.* Nature Nanotechnology. **5**(8): p. 574-578. 2010. http://dx.doi.org/10.1038/nnano.2010.132

52. Kim, K.S., *et al.*, *Large-scale pattern growth of graphene films for stretchable transparent electrodes.* Nature. **457**(7230): p. 706-10. 2009. http://dx.doi.org/10.1038/nature07719

53. Kang, J., *et al.*, *Graphene transfer: key for applications.* Nanoscale. **4**: p. 5527-5537. 2012. http://dx.doi.org/10.1039/c2nr31317k

54. Gao, L., *et al.*, *Repeated growth and bubbling transfer of graphene with millimetre-size single-crystal grains using platinum.* Nature Communications. **3**: p. 699-699. 2012. http://dx.doi.org/10.1038/ncomms1702

55. Mafra, D.L., T. Ming, and J. Kong, *Facile graphene transfer directly to target substrates with a reusable metal catalyst.* Nanoscale. **7**(36): p. 14807-14812. 2015. http://dx.doi.org/10.1039/C5NR03892H

56. Lin, W.-H., *et al.*, *A Direct and Polymer-Free Method for Transferring Graphene Grown by Chemical Vapor Deposition to Any Substrate.* ACS Nano. **8**(2): p. 1784-1791. 2014. http://dx.doi.org/10.1021/nn406170d

57. Song, J., *et al.*, *A general method for transferring graphene onto soft surfaces.* Nature Nanotechnology. **8**(5): p. 356-62. 2013. http://dx.doi.org/10.1038/nnano.2013.63

58. Barin, G.B., *et al.*, *Optimized graphene transfer: Influence of polymethylmethacrylate (PMMA) layer concentration and baking time on grapheme final performance*. Carbon. **84**(C): p. 82-90. 2015. http://dx.doi.org/10.1016/j.carbon.2014.11.040

59. Ko, P.J., *et al.*, *Simple method to transfer graphene from metallic catalytic substrates to flexible surfaces without chemical etching.* Journal of Physics: Conference Series. **433**(1): p. 012002-012002. 2013. http://dx.doi.org/10.1088/1742-6596/433/1/012002

60. Li, X., *et al.*, *Transfer of large-area graphene films for high-performance transparent conductive electrodes.* Nano Letters. **9**(12): p. 4359-63. 2009. http://dx.doi.org/10.1021/nl902623y

61. Liang, X., *et al.*, *Toward clean and crackless transfer of graphene.* ACS Nano. **5**(11): p. 9144-53. 2011. http://dx.doi.org/10.1021/nn203377t

62. Novoselov, K.S. and a.H. Castro Neto, *Two-dimensional crystals-based heterostructures: materials with tailored properties.* Physica Scripta. **T146**: p. 014006-014006. 2012. http://dx.doi.org/10.1088/0031-8949/2012/T146/014006

63. Kumar, A. and C.H. Lee, *Synthesis and Biomedical Applications of Graphene: Present and Future Trends*. Advances in Graphene Science. 2013.

64. Li, X., *et al.*, *Evolution of graphene growth on Ni and Cu by carbon isotope labeling.* Nano Letters. **9**(12): p. 4268-4272. 2009. http://dx.doi.org/10.1021/nl902515k

65. Li, X., *et al.*, *Large-area graphene single crystals grown by low-pressure chemical vapor deposition of methane on copper.* JACS Communication. **133**(9): p. 2816-2819. 2011. http://dx.doi.org/10.1021/ja109793s

66. Hao, Y., *et al.*, *The role of surface oxygen in the growth of large single-crystal graphene on copper.* Science. **342**(6159): p. 720-3. 2013. http://dx.doi.org/10.1126/science.1243879

67. Banszerus, L., *et al.*, *Ultrahigh-mobility graphene devices from chemical vapor deposition on reusable copper.* Science Advances. **1**(6): p. 1-6. 2015. http://dx.doi.org/10.1126/sciadv.1500222

68. Huang, P.Y., *et al.*, *Grains and grain boundaries in single-layer graphene atomic patchwork quilts.* Nature. **469**(7330): p. 389-92. 2011. http://dx.doi.org/10.1038/nature09718

69. Brown, L., *et al.*, *Polycrystalline graphene with single crystalline electronic structure.* Nano Letters. **14**(10): p. 5706-5711. 2014. http://dx.doi.org/10.1021/nl502445j

70. Cheng, Z., *et al.*, *Toward intrinsic graphene surfaces: a systematic study on thermal annealing and wet-chemical treatment of SiO2-supported graphene devices.* Nano Letters. **11**(2): p. 767-71. 2011. http://dx.doi.org/10.1021/nl103977d

71. Lin, Y.-C., *et al.*, *Graphene annealing: how clean can it be?* Nano Letters. **12**(1): p. 414-9. 2012. http://dx.doi.org/10.1021/nl203733r

72. Moser, J., a. Barreiro, and a. Bachtold, *Current-induced cleaning of graphene.* Applied Physics Letters. **91**(16): p. 163513-163513. 2007. http://dx.doi.org/10.1063/1.2789673

73. Wang, Y., *et al.*, *Electrochemical delamination of CVD-grown graphene film: Toward the recyclable use of copper catalyst.* ACS Nano. **5**(12): p. 9927-9933. 2011. http://dx.doi.org/10.1021/nn203700w

74. Jariwala, D., A. Srivastava, and P.M. Ajayan, *Graphene Synthesis and Band Gap Opening.* Journal of Nanoscience and Nanotechnology. **11**(8): p. 6621-6641. 2011. http://dx.doi.org/10.1166/jnn.2011.5001

75. Schwierz, F., *Graphene transistors.* Nature Nanotechnology. **5**(7): p. 487-96. 2010. http://dx.doi.org/10.1038/nnano.2010.89

76. Kim, K., *et al.*, *A role for graphene in silicon-based semiconductor devices.* Nature. **479**(7373): p. 338-44. 2011. http://dx.doi.org/10.1038/nature10680

77. Lonkar, S.P., Y.S. Deshmukh, and A.A. Abdala, *Recent advances in chemical modifications of graphene.* Nano Research. 2014. http://dx.doi.org/10.1007/s12274-014-0622-9

78. Elias, D.C., *et al.*, *Control of graphene's properties by reversible hydrogenation: evidence for graphane.* Science. **323**(5914): p. 610-3. 2009. http://dx.doi.org/10.1126/science.1167130

79. Nair, R.R., *et al.*, *Fluorographene: A two-dimensional counterpart of Teflon.* Small. **6**(24): p. 2877-2884. 2010. http://dx.doi.org/10.1002/smll.201001555

80. Pi, K., *et al.*, *Electronic doping and scattering by transition metals on graphene.* Physical Review B. **80**(7): p. 1-5. 2009. http://dx.doi.org/10.1103/PhysRevB.80.075406

81. Berger, A.J., *et al.*, *A versatile LabVIEW and field-programmable gate array-based scanning probe microscope for in operando electronic device characterization.* Review of Scientific Instruments. **85**(12): p. 1-12. 2014. http://dx.doi.org/10.1063/1.4902934

82. Berger, A.J., *et al.*, *Correlating spin transport and electrode magnetization in a graphene spin valve: Simultaneous magnetic microscopy and non-local measurements.* Applied Physics Letters. **107**(14). 2015. http://dx.doi.org/10.1063/1.4932673

83. Novoselov, K.S., *et al.*, *Two-dimensional atomic crystals.* Proceedings of the National Academy of Sciences of the United States of America. **102**(30): p. 10451-10453. 2005. http://dx.doi.org/10.1073/pnas.0502848102

84. Bhimanapati, G.R., *et al.*, *Recent Advances in Two-Dimensional Materials beyond Graphene.* ACS Nano. **9**(12): p. 11509-11539. 2015. http://dx.doi.org/10.1021/acsnano.5b05556

85. Das, S., *et al.*, *Beyond Graphene: Progress in Novel Two-Dimensional Materials and van der Waals Solids.* Annual Review of Materials Research. **45**(1): p. 1-27. 2015. http://dx.doi.org/10.1146/annurev-matsci-070214-021034

86. Butler, S.Z., *et al.*, *Progress, Challenges, and Opportunities in Two-Dimensional Materials Beyond Graphene.* ACS Nano. **7**(4): p. 2898-2926. 2013. http://dx.doi.org/10.1021/nn400280c

87. Mas-Ballesté, R., *et al.*, *2D materials: to graphene and beyond.* Nanoscale. **3**(1): p. 20-30. 2011. http://dx.doi.org/10.1039/c0nr00323a

88. Gupta, A., T. Sakthivel, and S. Seal, *Recent development in 2D materials beyond graphene.* Progress in Materials Science. **73**: p. 44-126. 2015. http://dx.doi.org/10.1016/j.pmatsci.2015.02.002

89. Wilson, J.A. and A.D. Yoffe, *The transition metal dichalcogenides discussion and interpretation of the observed optical, electrical and structural properties.* Advances in Physics. **18**(73): p. 193-335. 1969. http://dx.doi.org/10.1080/00018736900101307

90. Ataca, C., H. Sahin, and S. Ciraci, *Stable, Single-Layer MX2 Transition-Metal Oxides and Dichalcogenides in a Honeycomb-Like Structure.* The Journal of Physical Chemistry C. **116**: p. 8983-8999. 2012. http://dx.doi.org/10.1021/jp212558p

91. Wang, Q.H., *et al.*, *Electronics and optoelectronics of two-dimensional transition metal dichalcogenides.* Nature Nanotechnology. **7**(11): p. 699-712. 2012. http://dx.doi.org/10.1038/nnano.2012.193

92. Chhowalla, M., *et al.*, *The chemistry of two-dimensional layered transition metal dichalcogenide nanosheets.* Nature Chemistry. **5**(4): p. 263-75. 2013. http://dx.doi.org/10.1038/nchem.1589

93. Jariwala, D., *et al.*, *Emerging Device Applications for for Semiconducting Two-Dimensional Transition Metal Dichalcogenides.* ACS Nano. **8**(2): p. 1102-1120. 2014. http://dx.doi.org/10.1021/nn500064s

94. Mak, K.F., *et al.*, *Atomically thin MoS2: a new direct-gap semiconductor.* Physical Review Letters. **105**(13): p. 136805. 2010. http://dx.doi.org/10.1103/PhysRevLett.105.136805

95. Splendiani, A., *et al.*, *Emerging photoluminescence in monolayer MoS2.* Nano Letters. **10**(4): p. 1271-1275. 2010. http://dx.doi.org/10.1021/nl903868w

96. Lee, G.-h., *et al.*, *Highly Stable , Dual-Gated MoS2 Transistors Encapsulated by Hexagonal Boron Nitride with Gate-Controllable Contact, Resistane and Threshold Voltage.* ACS Nano. **9**: p. 7019-7019. 2015. http://dx.doi.org/10.1021/acsnano.5b01341

97. Choi, W., *et al.*, *High-detectivity multilayer MoS2 phototransistors with spectral response from ultraviolet to infrared.* Advanced Materials. **24**(43): p. 5832-5836. 2012. http://dx.doi.org/10.1002/adma.201201909

98. Bertolazzi, S., D. Krasnozhon, and A. Kis, *Nonvolatile memory cells based on MoS2/graphene heterostructures.* ACS Nano. **7**(4): p. 3246-3252. 2013. http://dx.doi.org/10.1021/nn3059136

99. Bao, W., *et al.*, *High mobility ambipolar MoS2 field-effect transistors: Substrate and dielectric effects.* Applied Physics Letters. **102**(4). 2013. http://dx.doi.org/10.1063/1.4789365

100. Bertolazzi, S., J. Brivio, and A. Kis, *Stretching and breaking of ultrathin MoS2.* ACS Nano. **5**(12): p. 9703-9709. 2011. http://dx.doi.org/10.1021/nn203879f

101. Heiranian, M., A.B. Farimani, and N.R. Aluru, *Water desalination with a single-layer MoS2 nanopore.* Nature Communications. **6**: p. 1-6. 2015. http://dx.doi.org/10.1038/ncomms9616

102. Lee, G.-H., *et al.*, *Flexible and Transparent MoS2 Field-Effect Transistors on Hexagonal Boron Nitride-Graphene Heterostructures.* ACS Nano. **7**(9): p. 7931-7936. 2013. http://dx.doi.org/10.1021/nn402954e

103. Akinwande, D., N. Petrone, and J. Hone, *Two-dimensional flexible nanoelectronics.* Nature Communications. **5**: p. 5678-5678. 2014. http://dx.doi.org/10.1038/ncomms6678

104. Kam, K.K. and B.A. Parkinson, *Detailed Photocurrent Spectroscopy.* Journal of Physical Chemistry. **86**: p. 463-467. 1982. http://dx.doi.org/10.1021/j100393a010

105. Smith, R.J., *et al.*, *Large-scale exfoliation of inorganic layered compounds in aqueous surfactant solutions.* Advanced Materials. **23**(34): p. 3944-3948. 2011. http://dx.doi.org/10.1002/adma.201102584

106. Hunt, B., *et al.*, *Massive Dirac fermions and Hofstadter butterfly in van der Waals heterostructure.* Science. **340**(6139): p. 1427-1430. 2013. http://dx.doi.org/10.1126/science.1237240

107. Lebègue, S. and O. Eriksson, *Electronic structure of two-dimensional crystals from ab initio theory.* Physical Review B. **79**(11): p. 4-7. 2009. http://dx.doi.org/10.1103/PhysRevB.79.115409

108. Kuc, A., N. Zibouche, and T. Heine, *Influence of quantum confinement on the electronic structure of the transition metal sulfide TS2.* Physical Review B. **83**(24): p. 245213-245213. 2011. http://dx.doi.org/10.1103/PhysRevB.83.245213

109. Chang, H.Y., *et al.*, *High-performance, highly bendable MoS2 transistors with high-K dielectrics for flexible low-power systems.* ACS Nano. **7**(6): p. 5446-5452. 2013. http://dx.doi.org/10.1021/nn401429w

110. Radisavljevic, B., *et al.*, *Single-layer MoS2 transistors.* Nature Nanotechnology. **6**(3): p. 147-150. 2011. http://dx.doi.org/10.1038/nnano.2010.279

111. Radisavljevic, B., M.B. Whitwick, and A. Kis, *Integrated circuits and logic operations based on single-layer MoS2.* ACS Nano. **5**(12): p. 9934-9938. 2011. http://dx.doi.org/10.1021/nn203715c

112. Kim, K.K.*, et al.*, *Synthesis of monolayer hexagonal boron nitride on Cu foil using chemical vapor deposition.* Nano Letters. **12**(1): p. 161-166. 2012. http://dx.doi.org/10.1021/nl203249a

113. Mak, K.F.*, et al.*, *The valley Hall effect in MoS_2 transistors.* Science. **344**(6191): p. 1489-92. 2014. http://dx.doi.org/10.1126/science.1250140

114. Mak, K.F.*, et al.*, *Control of valley polarization in monolayer MoS2 by optical helicity.* Nature Nanotechnology. **7**(8): p. 494-498. 2012. http://dx.doi.org/10.1038/nnano.2012.96

115. Zeng, H.*, et al.*, *Valley polarization in MoS2 monolayers by optical pumping.* Nature Nanotechnology. **7**(8): p. 490-493. 2012. http://dx.doi.org/10.1038/nnano.2012.95

116. Benameur, M.M.*, et al.*, *Visibility of dichalcogenide nanolayers.* Nanotechnology. **22**(12): p. 125706-125706. 2011. http://dx.doi.org/10.1088/0957-4484/22/12/125706

117. Lee, C.*, et al.*, *Anomalous lattice vibrations of single-and few-layer MoS2.* ACS Nano. **4**(5): p. 2695-700. 2010. http://dx.doi.org/10.1021/nn1003937

118. Li, H.*, et al.*, *From bulk to monolayer MoS2: Evolution of Raman scattering.* Advanced Functional Materials. **22**(7): p. 1385-1390. 2012. http://dx.doi.org/10.1002/adfm.201102111

119. Mak, K.F.*, et al.*, *Tightly bound trions in monolayer MoS2.* Nature Materials. **12**(3): p. 207-11. 2013. http://dx.doi.org/10.1038/nmat3505

120. Stewart, T.B. and P.D. Fleischauer, *Chemistry of sputtered molybdenum disulfide films.* Inorganic Chemistry. **21**(6): p. 2426-2431. 1982. http://dx.doi.org/10.1021/ic00136a060

121. Bichsel, R. and F. Levy, *Morphological and Compositional Properties of MoSe2 Films Prepared by R.F. Magnetron Sputtering.* Thin Solid Films. **116**(1): p. 367-372. 1984. http://dx.doi.org/10.1016/0040-6090(85)90031-8

122. Ellmer, K.*, et al.*, *Deposition of c-oriented tungsten disulfide (WS2) films by reactive DC magnetron sputtering from a W-target in Ar/H2S.* Journal of Crystal Growth. **182**(3–4): p. 389-393. 1997. http://dx.doi.org/10.1016/S0022-0248(97)00355-2

123. Wu, S.*, et al.*, *Vapor-Solid Growth of High Optical Quality MoS2 Monolayers with Near-Unity Valley Polarization.* ACS Nano. **7**(3): p. 2768-2772. 2013. http://dx.doi.org/10.1021/nn4002038

124. Liu, K.K.*, et al.*, *Growth of large-area and highly crystalline MoS2 thin layers on insulating substrates.* Nano Letters. **12**(3): p. 1538-1544. 2012. http://dx.doi.org/10.1021/nl2043612

125. Yu, Y.*, et al.*, *Controlled scalable synthesis of uniform, high-quality monolayer and few-layer MoS2 films.* Scientific Reports. **3**: p. 1866-1866. 2013. http://dx.doi.org/10.1038/srep01866

126. Ji, Q.*, et al.*, *Chemical vapour deposition of group-VIB metal dichalcogenide monolayers: engineered substrates from amorphous to single crystalline.* Chemical Society Reviews. p. 2587-2602. 2015. http://dx.doi.org/10.1039/C4CS00258J

127. Lee, Y.H.*, et al.*, *Synthesis of large-area MoS2 atomic layers with chemical vapor deposition.* Advanced Materials. **24**(17): p. 2320-2325. 2012. http://dx.doi.org/10.1002/adma.201104798

128. Najmaei, S., *et al.*, *Vapour phase growth and grain boundary structure of molybdenum disulphide atomic layers.* Nature Materials. **12**(8): p. 754-9. 2013. http://dx.doi.org/10.1038/nmat3673

129. Mann, J., *et al.*, *Facile growth of monolayer MoS2 film areas on SiO2.* European Physical Journal B. **86**(5): p. 2-5. 2013. http://dx.doi.org/10.1140/epjb/e2013-31011-y

130. van der Zande, A.M., *et al.*, *Grains and grain boundaries in highly crystalline monolayer molybdenum disulphide.* Nature Materials. **12**(6): p. 554-61. 2013. http://dx.doi.org/10.1038/nmat3633

131. Dumcenco, D., *et al.*, *Large-area MoS2 grown using H2S as the sulphur source.* 2D Materials. **2**(4): p. 044005-044005. 2015. http://dx.doi.org/10.1088/2053-1583/2/4/044005

132. Dumcenco, D., *et al.*, *Large-Area Epitaxial Monolayer MoS2.* ACS Nano. **10**(1021). 2015. http://dx.doi.org/10.1021/acsnano.5b01281

133. Baek, S.H., Y. Choi, and W. Choi, *Large-Area Growth of Uniform Single-Layer MoS2 Thin Films by Chemical Vapor Deposition.* Nanoscale Research Letters. **10**(1): p. 388-388. 2015. http://dx.doi.org/10.1186/s11671-015-1094-x

134. Plechinger, G., *et al.*, *A direct comparison of CVD-grown and exfoliated MoS2 using optical spectroscopy.* Physical Review Letters. **064008**(100): p. 1-7. 2013. http://dx.doi.org/10.1088/0268-1242/29/6/064008

135. V, K.K., *et al.*, *Predictive approach to CVD of crystalline layers of TMDs: The case of MoS2.* Nanoscale. **7**: p. 7802-7810. 2015. http://dx.doi.org/10.1039/C4NR07080A

136. Kang, K., *et al.*, *High-mobility three-atom-thick semiconducting films with wafer-scale homogeneity.* Nature. **520**(7549): p. 656-660. 2015. http://dx.doi.org/10.1038/nature14417

137. Jang, Y., *et al.*, *Wafer-scale, conformal and direct growth of MoS2 thin filmsby atomic layer deposition.* Applied Surface Science. **365**: p. 160-165. 2016. http://dx.doi.org/10.1016/j.apsusc.2016.01.038

138. Zhan, Y., *et al.*, *Large-area vapor-phase growth and characterization of MoS2 atomic layers on a SiO2 substrate.* Small. **8**(7): p. 966-971. 2012. http://dx.doi.org/10.1002/smll.201102654

139. Laskar, M.R., *et al.*, *Large Area Single Crystal (0001) Oriented MoS2 Thin Films.* Applied Physics Letters. **102**: p. 252108-252108. 2013. http://dx.doi.org/10.1063/1.4811410

140. Lee, Y., *et al.*, *Synthesis of wafer-scale uniform molybdenum disulfide films with control over the layer number using a gas phase sulfur precursor.* Nanoscale. **6**(5): p. 2821-6. 2014. http://dx.doi.org/10.1039/c3nr05993f

141. Gatensby, R., *et al.*, *Controlled synthesis of transition metal dichalcogenide thin films for electronic applications.* Applied Surface Science. **297**: p. 139-146. 2014. http://dx.doi.org/10.1016/j.apsusc.2014.01.103

142. Orofeo, C.M., *et al.*, *Scalable synthesis of layer-controlled WS2 and MoS2 sheets by sulfurization of thin metal films.* Applied Physics Letters. **105**: p. 083112-083112. 2014. http://dx.doi.org/10.1063/1.4893978

143. Liu, H., *et al.*, *Towards large area and continuous MoS2 atomic layers via vapor-phase growth: thermal vapor sulfurization.* Nanotechnology. **25**(40): p. 405702-405702. 2014. http://dx.doi.org/10.1088/0957-4484/25/40/405702

144. Lin, Y.-C., *et al.*, *Wafer-scale MoS2 thin layers prepared by MoO3 sulfurization.* Nanoscale. **4**(20): p. 6637-6637. 2012. http://dx.doi.org/10.1039/c2nr31833d

145. Wang, X., *et al.*, *Controlled Synthesis of Highly Crystalline MoS2 Flakes by Chemical Vapor Deposition.* Journal of the American Chemical Society. **135**: p. 5-8. 2013. http://dx.doi.org/10.1021/ja4013485

146. Han, G.H., *et al.*, *Seeded growth of highly crystalline molybdenum disulphide monolayers at controlled locations.* Nature Communications. **6**: p. 6128-6128. 2015. http://dx.doi.org/10.1038/ncomms7128

147. Sun, D., *et al.*, *Chemical vapor deposition growth of a periodic array of single-layer MoS2 islands via lithographic patterning of an SiO2/Si substrate.* 2D Materials. **2**(4): p. 045014-045014. 2015. http://dx.doi.org/10.1088/2053-1583/2/4/045014

148. Vogt, P., *et al.*, *Silicene: Compelling Experimental Evidence for Graphenelike Two-Dimensional Silicon.* Physical Review Letters. **108**(15): p. 155501-155501. 2012. http://dx.doi.org/10.1103/PhysRevLett.108.155501

149. Acun, A., *et al.*, *Germanene: the germanium analogue of graphene.* Journal of Physics: Condensed Matter. **27**(44): p. 443002-443002. 2015. http://dx.doi.org/10.1088/0953-8984/27/44/443002

150. Tao, L., *et al.*, *Silicene field-effect transistors operating at room temperature.* Nature Nanotechnology. **10**(3): p. 227-231. 2015. http://dx.doi.org/10.1038/nnano.2014.325

151. Kara, A., *et al.*, *A review on silicene - New candidate for electronics.* Surface Science Reports. **67**(1): p. 1-18. 2012. http://dx.doi.org/10.1016/j.surfrep.2011.10.001

152. Dávila, M.E. and G. Le Lay, *Few layer epitaxial germanene: a novel two-dimensional Dirac material.* Scientific Reports. **6**(August 2015): p. 20714-20714. 2016. http://dx.doi.org/10.1038/srep20714

153. Dávila, M.E., *et al.*, *Germanene: A novel two-dimensional germanium allotrope akin to graphene and silicene.* New Journal of Physics. **16**: p. 095002-095002. 2014. http://dx.doi.org/10.1088/1367-2630/16/9/095002

154. Zhu, F.-F., *et al.*, *Epitaxial growth of two-dimensional stanene.* Nature Materials. **14**: p. 1020-1025. 2015. http://dx.doi.org/10.1038/NMAT4384

155. Bianco, E., *et al.*, *Stability and Exfoliation of Germanane: A Germanium Graphane Analogue.* ACS Nano. **7**(5): p. 4414-4421. 2013. http://dx.doi.org/10.1021/nn4009406

156. Jiang, S., *et al.*, *Improving the stability and optical properties of germanane via one-step covalent methyl-termination.* Nature Communications. **5**: p. 3389-3389. 2014. http://dx.doi.org/10.1038/ncomms4389

157. Arguilla, M.Q., *et al.*, *Synthesis and Stability of Two-Dimensional Ge/Sn Graphane Alloys.* Chemistry of Materials. **26**: p. 6941-6946. 2014. http://dx.doi.org/10.1021/cm502755q

158. Jiang, S., *et al.*, *Covalently-controlled properties by design in group IV graphane analogues.* Accounts of Chemical Research. **48**(1): p. 144-151. 2015. http://dx.doi.org/10.1021/ar500296e

159. Xu, Y., *et al.*, *Large-Gap Quantum Spin Hall Insulators in Tin Films.* Physical Review Letters. **111**(13): p. 136804-136804. 2013. http://dx.doi.org/10.1103/PhysRevLett.111.136804

160. Liu, C.C., W. Feng, and Y. Yao, *Quantum spin Hall effect in silicene and two-dimensional germanium.* Physical Review Letters. **107**(7): p. 1-4. 2011. http://dx.doi.org/10.1103/PhysRevLett.107.076802

161. Restrepo, O.D., *et al.*, *Tunable gaps and enhanced mobilities in strain-engineered silicane.* Journal of Applied Physics. **115**(3). 2014. http://dx.doi.org/10.1063/1.4860988

162. Pinchuk, I.V., *et al.*, *Epitaxial co-deposition growth of CaGe2 films by molecular beam epitaxy for large area germanane.* Journal of Materials Research. **29**(03): p. 410-416. 2014. http://dx.doi.org/10.1557/jmr.2014.2

163. Vogg, G., *et al.*, *Epitaxial alloy films of Zintl-phase Ca(Si1−xGex)2.* Journal of Crystal Growth. **223**(4): p. 573-576. 2001. http://dx.doi.org/10.1016/S0022-0248(01)00686-8

164. Slotman, G.J. and A. Fasolino, *Structure, stability and defects of single layer hexagonal BN in comparison to graphene.* Journal of Physics: Condensed Matter. **25**(4): p. 045009-045009. 2013. http://dx.doi.org/10.1088/0953-8984/25/4/045009

165. Song, L., *et al.*, *Large scale growth and characterization of atomic hexagonal boron nitride layers.* Nano Letters. **10**(8): p. 3209-3215. 2010. http://dx.doi.org/10.1021/nl1022139

166. Liu, H., *et al.*, *Phosphorene : An Unexplored 2D Semiconductor with a High Hole Mobility.* ACS Nano. **8**(4): p. 4033-4041. 2014. http://dx.doi.org/10.1021/nn501226z

167. Li, L., *et al.*, *Black phosphorus field-effect transistors.* Nature Nanotechnology. **9**(5): p. 1-17. 2014. http://dx.doi.org/10.1038/nnano.2014.35

168. Kim, J.-S., *et al.*, *Toward air-stable multilayer phosphorene thin-films and transistors.* Scientific Reports. **5**: p. 8989-8989. 2015. http://dx.doi.org/10.1038/srep08989

169. Kou, L., C. Chen, and S.C. Smith, *Phosphorene: Fabrication, Properties, and Applications.* The Journal of Physical Chemistry Letters. **6**(14): p. 2794-2805. 2015. http://dx.doi.org/10.1021/acs.jpclett.5b01094

170. Geim, A.K. and I.V. Grigorieva, *Van der Waals heterostructures.* Nature. **499**(7459): p. 419-25. 2013. http://dx.doi.org/10.1038/nature12385

171. Niu, T. and A. Li, *From two-dimensional materials to heterostructures.* Progress in Surface Science. **90**(1): p. 21-45. 2015. http://dx.doi.org/10.1016/j.progsurf.2014.11.001

172. Lotsch, B.V., *Vertical 2D Heterostructures.* Annual Review of Materials Research. **45**(1): p. 85-109. 2015. http://dx.doi.org/10.1146/annurev-matsci-070214-020934

173. Lee, C.-H., *et al.*, *Atomically thin p–n junctions with van der Waals heterointerfaces.* Nature Nanotechnology. **9**(9): p. 676-681. 2014. http://dx.doi.org/10.1038/nnano.2014.150

Chapter 3: Electronic Transport in Germanane[1]

The synthesis of germanane (GeH) has opened the door for covalently-functionalizable two-dimensional materials in electronics. Herein, we demonstrate that GeH can be electronically doped by incorporating stoichiometric equivalents of phosphorus dopant atoms into the $CaGe_2$ precursor. The electronic properties of these doped materials show significant atmospheric sensitivity, and we observe a reduction in resistance by up to three orders of magnitude when doped samples are measured in water-containing atmospheres indicating that this reduction is likely a result of water activation of the phosphorus dopants. Transport measurements in different contact geometries show a significant anisotropy between in-plane and out-of-plane resistances, with a much larger out-of-plane resistance. These measurements along with finite element modeling results predict that the current distribution in top contacted crystals is restricted to only the topmost, water activated crystal layers. Taken together, these results pave the way for future electronic and optoelectronic applications utilizing group IV graphane analogues.

Bulk GeH crystals were synthesized Nick Cultrara, Maxx Arguilla, Basant Chitara, and Fan Fan of the Goldberger Group at The Ohio State University. Molecular beam epitaxy

[1] The contents of Sections 3.1-3.5 were published in Journal of Physics: Condensed Matter, **28**, 34001 (2016). [174]

$CaGe_2$ was grown by Jinsong Xu and Jyoti Katoch from the Roland Kawakami group at The Ohio State University and the Cross-sectional transmission electron microscopy (TEM) was performed by the David McComb group at The Ohio State University Center for Electron Microscopy and Analysis (CEMAS). I performed electrical measurements and finite element analysis of the bulk synthesized GeH samples, and structural characterization of the MBE grown samples.

3.1 Introduction

Over the past decade, there has been considerable scientific interest focused around the unique properties and device applications of single sheet and multilayered van der Waals materials [10, 110, 175-178]. When exfoliated or grown as single atomic layers, many of these two-dimensional (2D) materials exhibit electronic and optoelectronic properties that differ fundamentally from those of the parent bulk materials [2, 179]. These changes are indicative of the electronic coupling that arises between the neighboring layers of these bulk crystals. For instance, single-layered graphene exhibits the quantum Hall effect at room temperature. This is not seen in its bulk counterpart, graphite, and demonstrates graphene's high-mobility two-dimensional electronic structure [15]. Additionally, the normally indirect band gaps of the group VIB layered transition metal dichalcogenides, such as MoS_2, transform into direct band gaps only when exfoliated or grown as single layers [92, 94, 95, 180]. This dramatic contrast between single- and multi-layered 2D crystals implies that there exists significant coupling between the different layers. In contrast, a material where this interlayer coupling is strongly suppressed or can be

manipulated would enable observation of these exotic 2D phenomena even in relatively thick multilayered crystals.

The Si/Ge/Sn graphane analogues are a unique class of van der Waals materials that feature a 2D electronically active main group lattice in which every atom is terminated with a covalent ligand [155-157, 181]. This covalent termination serves to dramatically suppress band dispersion in the out-of-plane direction as compared to previously studied van der Waals materials. Furthermore, varying the identity of the covalently terminated ligand enables tuning of the in-plane and out-of-plane electronic and thermal transport behavior, optical properties, thermal stability, and topological phases in these materials [86, 155, 159, 182]. The recent development of a facile approach to the synthesis of Ge graphane analogues has resulted in mm-scale crystals of both hydrogen-terminated germanane (GeH) and methyl-terminated germanane ($GeCH_3$) [155, 156, 162]. Hydrogen-terminated germanane is of particular interest due to the predictions of a room temperature phonon-limited electron mobility of 18 000 $cm^2V^{-1}s^{-1}$—a value approximately five times larger than the mobility in bulk Ge—and a direct bandgap of 1.59 eV. Density functional theory predicts little change in the electronic structure between an isolated sheet of GeH, and the two-layer unit cell [155]. Consequently, there is only a weak electronic coupling between crystal layers. Therefore, the high mobility and direct band gap are predicted to exist both in exfoliated flakes and in the bulk crystalline material. While studies on electronic transport in silicene and related silicon based graphane analogues exist, to date there have been none on the germanium based graphane analogues [150, 183].

Herein, we measure the electrical transport properties of GeH through measurements on both undoped and phosphorous doped GeH multilayer crystals. Dopants are incorporated into the GeH lattice by first integrating stoichiometric equivalents of the elemental dopants into the precursor $CaGe_2$ Zintl phase. The effectiveness of this phosphorous doping is verified by observation of a reduction in sheet resistance by up to three orders of magnitude. There is also a significant anisotropy between electronic transport parallel and perpendicular to the layered structure. Additionally, there is a strong atmospheric dependence in the resistance, with the sample resistance decreasing when water vapor is present in the environment. These results, combined with a finite element analysis of the transport in GeH, are used to extract the in-plane and out-of-plane resistivities and to model the current distribution in GeH crystals. This suggest that the sample current flows primarily through the outermost layers due to dopant activation by the water vapor present in the environment. This dopant activation results in a modeled resistivity four orders of magnitude smaller than those calculated in vacuum.

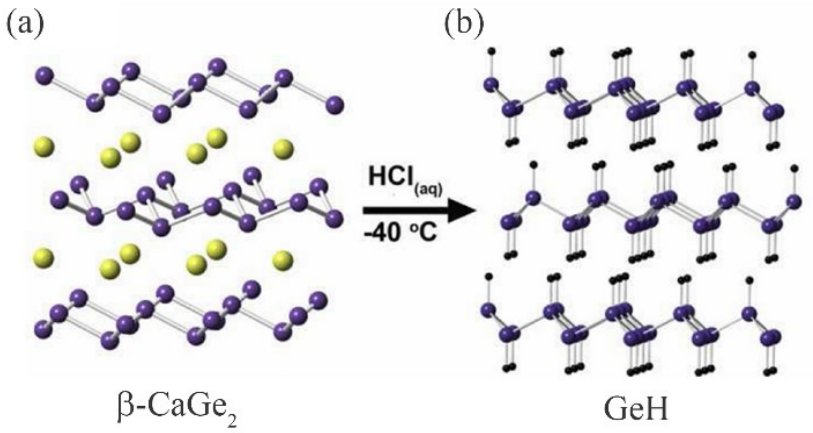

Figure 3.1 *GeH Synthesis*

Schematic diagram of to topotactic deintercalation of the Zintl phase $CaGe_2$ (a) to form GeH (b).

3.2 Experimental Methods

3.2.1 Germanane Synthesis

The synthesis of Germane is achieved using a two-step process [155]. Initially the β-$CaGe_2$ (Zintl phase) is synthesized typically via either bulk crystal growth (see Section 3.2.2) [155], or MBE growth (see Section 3.7.1) [162, 163]. Subsequently, this precursor is immersed in concentrated hydrochloric acid (HCl) during which the soluble $CaCl_2$ is deintercalated from the $CaGe_2$ crystal, forming the van der Waals bonded GeH material. The crystal structure of the resulting GeH follows the existing crystal structure of the $CaGe_2$ crystals resulting in a layered crystalline material where each layer is a 2D sheet of buckled Ge atoms, with each atom terminated covalently by a hydrogen atom. This transformation known as topotactic deintercalation and is shown schematically in **Figure 3.1**.

3.2.2 Bulk Flake Synthesis

Transport measurements are primarily conducted on GeH crystals synthesized via a bulk flake synthesis. These single-crystalline platelets of GeH were synthesized using methods previously reported [155]. In brief, the layered $CaGe_2$ Zintl phase precursor was produced by annealing a stoichiometric ratio of calcium and germanium in a sealed quartz tube at 950-1050 °C under vacuum. The samples were subsequently cooled over the course of 2-10 days. The $CaGe_2$ crystals were then converted to GeH by treatment in concentrated HCl for 5-14 days at -40 °C. This process yielded GeH crystals which measure up to 4 mm laterally and have a thickness of 5-20 μm. To tune the electronic properties of the resulting GeH, phosphorous was used as an extrinsic n-type dopant. Phosphorous doped GeH crystals (P:GeH) were obtained by incorporating stoichiometric amounts of phosphorous—0.5 and 1.0% atomic percentage—to the initial Ca/Ge mixture, and sealed in an evacuated quartz tube. Again, these samples were annealed at 950-1050 °C for 18 hours, and cooled to room temperature of the course of 2-10 days. These P:$CaGe_2$ crystals were then converted to P:GeH by treatment in concentrated HCl for 5-14 days at -40 °C.

3.2.3 Physical and Optical Characterization

The crystallinity of the resulting GeH and P:GeH crystals was confirmed via powdered x-ray diffraction (XRD), Raman spectroscopy, and scanning electron microscopy (SEM). XRD was performed on a Bruker D8 powder X-ray diffractometer with Cu Kα radiation. The Raman scattering spectra were collected on a Renishaw InVia Raman equipped with a CCD detector using a 633 nm He-Ne laser as excitation. The SEM micrographs were

taken using a FEI Helios Nanolab 600 dual beam focused ion beam and scanning electron microscope at current of 43 pA and voltage of 10 kV.

3.2.4 Device Synthesis

Top-contacted GeH samples were fabricated by electron-beam deposition of Ag/Au (100/20 nm) through a shadow mask, creating a 25 μm channel between the two contacts. Depositions were conducted with the sample at room temperature to avoid amorphization which occurs above 75 °C [155]. Silver (with a gold capping layer to prevent oxidation) was selected as a contact metal after showing that the silver contacts on P:GeH had smaller resistances and linear IV curves indicating a low contact resistance and minimal Schottky barrier. Other metals tested were Ti/Au, Au, Pd, Cr, and Pt. Connections to the electron beam deposited sample contacts were made by connecting thin Au wires to the deposited contacts using Ag epoxy. The out-of-plane samples were fabricated by placing a drop of Ag epoxy on a SiO_2/Si substrate (300 nm SiO_2), setting the GeH sample on top of this epoxy, and then placing a second epoxy spot on the top of the GeH. Here again, Au wire was used to make contact to the epoxy contacts.

3.2.5 Electronic Transport

Transport current-voltage scans were measured using a Keithley 4200-SCS, using a probe station manufactured by Lake Shore Cryotronics Inc. (Westerville, OH). Unless otherwise noted, all IV curves are measured in ambient atmosphere, at room temperature, and in a dark environment (to prevent photo-excited carrier contributions to the conductivity). Due

the high (>100 GΩ) sample resistance observed here, triaxial cables (with the center conductor acting as a guard for the measurements) in order to prevent current leakage in the measurement.

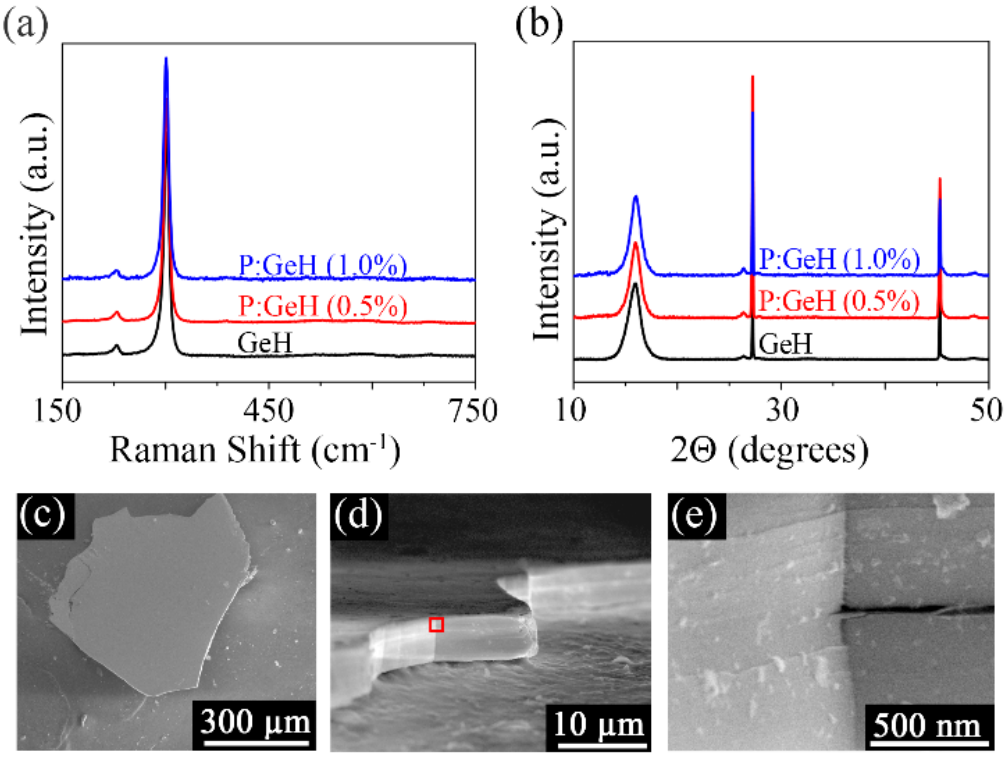

Figure 3.2 *Sample Characterization.*

Raman (a) and XRD (b) spectra of HCl deintercalated GeH with 0.0% (undoped, black), 0.5% (red), and 1.0% (blue) phosphorous incorporation in the CaGe2 precursor. (c-e) SEM images of the bulk GeH crystals.

3.3 Results and Discussion

3.3.1 Sample Characterization

The purity of the resulting P:GeH crystals is confirmed through X-ray crystal diffraction (XRD) and Raman spectroscopy (**Figure 3.2**(a) and (b)). The samples can be indexed to a

hexagonal unit cell with $a = 3.880$ Å and $c = 11.04$ Å (two GeH layers per c-unit cell spacing), consistent with previous measurements [155, 162]. The absence of extra peaks in the XRD spectra indicate the absence of crystalline impurity phases within the resolution of our measurement system. There are also no significant changes in the lattice parameters for the doped samples. The Raman spectra of the GeH and P:GeH samples show the expected E_2 mode at 302 cm^{-1} as well as the A_1 mode at 228 cm^{-1} with no discernable changes in peak-shape or position [155, 162]. Scanning electron micrographs (**Figure 3.2**(c), (d), and (e)) of the GeH crystals confirm that they are smoothly faceted with no visible gaps between the GeH sheets.

3.3.2 Atmospheric Dependence and Anisotropy of Resistance Measurements

In bulk crystalline samples of 2D materials such as single-crystal Kish graphite and MoS_2, there is typically a strong anisotropy (ranging from 2-6 orders of magnitude) between resistivity in the plane of the 2D sheets and between the sheets [8, 183-185]. In order to probe this anisotropy, as well as the effectiveness of the P dopants, two different contact geometries were employed to measure current-voltage (IV) scans. The in-plane (IP) conductivity was probed through the use of a top contact (TC) geometry (**Figure 3.3**(a) and (b) inset), while an out-of-plane (OOP) geometry (**Figure 3.3**(c), (d) inset) was used to measure the interplane resistivity.

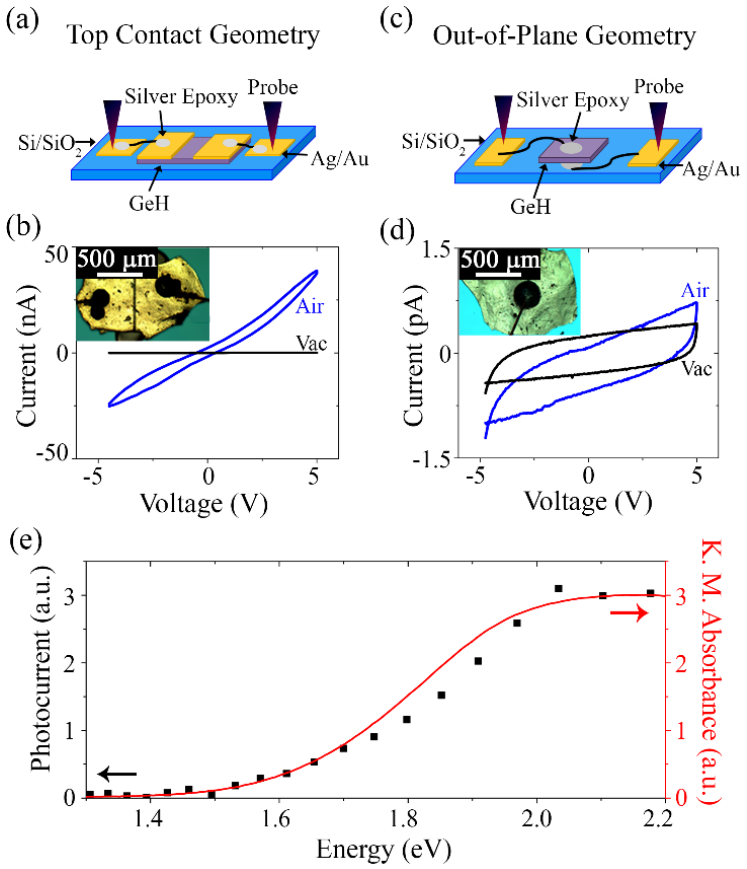

Figure 3.3 *Flake Transport.*

Schematics of the top-contact (a) and out-of-plane (c) geometries used to study the transport properties in GeH crystals. (b) and (d) show representative IV curves both in ambient atmospheric conditions (blue) and in a vacuum of 5×10^{-4} mbar (black). Out-of-plane measurements are at the lower limit of the hardware setup. Insets show characteristic micrographs of samples (e) Photocurrent as a function of light energy which matches the absorbance curve from Bianco *et al.* showing an increase in conductivity with exposure to above bandgap light [16].

Representative IV curves for TC and OOP geometries are shown in **Figure 3.3**(b) and (d), respectively (data shown here for 0.5% P:GeH). In addition to the large difference in resistances between the two contact geometries (extracted from the slopes of the IV curves), there is also a variation in the sensitivity of the two measurements to the environmental conditions. In particular, measurements conducted on TC devices show an increase in current by three orders of magnitude when exposed to the ambient atmosphere

compared to measurements under a vacuum of 5×10^{-4} mbar. In contrast, the OOP devices experience almost no change in resistivity as both vacuum and ambient atmosphere measurements exhibit currents at the lower limit of the hardware setup. This lack of variation could be due to an absence of atmospheric sensitivity in the OOP conduction, or the magnitude of this change is beyond our current sensitivity. To confirm that the observed TC geometry's low current signals are generated by transport through the P:GeH crystal rather than through parallel conduction channels such as the substrate or a surface water layer, variable wavelength photoconductivity measurements were performed at light energies of 1.2-2.2 eV under vacuum. **Figure 3.3**(e) shows the photocurrent signal (black data) on top of the diffuse reflectance absorption measured previously by Bianco *et al.* in GeH (red data) [155]. The increase in photocurrent at wavelengths above the 1.59 eV bandgap correlates well with the absorption spectra and confirms that the current measured is due to conduction inside the P:GeH samples.

Since the photoconductivity measurement confirms that the conduction is occurring in the GeH crystal, the atmospheric dependence observed in the TC geometry suggests that a component of the ambient atmosphere may be activating dopants on the surface of the P:GeH crystals. **Figure 3.4** shows the positive voltage I-V scans for a prototypical 0.5% P:GeH sample in the TC geometry upon exposure to a variety of atmospheres. Though not shown here, negative scans show similar behavior. The sample was first measured in air and then the chamber was pumped down to a vacuum of 5×10^{-4} mbar for a second measurement. The chamber was subsequently backfilled to atmospheric pressure with Ar, O_2, and 32 mbar water in argon mixture (H_2O/Ar). The system was pumped down to the

base pressure after each gas exposure. On exposure to both air and water vapor, the maximum current increased as compared to the vacuum, Ar, and O_2 I-V scans. These measurements demonstrate that the component of the ambient atmosphere responsible for the decreased resistivity signal in the TC measurements is the water vapor.

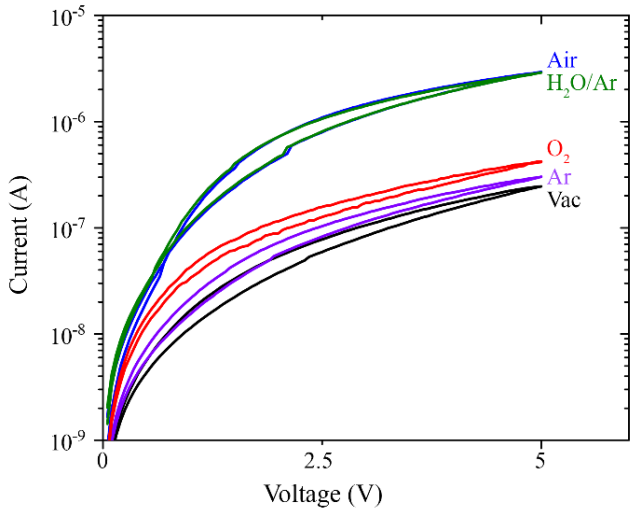

Figure 3.4 *Atmospheric Dependent Transport.*

Representative positive voltage I-V curves showing the atmospheric dependence of P:GeH using top contact geometry. Samples were exposed to air (blue), water/argon mixture (green), oxygen (red), argon (violet), and vacuum (black). The sample was pumped down to a base vacuum of 5×10^{-4} mbar between measurements. Negative voltage I-V curves are similar and are not shown for clarity.

3.3.3 Doping Dependence

Next the changes in electronic properties in samples with different phosphorous incorporation were probed in both the TC and OOP geometries. We investigate three cases: undoped GeH, 0.5% P incorporation, and 1.0% P incorporation. **Figure 3.5** shows the respective IV curves at different phosphorous incorporations for the TC geometry

(**Figure 3.5**(a)) and the OOP geometry (**Figure 3.5**(b)). The TC devices show an increase in resistance by three orders of magnitude under increased phosphorous doping, while the OOP geometry show no apparent increase. Here again, all of the OOP measurements show currents that are at the lower limits of the hardware. The variation in sheet resistance of the different phosphorous incorporation regimes is shown quantitatively in **Figure 3.5**(c) for the TC measurement geometry. Resistances were extracted from the slope of the best fit line for each I-V with three to five samples measured at each P incorporation value. In order to account for sample-to-sample geometric effects in the extracted resistances, the resistances were converted to sheet resistances. Error bars represent the sample to sample variation observed in the doping series measurements. The lack of doping dependence in the OOP measurements suggests either that the IP geometry change is dominated by the exposure to water vapor (which may indicate that the IP geometry is particularly sensitive to the outermost, water-activated layers), or that any doping dependence is just outside of the range of the hardware to observe.

While the large resistance anisotropy of the TC and OOP contact geometries is a useful metric, the intrinsic in-plane and out-of-plane resistivities (ρ_x and ρ_z, respectively) and the anisotropy ($A = \rho_z/\rho_x$) between them provide insight into the inter- and intra-layer coupling of the material. The OOP resistivity (ρ_z) can be extracted directly from the OOP measurement geometry using the standard equation for uniformly distributed current flow inside a material:

$$\rho_z = R_{OOP}\left(\frac{WL}{T}\right)$$

where R_{OOP} is the resistance measured in the OOP geometry, W and L are the two in-plane sample dimensions, and T is the out of plane thickness of the sample. Since the OOP geometry measurements exhibit a current signal at the limit of our hardware, only a lower bound of $\rho_z \geq 5\times10^{14}\ \Omega \cdot \text{cm}$ can be calculated for all three doping regimes. This value is comparable to that measured previously in half hydrogen and half hydroxide terminated silicane [$SiH_{0.5}(OH)_{0.5}$] at 250 °C [183].

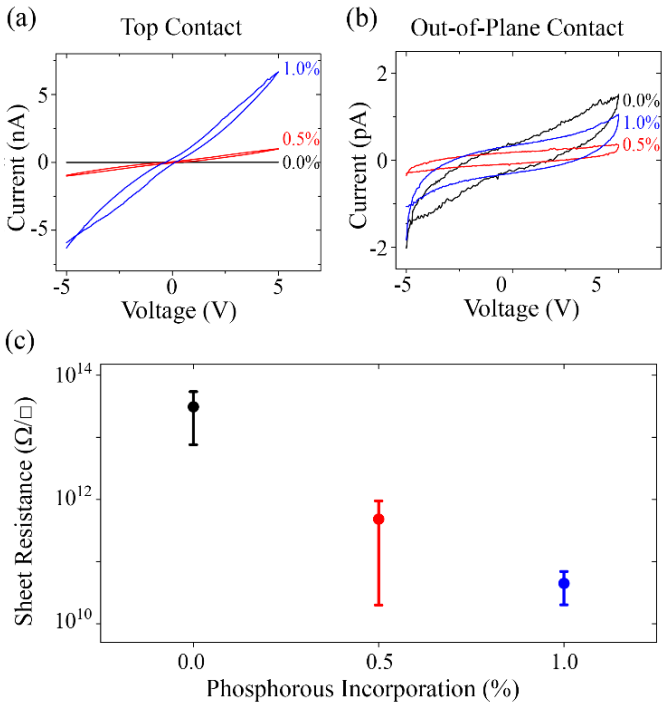

Figure 3.5 *Doping Dependence of P:GeH.*

Doping dependence of GeH samples with 0.0% (black data), 0.5% (red data), and 1.0% (blue) incorporation of phosphorous in the $CaGe_2$ precursor. Representative I-Vs in the top-contact (a) and out-of-plane (b) geometries. Out-of-plane I-Vs show a signal below the limits of the hardware setup. (c) Sheet resistances in top-contact geometry for different doping regimes. Error bars represent the sample to sample variation.

On the other hand ρ_x cannot be directly extracted from the TC geometry measurements due to the non-uniformity of the current distribution which is a combination of in-plane and out-of-plane current paths. Further, the strong atmospheric dependence observed in the TC geometry implies transport in this geometry is more sensitive to the surface of the sample (and hence ρ_x) than it is to the bulk of the sample (and ρ_z). This suggests an anisotropy between ρ_x and ρ_z that is partially due to the atmospheric activation of dopants present in the samples. In order to probe this current distribution in the TC measurement and to place bounds on ρ_x (and hence the anisotropy between ρ_x and ρ_z), we developed a finite element model of transport inside of multilayered 2D materials.

3.4 Finite Element Modelling of In-Plane Resistivity

3.4.1 Model Description

The finite element model used here is illustrated in **Figure 3.6**(a). The bulk crystal is modeled by a network of in-plane and out-of-plane resistors with resistances R_x and R_z, respectively. This simple model can be modified to incorporate two materials with different internal resistance values by stacking blocks of materials on top of each other, each with their own internal resistances. We use primed variables to refer to the resistances (R_x' and R_z') in the top material block, and unprimed variables (R_x and R_z) to note the resistances in the lower block. This network of resistors can then be solved for the equivalent sheet resistance of the complete network. The values of network resistors are tuned in order to match this equivalent sheet resistance to the measured sheet resistance. Additionally, this model yields the voltage at each node and the current across the resistors

between nodes. The input model resistances R_x and R_z for both layers can be directly related to the physical resistivities of the materials of the different blocks (ρ_x and ρ_z) through the relations:

$$R_x = \rho_x\left(\frac{l}{t \cdot w}\right) \quad \text{and} \quad R_z = \rho_z\left(\frac{t}{l \cdot w}\right)$$

where $l, t,$ and w are the physical cell dimensions used to describe the model. In the case of GeH, we let $l = t = 0.6$ nm—the thickness of a physical GeH sheet—and let w be the width of the samples themselves. This network of resistors is examined using Kirchhoff's circuit laws to generate a set of linear equations which are solved for the voltage at each node, the current across each resistor, and the equivalent sheet resistance of the network as a whole (which is equivalent to the sheet resistance measured in the top-contact geometry, R_{TC}). The model was implemented using National Instruments (NI) LabVIEW software along with NI's multicore analysis and sparse matrix toolkit. We apply this model to the 0.5% P:GeH measurements.

3.4.2 Modeling Results

To extract the in-plane resistivity (ρ_z) of the P:GeH samples, R_z is held constant while R_x is varied until the equivalent resistance of the modeled network matches the sheet resistance measured in the TC geometry (R_{TC}). The vacuum measurements (black curves in **Figure 3.3**(b) and (d)) are modeled using a single block of material. Using the sheet resistance measured in the TC geometry, $R_{TC} = 1.0 \times 10^{14}$ Ω/□, and the resistivity extracted from OOP geometry measurement, $\rho_z = 5 \times 10^{14}$ Ω · cm, the in-plane resistivity

is found to be $\rho_x = 1.4 \times 10^7\ \Omega \cdot \text{cm}$. This in-plane resistivity is four orders of magnitude smaller than the in-plane resistivity measured in half hydrogen and half hydroxide terminated silicane [SiH0.5(OH)0.5] at 250 °C, and twelve orders of magnitude smaller than its extrapolated room temperature value [183]. Even in this vacuum case, we observe that the samples are nearly 7 orders of magnitude less resistive in the in-plane geometry, suggesting that the interlayer coupling is extremely small in this material.

To model the resistivities of the samples exposed to water vapor (I-V measurements shown in blue curves in **Figure 3.3**(b) and (d)), the two block model is used. Here, the top block is made up of a number of surface layers in which the atmosphere has water activated carriers (assigned values of ρ_x' and ρ_z') while the second block is the non-activated bulk (assigned values of ρ_x and ρ_z). The value for ρ_x and ρ_z are the same values extracted from the vacuum measurements ($\rho_x = 1.4 \times 10^7\ \Omega \cdot \text{cm}$, $\rho_z = 5 \times 10^{14}\ \Omega \cdot \text{cm}$). The values of ρ_x' and ρ_z' are then varied so that the equivalent sheet resistance of the network matches the observed sheet resistance of $R_{TC} = 3.8 \times 10^{10}\ \Omega/\square$. The number of water activated layers is varied in the model as a means of accounting for the surface roughness in the measured samples. Rougher samples are expected to have a higher number of layers exposed to the atmosphere due to the increased surface area, while an atomically smooth sample would only have the single topmost layer exposed to the atmosphere. For this reason, a rougher sample is modeled assuming the top ten layers of GeH are water activated, while a smooth sample assumes only the top layer is water activated.

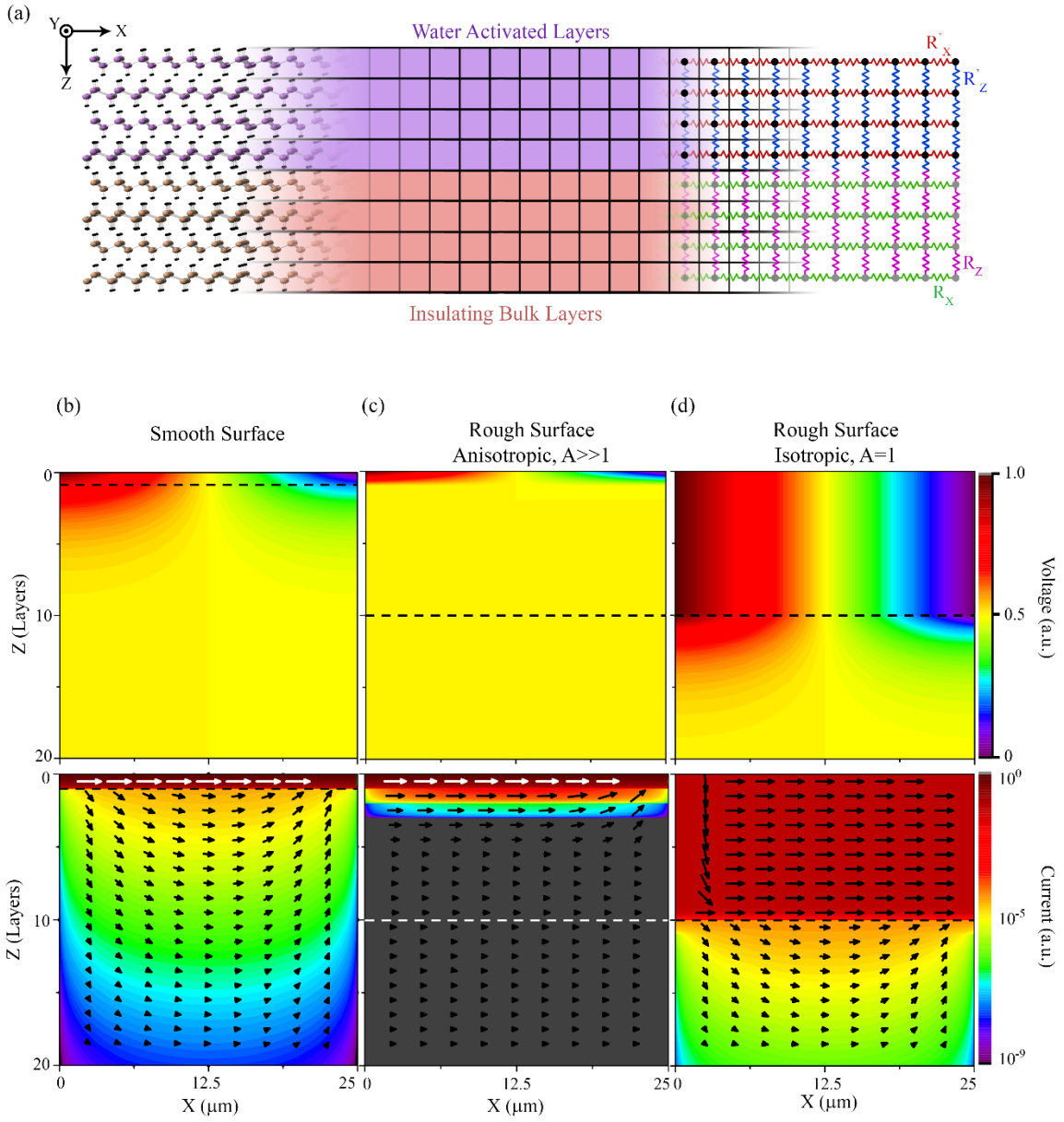

Figure 3.6 *Transport modeling in GeH.*

(a) Cartoon showing the model developed to investigate current flow in a layered, multi-material structure. Material layers are split into cells with dimensions equal to that of a single layer thickness. Material resistances (in-plane and out-of-plane) are input as the pairs R'_x, R'_z and R_x, R_z, and the network of resistors is solved for the voltage at each voltage node (V_n) and the equivalent resistance of the network. Voltage and current maps—top and bottom of (b), (c), and (d), respectively—are shown for a smooth surface (a), a rough surface with anisotropic conductivity in the water activated 0.5% P:GeH block (b), and a rough surface with isotropic conductivity in the water activated P:GeH block (c). The smooth surface is simulated using one single layer of water activated P:GeH, while rough surfaces are simulated with ten layers of water activated P:GeH. Dashed lines distinguish between the upper water activated block, and the bottom non-water activated block of the model.

For the case of an atomically smooth sample we assume that only a single layer of material experiences water activation of dopants, thus there is no ρ'_z value and only ρ'_x is varied until the effective sheet resistance matches the observed sheet resistance. This occurs at $\rho'_x = 2.3 \times 10^3\ \Omega \cdot \text{cm}$. The resultant current and voltage maps for this case are shown in **Figure 3.6**(b). Modeling indicates that in this case, >99% of the current travels solely in this topmost layer. The modeled ρ'_x value is nearly four orders of magnitude smaller than the value derived in the unactivated case ($\rho_x = 1.4 \times 10^7\ \Omega \cdot \text{cm}$), and eleven orders smaller than the out of plane resistivity ($\rho_z = 5 \times 10^{14}\ \Omega \cdot \text{cm}$).

A more realistic view of the P:GeH samples is that the surface is not atomically flat. In this scenario, several layers are exposed to the atmosphere and experience dopant activation. To model this, the top ten layers of the sample are assumed to be water activated. This corresponds to a roughness of 6 nm. While water is unlikely to diffuse through the bulk of the GeH samples and change the OOP resistance measurements, the measured currents in the OOP geometry are below the minimum instrument resolution, making it impossible to verify this hypothesis. Consequently, we chose to model two extreme cases for the for the P:GeH anisotropy, $A = \rho'_z/\rho'_x$. The first assumes no change in ρ'_z compared to the vacuum measurements ($A \gg 1$) so that the water has no effect on the OOP resistivity. The second case assumes a large reduction in ρ'_z due to the water activation ($A = 1$).

For the strong anisotropy ($A \gg 1$) case, $\rho'_z = 5 \times 10^{14}\ \Omega \cdot \text{cm}$, the value calculated from the OOP measurements. Here, $\rho'_x = 2.3 \times 10^3\ \Omega \cdot \text{cm}$, the same as the previously modeled smooth sample. The result for this scenario is shown in **Figure 3.6**(c). Again >99% of the

current flows through the topmost layer. The final case (**Figure 3.6**(d)) again assumes ten layers of water activated GeH, but this time the water activation is taken to increase the interlayer conduction yielding isotropic resistivity values, A = 1. In this case values of $\rho_x' = \rho_z' = 2.3 \times 10^4\ \Omega \cdot \text{cm}$ are extracted from the model. Here, >99% of the current travels inside of the water activated region and is equally distributed throughout these surface layers.

A summary of the modeling results is shown in **Table 3.1**. In all three cases, we find that the value of the in-plane resistivity is bounded $2.3 \times 10^3 < \rho_x' < 2.3 \times 10^4\ \Omega \cdot \text{cm}$, which is 10 - 11 orders of magnitude smaller than the calculated out-of-plane resistivity value of $\rho_z = 5 \times 10^{14}\ \Omega \cdot \text{cm}$. Additionally, >99% of the current is confined to only the water activated layers of the sample in all of the modeled cases.

Table 3.1 *Modeling Summary.*

Summary of modeling results for the cases involving water activated dopants.

Number of Activated Layers	ρ_z' ($\Omega \cdot$ cm)	ρ_x' ($\Omega \cdot$ cm)	A = ρ_z'/ρ_x'
1	5×10^{14}	2.3×10^3	2.2×10^{11}
10	5×10^{14}	2.3×10^3	2.2×10^{11}
10	2.3×10^4	2.3×10^4	1×10^0

3.5 Conclusion

We have grown both doped and undoped GeH crystals and evaluated their transport properties for the first time. By incorporating phosphorous into the synthesis of the $CaGe_2$ precursor, it is possible to electronically dope GeH, leading to a reduction in the sample resistance by up to three orders of magnitude. Electrical transport measurements conducted on bulk crystalline GeH samples using two different contact geometries show a large resistance anisotropy between the in-plane and out-of-plane directions. The resistivity of the crystals exhibit a strong atmospheric dependence with the resistivity decreasing by up to three orders of magnitude when samples are exposed to air. This atmospheric dependence of the resistance, along with the photocurrent measurements suggest that the presence of water vapor in the air is activating dopants on the surface of the P:GeH crystals. The effect of the presence of water increasing surface conductivity has been observed in other materials (particularly in diamond, see Ref. [186]), however to our knowledge this is the first time this effect is observed only in conjunction with a dopant dependence. To better understand the current distribution inside these layered materials, we developed a finite element model which indicates that nearly all of the current travels in the topmost water activated layers. These experimental and modeling results suggest the possibility of the ability to measure exotic single layer properties in the top layer of a multilayered group IV graphane crystal by making electronic contact to the top surface.

3.6 Four-Probe Measurements Exfoliated Flakes

In addition to the electronic transport measurements made on bulk P doped GeH crystals, some initial transport measurements have been made using exfoliated Ga doped GeH (Ga:GeH) flakes. The Ga:GeH samples were chosen for the exfoliated measurements because typically, with bulk top-contacted measurements, this Ga doped material exhibits resistances 1-2 orders of magnitude lower than that of the P:GeH. Work is in progress to further characterize the electronic transport in these Ga doped samples as well as the atmospheric dependence. One of the concerns in the bulk P:GeH measurements is that the transport may be dominated by the contact resistance of the devices. By designing and fabricating Hall-style devices from exfoliated flakes we can measure the 2-probe and 4-probe resistances of the GeH flakes and probe the contact resistance of GeH.

3.6.1 GeH Exfoliation and Device Synthesis

Ga:GeH flakes are exfoliated from bulk Ga doped GeH crystals synthesized using the same method discussed in Section 3.2.1 except that Ga is used as a dopant during the $CaGe_2$ synthesis rather than phosphorous. Flakes are exfoliated from the bulk GeH crystals using polydimethylsiloxane (PDMS). The adhesive PDMS is synthesized by mixing monomer PDMS and a curing agent to homogeneity in a ratio of 8:1. This mixture is then placed in a vacuum until air bubbles are removed from the mixture and subsequently cured at 60-80 °C for 1-2 hours (depending on desired adhesiveness). This PDMS is then used to exfoliate the GeH flakes using similar methods to those used in the exfoliation of other 2D

materials through Kapton or Scotch type tapes. PDMS is used for GeH exfoliation in order to eliminate the residue left by Scotch and Kapton tapes.

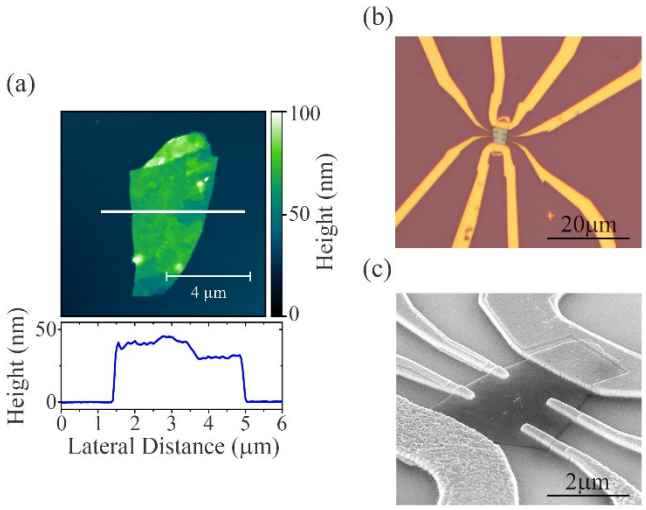

Figure 3.7 *Exfoliated GeH Physical Characteristics*.

AFM image (a) of GeH exfoliated via PDMS on SiO2 substrate. Line cut (bottom) shows thickness and flake roughness at the white line in the top AFM image. (b) Optical micrograph showing the same flake after Hall device synthesis. (c) SEM image showing a second (though representative) flake after the two-stage lithography process. Dark area is the GeH flake, while the lighter areas are Ti/Au and Au contacts shown making good contact to the flake.

Flakes are exfoliated onto Si/SiO_2 substrates with a 300 nm thick oxide layer. Typical flakes are 5-10 μm in lateral dimensions and 20-50 nm thick (roughly 30-80 GeH layers) and an example flake is shown in **Figure 3.7**(a). The Ga doped GeH flakes used in this work were grown by Maxx Arguilla and Nick Cultrara and exfoliated by Fan Fan in the Joshua Goldberger at The Ohio State University.

After the exfoliation, a Hall device is fabricated around the flake using a multi-step electron beam lithographic process. This process is described in full in **Appendix A**. In brief, the substrate is spin coated by a copolymer/PMMA bilayer and baked at a lower

temperature (50 °C) than is typical in order to prevent amorphization which occurs in the GeH flake around 75 °C [155]. After resist deposition, a large area alignment grid is written via electron beam lithography (EBL) which allows for the flake to be geometrically registered on the SiO_2 substrate. Following this, a two-stage EBL and metallization process is carried out. The first stage is EBL of the contact pattern up to but not including those overlapping the GeH flake and metallization with Ti/Au (1.5/50 nm). The second stage is the same EBL pattern, but this time it is extended to the contacts which sit on top of the flake and metalized using only Au (100 nm) as the contact layer. The first stage allows for a strong adhesion of the contacts to the SiO_2 substrate through the use of the Ti sticking layer, while the second keeps this same Ti layer from making direct contact to the GeH flake. This is done because of the determination that a Ti sticking layer between the flake and the Au contacts causes a decrease in the quality of the contact/GeH interface. Immediately before the final Au metal deposition, a 30 second ultraviolet-ozone clean and a 30 second HCl soak are performed to clean any resist residue and etch away any oxidized GeH material from the GeH flake. Optical and SEM micrographs of finished devices are shown in **Figure 3.7**(b) and (c).

3.6.2 Exfoliated GeH Measurement Setup

Current-voltage scans were measured using a Keithley 4200-SCS, using a probe station manufactured by Lake Shore Cryotronics Inc. (Westerville, OH). The 4-Probe voltage was recorded using a Keithly 6430 sub-femptoamp sourcemeter. Here again, measurements are made in atmosphere.

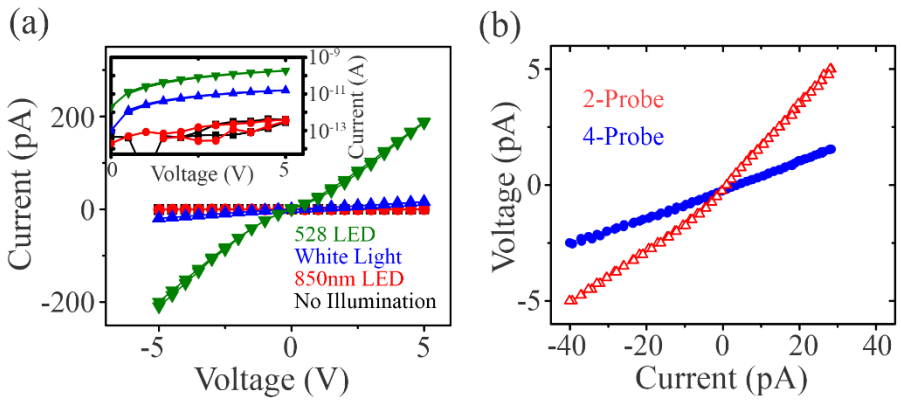

Figure 3.8 *Exfoliated GeH Electronic Characterization.*

(a) displays the 2-probe photoconductivity from the device shown in **Figure 3.7**(b) with no illumination (black), below bandgap illumination (red), above bandgap illumination (green), and white ambient white light illumination (blue). The Inset shows the positive voltage scan of this data on a log scale. (b) 2- and 4-probe IV scans of the same device, made under white light illumination.

3.6.3 Electronic Measurements in Exfoliated GeH

As with the bulk measurements on P:GeH, 2-probe photoconductivity measurements are performed first to demonstrate that current is indeed travelling through the Ga doped GeH flakes. Here, above and below bandgap LEDs and ambient white light are used to illuminate the sample. These IV scans are shown in **Figure 3.8**(a) and demonstrate the increase in current flow in the Ga:GeH flakes by three orders of magnitude when the samples are exposed to above-bandgap light, confirming that transport is indeed occurring in the GeH flake itself.

Using the same device, both 2- and 4-probe IV measurements are taken under white ambient light (**Figure 3.8**(c)). This IV data from the 2-probe measurement shows non-linear behavior indicating a non-Ohmic contact. Additionally, a fit of the linear portions of the datasets indicate resistances of 150 and 60 GΩ respectively. These values are the same order of magnitude indicating that at a maximum, the contact resistance is on the same

order of magnitude as the sample resistance and hence not dominating the transport measurements made on GeH samples.

The maximum current value measured here is ~200 pA which is nearly 2 orders of magnitude smaller than values measured in the bulk P doped GeH measurements. These small currents were present in all GeH flake devices measured (both P and Ga doped), and are considerably smaller than expected based on bulk crystal measurements. One possible cause of this may be the local roughness of the exfoliated flakes and the fact that the contacts are being made to different individual sheets of GeH (See line-cut in **Figure 3.7**(a)). This would imply that the current must travel vertically through different flakes in addition to horizontally through single flakes. The results from the bulk measurements suggest that transport vertically through the flakes would result in an artificially high measurement of the GeH layer resistance in these exfoliated flakes as a result of the extremely weak inter-layer coupling observed in bulk crystal measurements.

This possible effect is being investigated through the use of electrodes that are as closely spaced as possible using current lithography processing capabilities. By placing the contacts very close together we can make electrical contact to a single sheet of GeH and avoid any inter-layer transport from occurring. Resolution limited electrodes with widths of 25 nm and a pitch of 100 nm have been developed (See **Appendix A** and **Figure 3.9**), and future work will involve the synthesis of new exfoliated GeH devices using these electrodes as contacts.

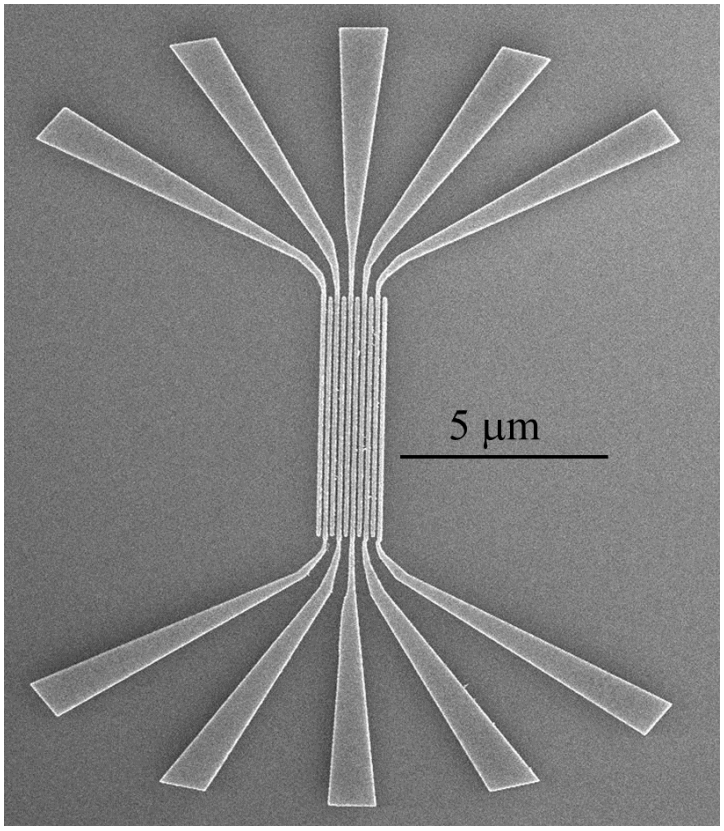

Figure 3.9 *Resolution Spaced Electrodes*.

SEM image of resolution spaced electrodes fabricated through electron beam lithography. Electrodes are 25 nm wide with a pitch of 100 nm.

3.7 MBE Growth of GeH

Overall, the electronic transport in both bulk crystals and exfoliated flakes is of considerably poorer quality than one might expect from a material predicted to have an extremely high mobility [155]. One possible cause for this lack in quality is that the material synthesized by the method described in Section 3.2.1 may result in a large number of defects. One route to solving this problem is to produce a starting material of higher quality via a different method, mainly through molecular beam epitaxy (MBE). The growth of the MBE $CaGe_2$ samples was carried out primarily by Jyoti Katoch and Jinsong Xu of

the Kawakami group. I contributed to this work primarily through the planning process, and the post growth characterization of the material.

3.7.1 MBE Growth Recipe

Growth of GeH via MBE follows the same general theory of synthesis as stated in Section 3.2.1, whereby β-$CaGe_2$ is synthesized first (in this case by MBE) and the $CaGe_2$ thin films are subsequently converted to GeH via topotactic deintercalation. This MBE process is known as "epitopotaxial" and described in detail in Ref. [162]. The $CaGe_2$ is grown epitaxially on top of Ge(111) substrates. To perform this growth, a buffer layer is first grown whose quality is critical to the quality of the resulting $CaGe_2$ growth. Directly after purchase it's not uncommon for the starting Ge(111) substrates to have polishing scratches remaining on the surface (**Figure 3.10**(a)). A high quality buffer layer fills in these scratches and further improve the surface quality, resulting in atomically smooth steps on the Ge(111) substrate (**Figure 3.10**(b)).

Before buffer layer growth, the Ge(111) substrate (0.35 mm thick and 0.5° miscut purchased from University Wafer) is treated chemically cleaned by a 5 minute sonication in deionized (DI) H_2O, a 1 minute etch each in a 10:1 DI H_2O:NH_4OH and 10:1 DI H_2O:H_2SO_4 solutions, and finally a 1 minute oxidation in H_2O_2 to create a new, clean, protective oxide on the Ge surface. After cleaning, the wafer is loaded into the ultrahigh vacuum (UHV) MBE chamber at a base pressure of 2×10^{-10} Torr for an anneal at 650 °C for 30 minutes to desorb the protective oxide layer from the Ge(111) surface. The substrate is then cooled to 180 °C for the buffer layer growth.

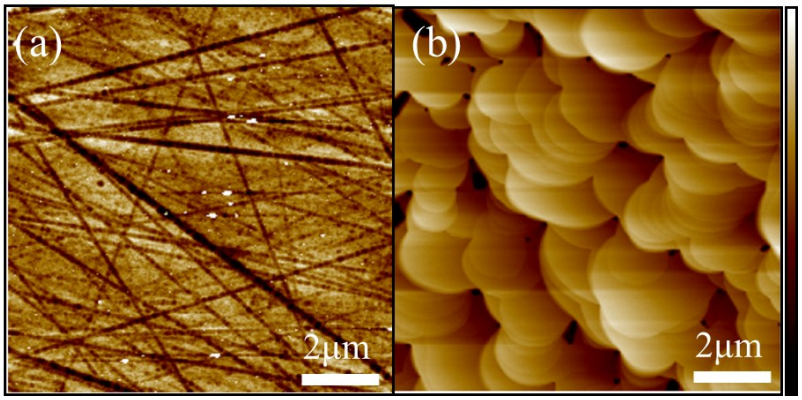

Figure 3.10 *Ge(111) Buffer Layer.*

(a) AFM of Ge(111) substrate prior to buffer layer growth with a z-scale of 8.6 nm. (b) AFM of Ge(111) substrate after buffer layer growth with a z-scale of 14.2 nm.

The buffer layer is grown by depositing Ge (99.9999%, Alfa Aesar) at a rate of 3 Å/min while increasing the substrate temperature from 180 °C to 730 °C at a ramp rate of 5 °C/min. This results in a ~30 nm thick buffer layer of Ge. After the buffer layer growth, the $CaGe_2$ crystal is grown by evaporating elemental Ge and Ca (99.99% Sigma Aldrich) at a flux ratio of 0.7 for Ge:Ca, creating a Ca rich growth environment. The growth takes place at a temperature of 730 °C, a temperature at which any extra elemental Ca is re-evaporated from the $CaGe_2$ surface leaving only $CaGe_2$. Reflected high energy electron diffraction (RHEED) is performed *in-situ* during the growth to monitor the quality of the grown $CaGe_2$ (**Figure 3.11**(a)). After the $CaGe_2$ growth, a 20-100 nm thick capping layer of Co, Py, or Ge is deposited at room temperature on top of the $CaGe_2$ crystal to prevent oxidation once the sample is removed from the UHV MBE chamber.

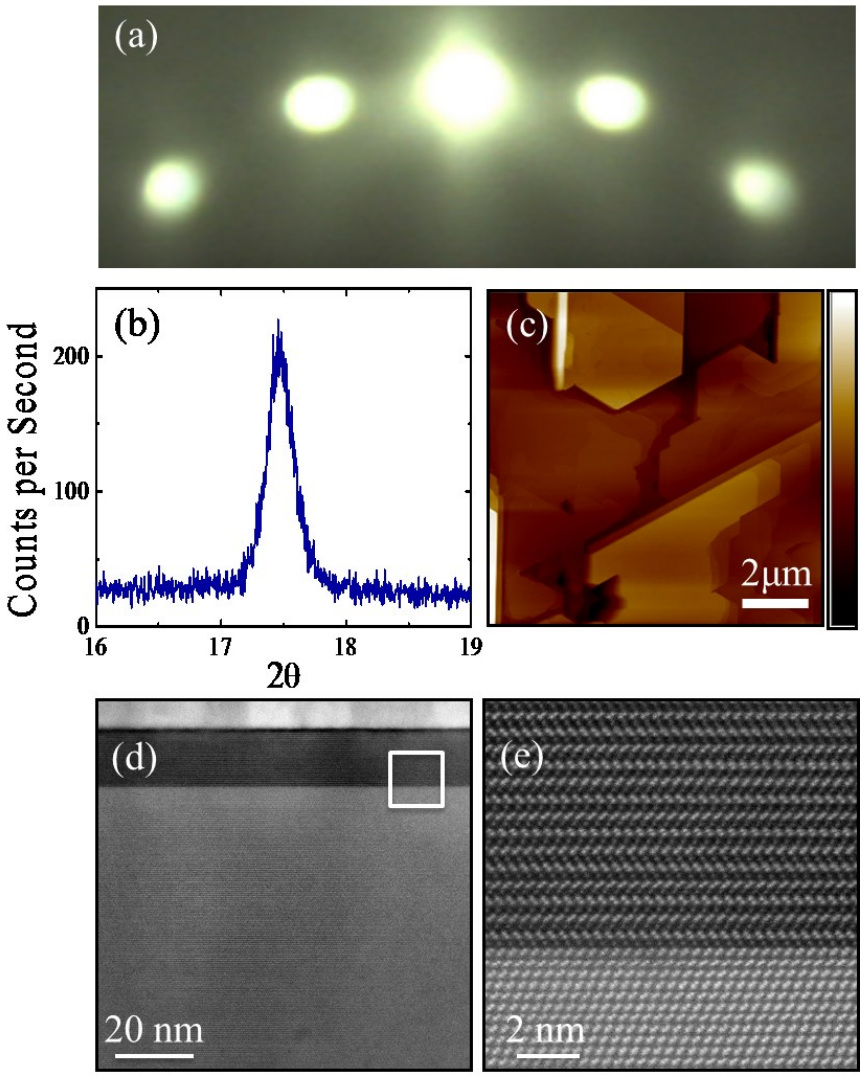

Figure 3.11 *MBE $CaGe_2$ Characterization.*

(a) *in situe* RHEED pattern of MBE $CaGe_2$ growth. (b) XRD of 10nm thick $CaGe_2$ film with 20nm Ge capping layer. (c) AFM of same film in (b) with a z-scale of 56 nm. (d) Cross-sectional TEM along the (001) direction of 5 nm thick $CaGe_2$ film with 20 nm Co capping layer. (e) Zoomed in TEM image of the white boxed region of (d).

3.7.2 MBE Growth Characterization

After sample growth, the $CaGe_2$ is removed from the chamber and post growth characterization is performed. X-ray photoelectron spectroscopy (XPS) is used (**Figure 3.11**(b)) to confirm the c-axis spacing of the crystalline $CaGe_2$ thin film. AFM is

also performed on the surface of the capped $CaGe_2$ film, and indicates an islanded growth mode with large atomically flat islands on the 1-5 μm scale (**Figure 3.11**(c)). The cross-section TEM (shown in **Figure 3.11**(d) and (e)) is notable for the fact that it indicates an extremely high level of crystallinity throughout the $CaGe_2$ sample, showing the crystalline structure expected. This post-growth characterization indicates that the MBE grown $CaGe_2$ is of very high quality on a local scale, but tends to be islanded on the scale of ~10 μm.

3.7.3 MBE Deintercalation and Transport

Some preliminary work has been done on converting MBE $CaGe_2$ to GeH through topotactic deintercalation in HCl, as well as electronic transport on transferred MBE grown GeH [162, 187]. However, the $CaGe_2$ (and subsequent GeH) used for these results was synthesized before the development of a greatly improved Ge buffer layer described here and hence was not as high of quality as the $CaGe_2$ shown in Section 3.7.2. In the future, $CaGe_2$ grown via this high-quality technique will be deintercalated in HCl for crystalline characterization via TEM and XRD, as well as for electronic transport measurements. Finally, a binary, shuttered MBE growth technique is being developed by Jinsong Xu of the Roland Kawakami group. In this technique, the $CaGe_2$ crystal is grown atomic layer by layer. Initial XRD and AFM results indicate a highly-crystalline growth with a thin film growth morphology, rather than island growth features seen above (**Figure 3.12**).

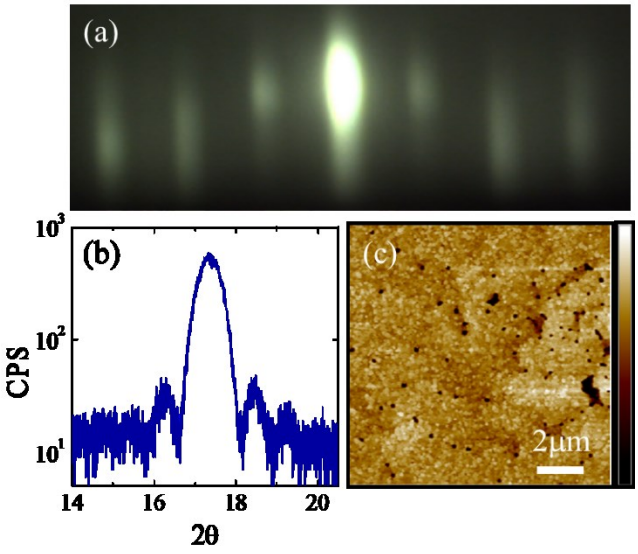

Figure 3.12 *Shuttered MBE $CaGe_2$ Characterization*.

(a) RHEED pattern from 10 nm thick $CaGe_2$ grown via shuttered MBE growth. (b) XRD of the same growth with a 20nm Ge capping layer. (c) AFM of this same growth, showing generally smooth surface (z-scale of 8.5 nm).

The MBE growth of $CaGe_2$ has, thus far, produced extremely high quality crystals, and the recent exploration of a shuttered growth technique has further improved the quality of the material by dramatically smoothing the growth surface. By improving this precursor material, we aim to produce high-quality GeH material, improving upon the transport and optical properties we've already observed and nominally realizing the high mobility of 18 000 $cm^2V^{-1}s^{-1}$ predicted for this material. Further, the development of wafer scale samples through MBE will allow for a wide array of additional studies of this material such as scanning tunneling microscopy, application of standard lithography techniques, and local surface functionalization studies.

3.8 Acknowledgements

Primary support for this work, especially electrical characterization and modeling comes from the Center for Emergent Materials at The Ohio State University, an NSF MRSEC center (Grant DMR-1420451). Partial support for materials synthesis comes from the Army Research Office (Grant W911-NF-12-1-0481).

3.9 References

2. Geim, A.K. and K.S. Novoselov, *The rise of graphene.* Nature Materials. **6**(3): p. 183-191. 2007. http://dx.doi.org/10.1038/nmat1849

8. Das Sarma, S.*, et al.*, *Electronic transport in two-dimensional graphene.* Reviews of Modern Physics. **83**(2): p. 407-470. 2011. http://dx.doi.org/10.1103/RevModPhys.83.407

10. Novoselov, K.S.*, et al.*, *Two-Dimensional Gas of Massless Dirac Fermions in Graphene.* Nature. **438**(7065): p. 197-200. 2005. http://dx.doi.org/10.1038/nature04233

15. Zhang, Y.*, et al.*, *Experimental observation of the quantum Hall effect and Berry's phase in graphene.* Nature. **438**(7065): p. 201-204. 2005. http://dx.doi.org/10.1038/nature04235

86. Butler, S.Z.*, et al.*, *Progress, Challenges, and Opportunities in Two-Dimensional Materials Beyond Graphene.* ACS Nano. **7**(4): p. 2898-2926. 2013. http://dx.doi.org/10.1021/nn400280c

92. Chhowalla, M.*, et al.*, *The chemistry of two-dimensional layered transition metal dichalcogenide nanosheets.* Nature Chemistry. **5**(4): p. 263-75. 2013. http://dx.doi.org/10.1038/nchem.1589

94. Mak, K.F.*, et al.*, *Atomically thin MoS2: a new direct-gap semiconductor.* Physical Review Letters. **105**(13): p. 136805. 2010. http://dx.doi.org/10.1103/PhysRevLett.105.136805

95. Splendiani, A.*, et al.*, *Emerging photoluminescence in monolayer MoS2.* Nano Letters. **10**(4): p. 1271-1275. 2010. http://dx.doi.org/10.1021/nl903868w

110. Radisavljevic, B.*, et al.*, *Single-layer MoS2 transistors.* Nature Nanotechnology. **6**(3): p. 147-150. 2011. http://dx.doi.org/10.1038/nnano.2010.279

150. Tao, L.*, et al.*, *Silicene field-effect transistors operating at room temperature.* Nature Nanotechnology. **10**(3): p. 227-231. 2015. http://dx.doi.org/10.1038/nnano.2014.325

155. Bianco, E.*, et al.*, *Stability and Exfoliation of Germanane: A Germanium Graphane Analogue.* ACS Nano. **7**(5): p. 4414-4421. 2013. http://dx.doi.org/10.1021/nn4009406

156. Jiang, S.*, et al.*, *Improving the stability and optical properties of germanane via one-step covalent methyl-termination.* Nature Communications. **5**: p. 3389-3389. 2014. http://dx.doi.org/10.1038/ncomms4389

157. Arguilla, M.Q.*, et al.*, *Synthesis and Stability of Two-Dimensional Ge/Sn Graphane Alloys.* Chemistry of Materials. **26**: p. 6941-6946. 2014. http://dx.doi.org/10.1021/cm502755q

159. Xu, Y.*, et al.*, *Large-Gap Quantum Spin Hall Insulators in Tin Films.* Physical Review Letters. **111**(13): p. 136804-136804. 2013. http://dx.doi.org/10.1103/PhysRevLett.111.136804

162. Pinchuk, I.V.*, et al.*, *Epitaxial co-deposition growth of CaGe2 films by molecular beam epitaxy for large area germanane.* Journal of Materials Research. **29**(03): p. 410-416. 2014. http://dx.doi.org/10.1557/jmr.2014.2

163. Vogg, G.*, et al.*, *Epitaxial alloy films of Zintl-phase Ca(Si1−xGex)2.* Journal of Crystal Growth. **223**(4): p. 573-576. 2001. http://dx.doi.org/10.1016/S0022-0248(01)00686-8

174. Young, J.R., *et al.*, *Water activated doping and transport in multilayered germanane crystals.* Journal of Physics: Condensed Matter. **28**: p. 34001-34001. 2016. http://dx.doi.org/10.1088/0953-8984/28/3/034001

175. Frindt, R.F., *Superconductivity in Ultrathin NbSe2 Layers.* Physical Review Letters. **28**(5): p. 299-301. 1972. http://dx.doi.org/10.1103/PhysRevLett.28.299

176. Frindt, R.F., *Single Crystals of MoS2 Several Molecular Layers Thick.* Journal of Applied Physics. **37**(4): p. 1928-1929. 1966. http://dx.doi.org/10.1063/1.1708627

177. Allen, M.J., V.C. Tung, and R.B. Kaner, *Honeycomb carbon: a review of graphene.* Chemical Reviews. **110**(1): p. 132-145. 2009. http://dx.doi.org/10.1021/cr900070d

178. Gong, Y., *et al.*, *Vertical and in-plane heterostructures from WS2/MoS2 monolayers.* Nature Materials. **13**(12): p. 1135-1142. 2014. http://dx.doi.org/10.1038/nmat4091

179. Eda, G. and S.A. Maier, *Two-Dimensional Crystals: Managing Light for Optoelectronics.* ACS Nano. **7**(7): p. 5660-5665. 2013. http://dx.doi.org/10.1021/nn403159y

180. Voiry, D., *et al.*, *Covalent functionalization of monolayered transition metal dichalcogenides by phase engineering.* Nature Chemistry. **7**(1): p. 45-49. 2015. http://dx.doi.org/10.1038/nchem.2108

181. Vogg, G., M. Brandt, and M. Stutzmann, *Polygermyne—a prototype system for layered germanium polymers.* Advanced Materials. **12**(17): p. 1278-1281. 2000. http://dx.doi.org/10.1002/1521-4095(200009)12:17<1278::AID-ADMA1278>3.0.CO;2-Y

182. Edman, L., *et al.*, *Electrical resistivity of single-crystal graphite under pressure: An anisotropic three-dimensional semimetal.* Physical Review B. **57**(11): p. 6227-6230. 1998. http://dx.doi.org/10.1103/PhysRevB.57.6227

183. Brandt, M., T. Puchert, and M. Stutzmann, *Electronic transport in crystalline siloxene.* Solid State Communications. **102**(5): p. 365-368. 1997. http://dx.doi.org/10.1016/S0038-1098(97)00010-0

184. Baugher, B.W.H., *et al.*, *Intrinsic electronic transport properties of high-quality monolayer and bilayer MoS2.* Nano Letters. **13**(9): p. 4212-4216. 2013. http://dx.doi.org/10.1021/nl401916s

185. Dresselhaus, M.S. and G. Dresselhaus, *Intercalation compounds of graphite.* Advances in Physics. **30**(2): p. 139-326. 1981. http://dx.doi.org/10.1080/00018738100101367

186. Maier, F., *et al.*, *Origin of Surface Conductivity in Diamond.* Physical Review Letters. **85**(16): p. 3472-3475. 2000. http://dx.doi.org/10.1103/PhysRevLett.85.3472

187. Amamou, W., *et al.*, *Large area epitaxial germanane for electronic devices.* 2D Materials. **2**: p. 035012-035012. 2015. http://dx.doi.org/10.1088/2053-1583/2/3/035012

Chapter 4: Uniform Wafer-Scale Growth of Stencil Templated, High-Quality, Monolayer MoS_2

Over the past decade it has become apparent that the extreme sensitivity of 2D crystals to surface interactions presents a unique opportunity to tune materials properties through surface functionalization and the mechanical assembly of 2D heterostructures. However, this opportunity carries with it a concurrent challenge: an enhanced sensitivity to surface contamination introduced by standard patterning techniques that is exacerbated by the difficulty in cleaning these atomically-thin materials. Here, we report a templated MoS_2 growth technique wherein Mo is deposited onto atomically-stepped sapphire substrates through a SiN stencil with feature sizes down to 100 nm and subsequently sulfurized at high temperature. These films have a quality comparable to the best MoS_2 prepared by other methodologies, and the thickness of the resulting MoS_2 patterns can be tuned layer-by-layer by controlling the initial Mo deposition. The quality and thickness of the films are confirmed by scanning electron and atomic force microscopies as well as Raman and photoluminescence spectroscopies. This approach critically enables the creation of patterned single-layer MoS_2 films with pristine surfaces suitable for subsequent modification via functionalization and mechanical stacking. Further, we anticipate that this growth technique should be broadly applicable within the family of transition metal dichalcogenides.

4.1 Introduction

Two-dimensional (2D) transition metal dichalcogenide (TMD) crystals have attracted extensive attention as next-generation semiconductor materials [10, 86, 91, 170] due to a variety of applications in flexible and transparent electronics [82, 103] and the potential for emergent phenomena due to the interplay of spin and valley degrees of freedom [113, 114, 188]. In particular, MoS_2 has emerged as one of the canonical members of this family with a variety of studies on its electrical, optoelectronic, and mechanical properties [94-101, 110, 189]. For example, bulk crystalline MoS_2 is a semiconductor with an indirect band gap of 1.2 eV [104] while a single layer [83, 105] exhibits a direct-gap of 1.8 eV and locking between the spin and valley degrees of freedom [94, 107, 108, 112, 113]. Recently, considerable work has been done to modify these properties via stacking and functionalization [84, 170, 171, 190, 191]. However, current approaches require lithographic patterning to realize functional structures, inevitably leaving organic contaminants whose impact is exacerbated by the difficulty in cleaning these atomically-thin materials. The result is a clear need for high-quality, patterned 2D materials with pristine surfaces.

Here, we introduce a novel synthetic approach to templated MoS_2 growth with sub-micron features without the need for resists or other sources of contamination. Stencils made of SiN membranes [192] with feature sizes down to 100 nm are used as masks through which Mo films are deposited onto atomically stepped sapphire substrates [132, 133]. These pre-patterned Mo films are subsequently sulfurized in a reducing atmosphere to grow MoS_2 films [138-141, 143]. Combining the SiN stencil with the sulfurization

growth technique allows centimeter-scale uniform growth and direct control of the number of layers in the resulting MoS_2 film which have an optical quality similar to that of exfoliated and suspended MoS_2 [94, 193] and the highest quality synthesized MoS_2 grown by other methodologies [132, 133]. This growth technique can readily be expanded to a wide variety of other TMDs simply by changing the templated metallic film and has the potential to directly address the demand for patterned 2D materials with pristine surfaces suitable for subsequent modification via functionalization and mechanical stacking.

Over the past five years, many methodologies for MoS_2 growth have been developed [10, 120, 123, 130-133, 136, 137, 194]. In particular, chemical vapor deposition (CVD) techniques whereby MoO_3 and S precursors are evaporated upstream of a heated growth substrate produce high-quality monolayer MoS_2 islands 10-100 μm in width that can form locally continuous films [130-133, 194]. Recently, this CVD technique has been augmented through the use of atomically stepped c-axis sapphire as a growth substrate [132, 133], promoting MoS_2 flake growth with uniform lattice orientation and reducing the number of domains present in these coalesced crystalline films. An alternate route to MoS_2 growth, and the method employed here, is through the sulfurization of pre-deposited Mo films [138, 139]. This technique produces uniform large-area MoS_2 films whose thickness is tuned by controlling the thickness of the starting Mo film [140, 141, 143]. While this sulfurization method is both facile and inexpensive, in the past it has typically yielded polycrystalline and multi-layer films [138-141, 143].

In several cases, both the CVD and sulfurization growth methods have been augmented to nucleate MoS_2 crystallization in predetermined locations by seeding [127] or

patterning [128, 147] the initial substrate, and by templating the pre-deposited Mo film prior to sulfurization [141, 146]. However, these techniques either rely on potentially contaminating lithographic processes or produce erratically shaped and positioned material. The growth technique adopted here builds on these existing approaches through the use of SiN stencils to produce resist free, templated Mo films that are subsequently sulfurized, producing high-quality MoS_2 with large-area uniformity, sub-micron feature sizes, and precisely controlled shape and location.

4.2 Growth Procedure

This growth procedure is illustrated schematically in **Figure 4.1**(a). The stencil is fabricated using focused ion beam (FIB) milling to pattern a SiN membrane, and sapphire substrates are pre-annealed for one hour at 1000 °C in air. This pre-treatment creates atomically smooth steps [195] (**Figure 4.2**(b)) and facilitates single-crystal domain growth of high-quality MoS_2 [131, 132]. Next, the SiN stencil is placed membrane-down on the sapphire substrate and the Mo thin film is deposited through the stencil using electron beam evaporation. These Mo/sapphire samples are then loaded onto an alumina plate and placed in a custom two-zone furnace (**Figure 4.1**(b)) for sulfurization. The furnace is designed such that the temperature of the Mo-templated sample and sulfur powder precursor can be individually controlled, allowing the sulfur temperature and flow during the sulfurization process to be systematically controlled, independent from the sample temperature.

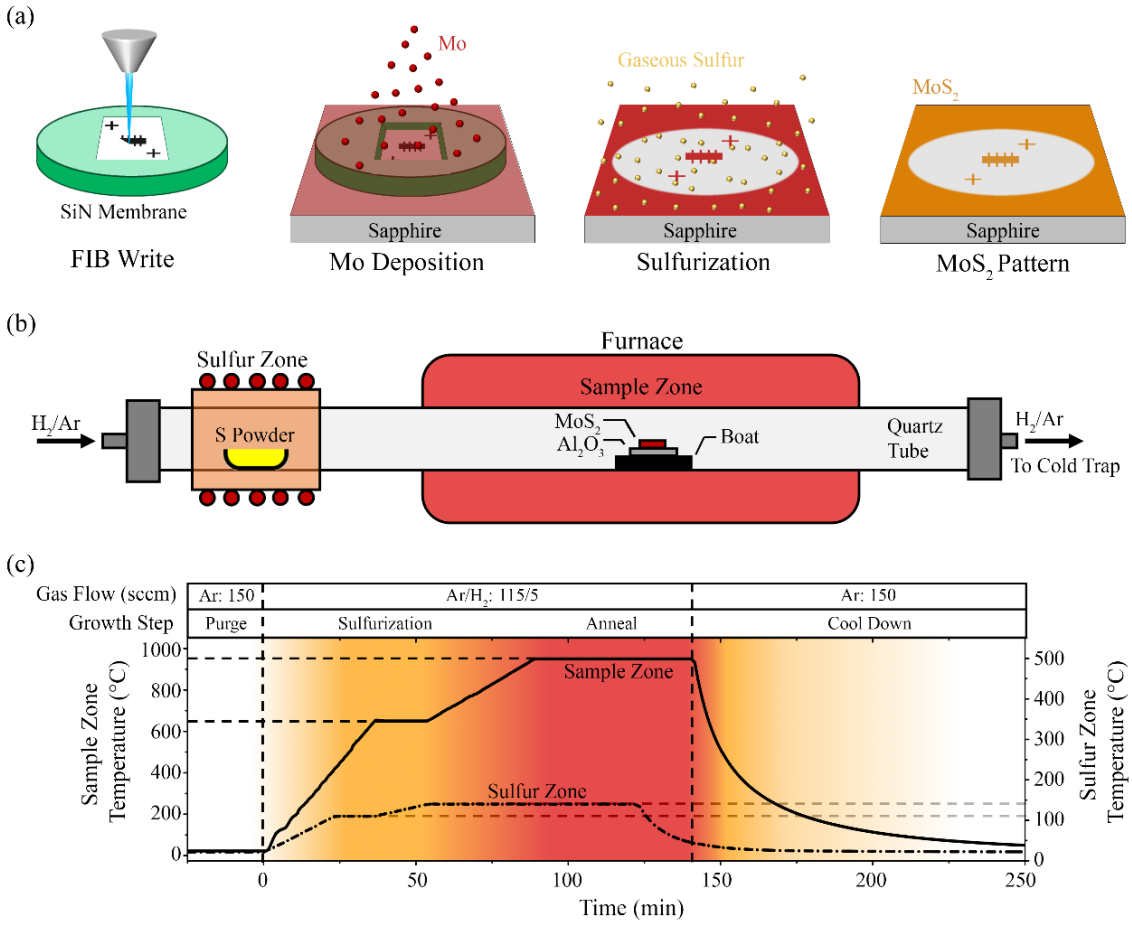

Figure 4.1 *Templated MoS_2 Synthesis.*

(a) SiN membranes (200 nm thick) are patterned using the focused ion beam (FIB) to produce a stencil through which a Mo film is deposited on sapphire via electron beam evaporation. The Mo is subsequently sulfurized in a furnace, resulting in MoS_2. (b) Schematic of custom two-zone furnace where MoS_2 films are sulfurized. The sulfur zone is dedicated to sulfur evaporation and is made of a Cu sleeve wrapped in heating cable. The sample zone controls the temperature of the templated growth substrate. (c) Visualization of growth recipe. The temperature in the two zones as well as the gas flow through the system as a function of growth time. The quartz tube is maintained at a pressure of 3-5 Torr during growth.

The optimized growth recipe, including the temperatures of the sulfur boat and substrate, is shown in **Figure 4.1**(c). The chamber is initially purged for 10 minutes using 150 sccm of Ar. After purging, the gas flow is changed to 115 sccm of Ar, and 5 sccm of H_2 [194, 196], and the sample temperature is ramped to 650 °C at a rate of 20 °C/min for sulfurization. During this initial ramp, the sulfur zone is also ramped up to a pre-melting

temperature of 110 °C. The sample is held at 650 °C for 30 minutes while the sulfur zone temperature is raised to a temperature of 140 °C, beginning the sulfurization process. Subsequently, the sample temperature is increased to 950 °C at a rate of 10 °C/min for a second annealing step while maintaining the sulfur flux. This annealing step is found to increase the quality of the resulting MoS_2 films both in our own work and in the literature [140, 197]. After it is complete, the sulfur zone temperature is reduced until the sulfur resolidifies (typically at a sulfur zone temperature of 50 °C) while maintaining the sample zone temperature at 950 °C to reduce the amount of free sulfur residue present on the substrate. Any residual sulfur is removed post-growth by soaking the sample in acetone for two minutes, rinsing in isopropanol, and finally drying with flowing nitrogen gas (**Figure 4.2**(b)).

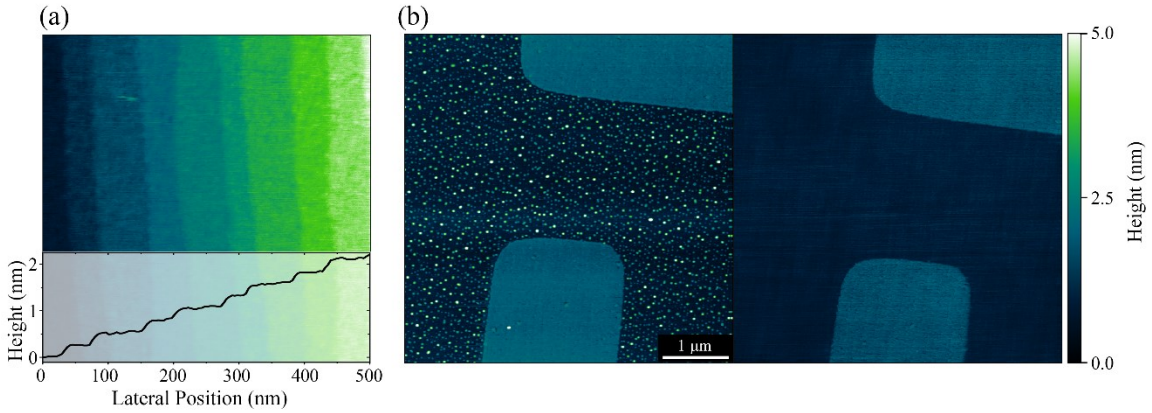

Figure 4.2 *Substrate Preparation and Cleaning.*

(a) AFM scan (top) of the sapphire substrates after annealing at 1000 °C for 1 hour in air showing the atomic steps and a line scan (bottom) across the width of the AFM image showing the expected 0.2nm spacing between steps. (b) AFM images showing a single-layer MoS_2 growth before (left) and after (right) a cleaning procedure which removes the sulfur dots shown in the before image. The cleaning procedure used was a rinsing in acetone for 2 minutes, followed by a 1 minute isopropanol rinse and blowing dry with Nitrogen.

4.3 Experimental Methods

Detailed synthesis parameters for the SiN Stencil fabrication and Mo deposition are provided in **Appendix B**.

4.3.1 SiN Stencil Synthesis.

SiN stencils are synthesized from SiN membranes using FIB milling. Prior to FIB writing, masks are coated with a 50 nm thick Ag film to reduce charging effects and to dissipate heat during the FIB writing process.

4.3.2 Mo Deposition.

Mo is deposited by electron beam evaporation on epi-ready, c-axis, sapphire substrates using deposition rates of 0.1 Å/sec. Substrates are pre-annealed before Mo deposition for one hour at 1000 °C in air.

4.3.3 Sulfurization.

Sulfurization is performed in a 2" diameter quartz tube in a modified Carbolite tube furnace, using Eurotherm temperature controllers and n-type thermocouples for temperature control. The additional sulfur zone is constructed of a ¼ inch Cu sleeve wrapped in heating cable with temperature measured by a k-type thermocouple. Sulfur powder is purchased from Sigma-Aldrich at a purity of 99.98% (#414980-250G). Typically 50 mg of S is used during the sulfurization process. Sulfur powder and Mo coated Sapphire

substrates are both loaded on alumina sample holders. The tube pressure is maintained at a pressure of 3-5 Torr during all growth steps.

4.3.4 Physical Characterization.

Physical characterization was performed via scanning electron microscopy (SEM) and atomic force microscopy (AFM). SEM was performed on a FEI Helios Nanolab 600 dual beam focused ion beam and scanning electron microscope using a voltage of 10 kV and current of 21 pA. Samples were characterized on a Bruker AXS dimension icon atomic/magnetic force microscope using Bruker TESPA-V2 Si probes in tapping mode.

4.3.5 Optical Characterization.

Resulting MoS_2 samples were also characterized optically using Raman scattering spectra and photoluminescence (PL). Both were performed on a Renishaw InVia Raman equipped with a CCD detector at room temperature in ambient atmosphere. Raman was collected using a 514 nm laser for excitation, while a 633 nm laser was used for PL excitation.

4.4 Results and Discussion

4.4.1 Physical Characterization

Characterization begins with the stencils, which are evaluated primarily through *in situ* scanning electron microscopy (SEM) and focused ion beam (FIB) imaging (**Figure 4.3**(a)). Pattern size is limited by the lateral dimensions of the SiN membrane ($750 \times 750\ \mu m^2$), with feature sizes that range from 100 nm to tens of microns (**Figure 4.3**(a)). Molybdenum

film thicknesses in the range of 1-10 nm (100-1000 sec) are calibrated using atomic force microscopy (AFM), and this calibration is subsequently used to estimate the Mo thickness for shorter deposition times (50-100 sec). These pre-sulfurized films are not easily visible optically or via SEM (due to low contrast and extreme charging effects, respectively). **Figure 4.3**(b) shows the full templated write-field after a 50 second Mo deposition and subsequent sulfurization using the recipe shown in **Figure 4.1**(c), demonstrating the fidelity of the templating procedure. Write fields spaced across the entire SiN membrane surface produce uniform MoS_2, regardless of position on the 5×5 mm^2 sapphire substrates. Further, the MoS_2 film quality does not vary sample to sample across the 1×3 in^2 alumina sample holders. In contrast to the bare Mo films, sulfurized films are visible with optical microscopy (**Figure 4.4**). When the deposited metal thickness is properly tuned, this templated sulfurization produces single-layer MoS_2 over the entire templated surface. For example, the AFM image in **Figure 4.3**(c) shows a zoomed in image of the "E" feature of the "CEM" shown in the SEM micrograph in **Figure 4.3**(b), with the line cut inset showing a uniform thickness of 0.7 nm indicating a single atomic layer of MoS_2.

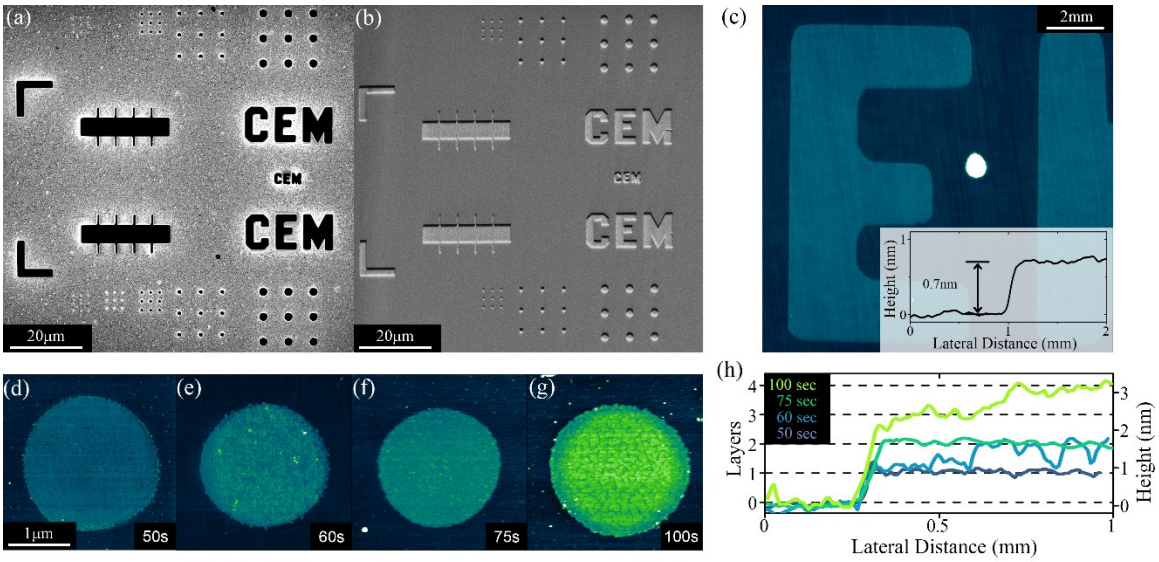

Figure 4.3 *Physical Characterization of MoS_2 Films.*

(a) FIB image of a complete SiN mask. Dark areas are patterned holes in the SiN. (b) SEM image of a completed MoS_2 growth. Lighter areas are single layer MoS_2 (c) AFM image of the "E" corresponding to a single-layer MoS_2 growth. Visible vertical striations are the atomic plateaus present on the sapphire substrate. The inset shows an AFM line scan of the "E" edge with a step height of 0.7nm, corresponding to a single-layer film. (d)-(g) AFM images of 2 μm wide MoS_2 dots on sapphire where the initial Mo film deposition times were varied from 50 seconds (d) to 100 seconds (g). (h) AFM line cuts across the edges of the dots shown in (d)-(g).

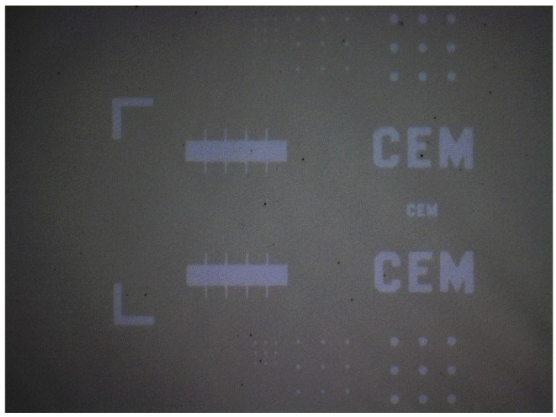

Figure 4.4 *Optical Micrograph of MoS_2 Growth.*

Optical microscopy after the templated growth of single-layer MoS_2 on a sapphire substrate. The field of view has a width of 120 μm.

Figure 4.3(d)-(g) show further AFM micrographs demonstrating the utility of this growth technique in producing templated features with precise control of layer thickness. These micrographs of 2 μm diameter dots show the transition from single-layer to multi-layer MoS_2 films as the Mo metal deposition time is increased from 50 to 100 seconds while all other growth parameters are held constant. The 50 second growth (**Figure 4.3**(d)) results in a single-layer of MoS_2. For Mo depositions of 60 seconds, we observe the seeding of a second layer of growth in the form of bilayer islands on top of the single layer (**Figure 4.3**(e)), and when the deposition time is increased further to 75 seconds these bilayer islands merge to form a continuous second layer of MoS_2 (**Figure 4.3**(d)). Finally, extending the deposition time to 100 seconds results in three layers of MoS_2 with small islands of a fourth layer grown on top. These results are summarized in **Figure 4.3**(h), which shows an AFM line cut for each dot demonstrating the layer-by-layer thickness control down to a single monolayer of MoS_2.

4.4.2 Optical Characterization

Further structural and electronic characterization of these thin films is performed using Raman and photoluminescence (PL) spectroscopies. Raman spectra are collected using a 514 nm (2.41 eV) laser for excitation and a representative spectrum is shown in **Figure 4.5**. We observe both the in-plane vibrational mode of the Mo and S atoms at 384.9 cm^{-1} (E′) with a width of 3.5 cm^{-1} and the out-of-plane vibration of S atoms at 405.1 cm^{-1} (A'_1 peak) with a width of 5.5 cm^{-1}. The E′ and A'_1 peak locations are characteristic of single-layer MoS_2 grown on sapphire [117, 132], and the sharpness of these peaks is an indicator of

high structural order [198]. Additionally, the A'_1 and E' peaks exhibit an intensity ratio close to one (1.02) indicating a slight n-type doping [199]. The small shoulder of the E'_1 peak at 381 cm^{-1} and the extra peak at 416 cm^{-1} are both attributed to the sapphire substrate (**Figure 4.6**).

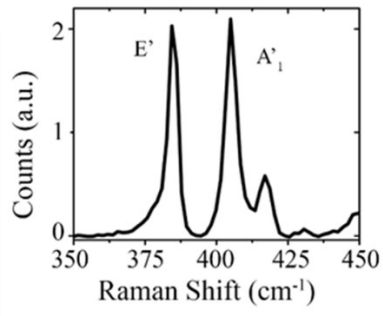

Figure 4.5 *Raman of MoS_2.*

Raman spectra from single-layer MoS_2 film. The characteristic MoS_2 E' and A'_1 Raman peaks are located at 384.9 and 405.1 cm^{-1}, respectively. Peaks at 381 and 416 cm^{-1} originate from the sapphire substrate.

The Raman spectra for samples of varying thickness (the same samples as those shown in **Figure 4.3**(d)-(e)) are measured in order to verify growth thickness (**Figure 4.7)**. We see the characteristic E' peak shift downward by 1.2 cm^{-1} and the A'_1 peak shift upward by 3.7 cm^{-1} as the number of MoS_2 layers is increased from a single-layer sheet, to a bulk film (>10 layers), consistent with the literature [117].

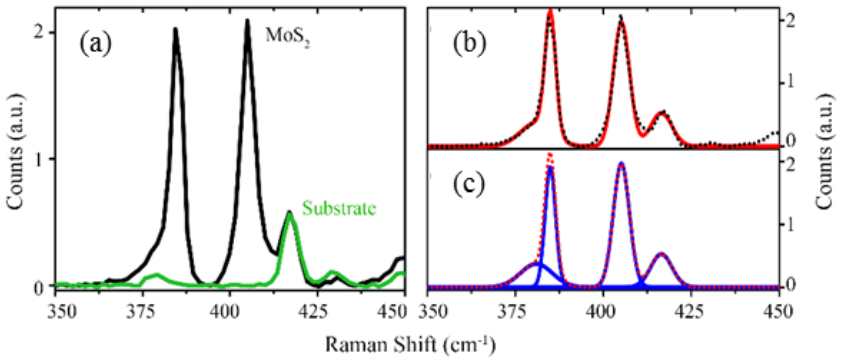

Figure 4.6 *Raman Data Fitting*

(a) Raman spectra for both single-layer MoS2 (black), and the bare sapphire substrate (green). (b) and (c) show the peak fitting used for the Raman spectra. The black curve shows the original single-layer MoS2 signal, the red curve shows the cumulative peak fit, and the blue curves are the individual peak fits. We show the fitting for both the E' (384.9 cm-1) and A'1 (405.1 cm-1) MoS2 peaks as well as the two sapphire substrate peaks.

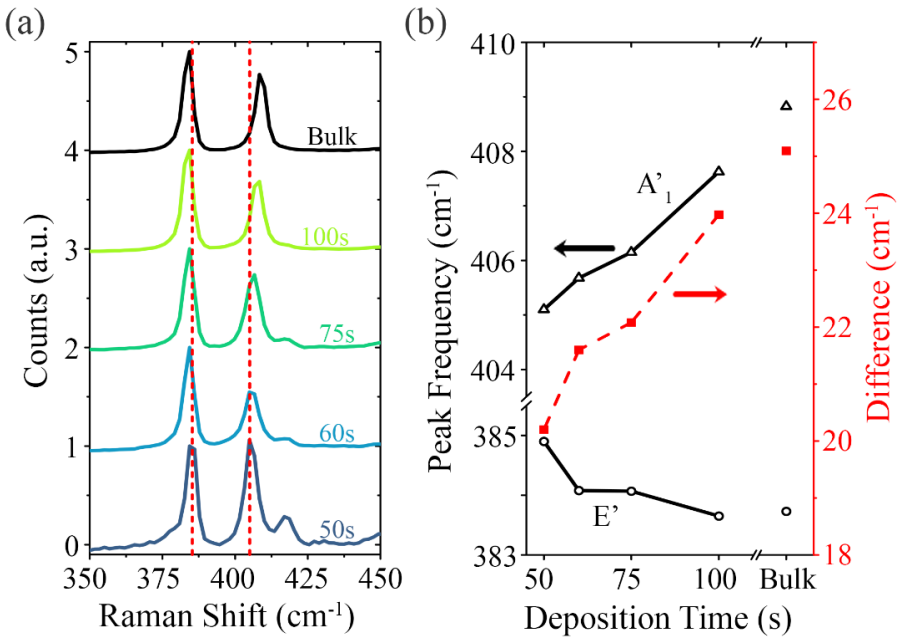

Figure 4.7 *Thickness Dependent Raman*.

(a) Raman spectra of MoS_2 grown with different Mo deposition times. Dashed red lines are centered on the E′ and A'_1 peaks of single-layer MoS_2. (b) Evolution of the characteristic MoS_2 peak positions and peak differences as a function of the initial Mo deposition time.

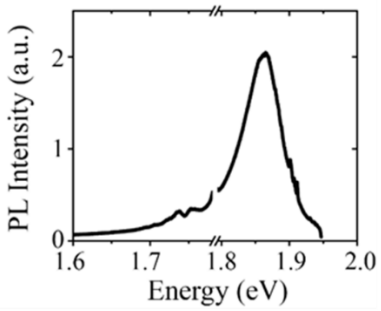

Figure 4.8 *Photoluminescence of MoS_2.*

Photoluminescence (PL) of single-layer MoS_2. The MoS_2 peak energy is centered at 1.86 eV with a FWHM of 56 meV (20 nm). The luminescence dublet from the sapphire substrate around 1.8 eV was removed.

A typical photoluminescence (PL) spectrum is shown in **Figure 4.8** and is measured using a 633 nm (1.96 eV) laser for excitation. We observe an intense A excitonic peak at 1.86 eV with a peak width of 56 meV (20 nm) which is comparable to that of suspended exfoliated MoS_2 flakes as well as the highest quality CVD grown MoS_2, and is indicative of highly crystalline single-layer MoS_2 [94, 132, 133] (for details regarding background spectra and peak fitting see **Figure 4.9**).

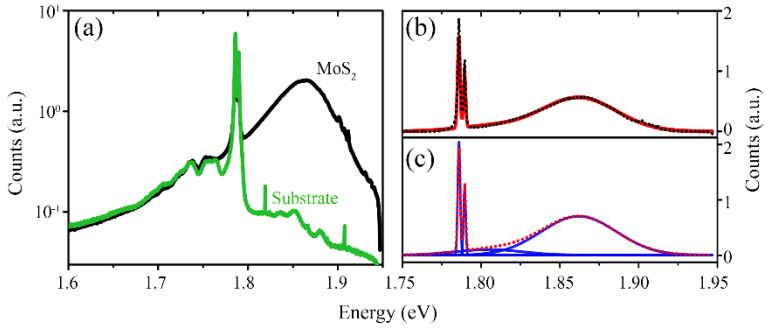

Figure 4.9 *PL Data Fitting.*

Photoluminescence (PL) spectra plotted on a logarithmic scale for both single-layer MoS2 (black), and the bare sapphire substrate (green). (b) and (c) show the peak fitting used for the (PL) spectra. The black curve shows the original single-layer MoS2 signal, the red curve shows the cumulative peak fit, and the blue curves are the individual peak fits.

In addition to individual PL and Raman spectra, we have performed optical mapping of the "CEM" portion of the pattern using half micron steps with a spot size of 0.4-0.6 μm. **Figure 4.10** shows the optical mapping of the 1.86 eV PL peak intensity (top), E′ Raman peak intensity (middle), and A'_1 Raman peak intensity (bottom). These maps demonstrate that the single-layer films are both optically and structurally uniform. This uniformity extends over the entire 5 × 5 mm^2 substrate.

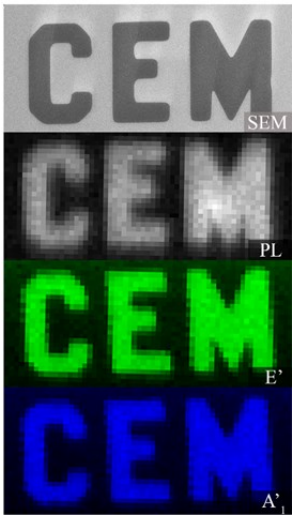

Figure 4.10 *Optical Mapping.*

Intensity maps showing a SEM micrograph for reference, the PL intensity at 1.86 eV, and Raman intensity at 385 cm^{-1} (E′) and 405 cm^{-1} (A'_1).

4.5 Conclusion

In conclusion, we have developed a high-quality MoS_2 growth technique wherein Mo is deposited onto atomically-stepped sapphire substrates through a SiN stencil with feature sizes down to 100 nm and subsequently sulfurized at high temperature. These films have a quality comparable to the best MoS_2 prepared by other methodologies, and the thickness

of the resulting MoS_2 patterns can be tuned layer-by-layer by controlling the initial Mo deposition. Raman and PL spectra are found to be of similar high quality to that of suspended exfoliated MoS_2 and high-quality MoS_2 grown by CVD methods [94, 132, 133]. This stenciled sulfurization methodology presents a facile and inexpensive route to pre-patterned MoS_2 monolayer films that are completely free of the organic residues generated by lithographic patterning techniques. The combination of high materials quality and pristine surfaces demonstrates the potential of this growth technique for use surface functionalization studies and the assembly of Van der Waals heterostructures that comprise some of the most active frontiers in 2D materials [170, 171, 190, 191].

4.6 Future Directions

This templated MoS_2 growth technique combines the power of several existing growth techniques and these initial results demonstrate a high-quality crystal. There are several future directions and additional measurements that we feel would help this technique mature. First, one of the issues we've experienced is the difficulty in depositing the exact amount of Mo metal necessary for a completely continuous growth of MoS_2, as well as consistency with this deposition process. At times, too much Mo is deposited and small bilayer islands are produced, or the resulting MoS_2 films contain nano-voids. An example AFM and SEM image of the latter is shown in **Figure 4.11**(a). We believe this is occurring due to a combination of two reasons.

The first, is the variability of the Mo deposition itself. To achieve the thin films used, slow depositions (0.1 Å/sec) are used, which are near the limit of the electron beam

evaporation system used (particularly of the quartz crystal monitors). Additionally, Mo metal has a very high melting temperature (2 623 °C) which causes the current deposition chamber temperature to increase. This creates considerable variability in the crystal monitor used to record the deposition rate. We hope to combat this in the future by either switching to a molecular beam epitaxy (MBE) growth system or switching to a sputtered deposition of the Mo film. See **Appendix B** for more details on these two issues.

The second possible cause for observed instability in the coverage of MoS_2 film, is the growth itself. By manipulating the parameters of the MoS_2 sulfurization, we can change the growth morphology of the film. In particular, it appears that the timing of the sulfur exposure has a large effect on the mobility of MoS_2, or the metal precursor. An example of this variation, and the effects of manipulating the growth parameters is shown in **Figure 4.11**(b) and (c). In this new growth recipe (**Figure 4.11**(c), red data), the sulfur is left at room temperature until after the sample temperature has reached the first soak period (in this case at 675 °C). This reduces the amount of sulfur sublimation occurring during the first ramp and soak of the sample temperature.

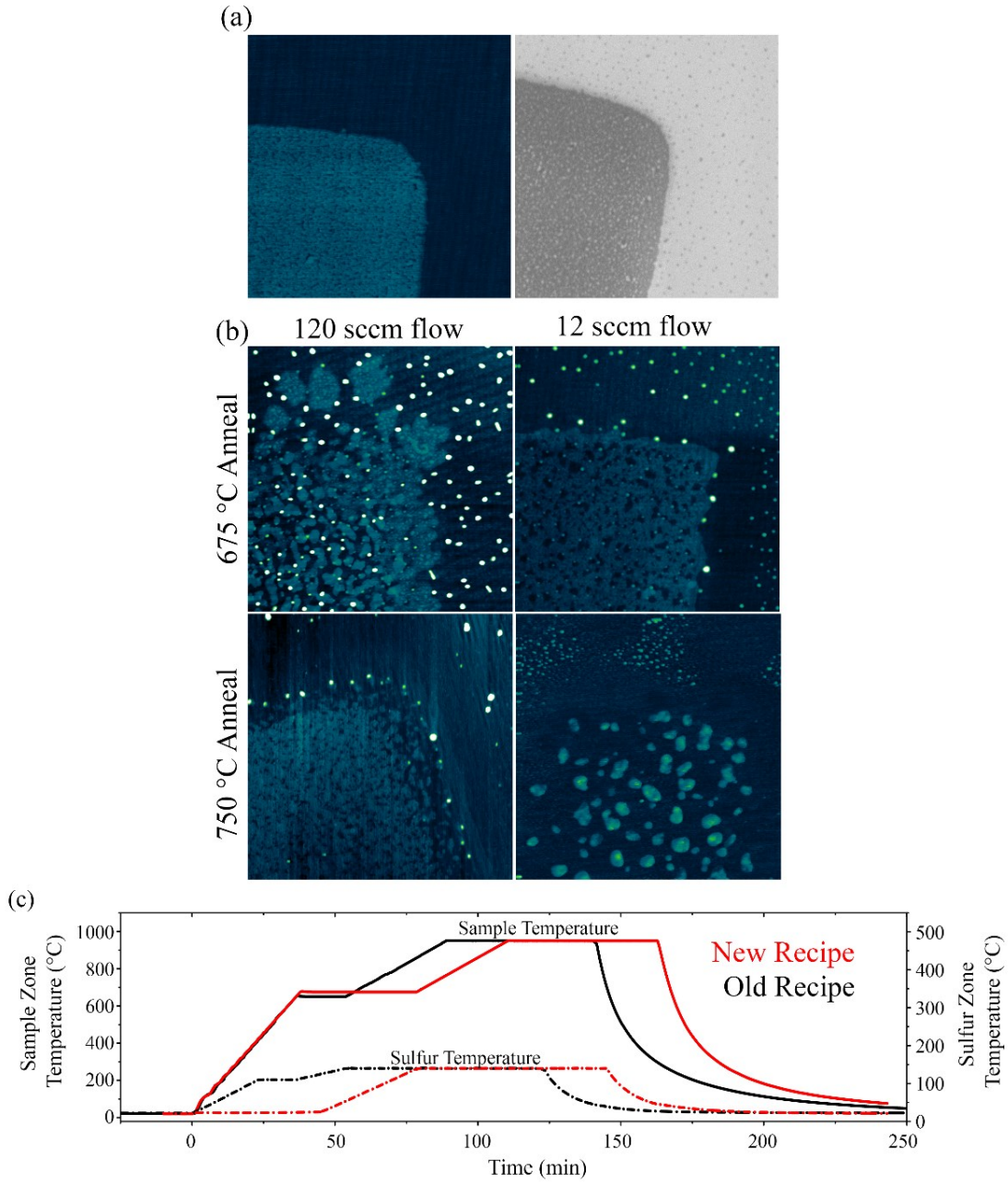

Figure 4.11 *Future Directions*.

(a) Showing a zoomed in view of the "E" from CEM pattern shown in **Figure 4.3** (field width of 2 μm) (c), showing the presence of nano-voids in the film. AFM image on left, SEM on right. (b) AFM images showing the growth morphology of an altered growth procedure at different annealing temperatures and total gas flows. (c) Comparison of the growth used in the main text of this chapter, with the new growth recipe described in Section 0. All AFM images have the same scanning field of 2 μm^2.

Using this new protocol, four different sulfurizations were performed (using samples from the same 50 sec Mo film depositions) with two different first stage soak temperatures (675 and 750 °C) and two different total gas flows (and consequently different sulfur flux, 120 and 12 sccm, with H_2:Ar ratio held constant). These four growths recipes exhibit different surface morphologies (from each other, and from the original growth recipe). We speculate this is a result of the sulfur pinning down the MoS_2 growth to greater or lesser degrees depending on the time of S introduction, sulfur flux, and substrate temperature. Much work remains to determine an ideal growth recipe for this templated, sulfurization technique. Again, we emphasize that one of the strengths of this templated growth is the ability to quickly analyze the growth morphology via AFM on easily identifiable features common to each growth.

In addition to the tuning of the existing growth technique, we intend to expand this growth technique to other materials. In particular, we are interested in using this method to attempt the growth of either V doped MoS_2 and VS_2—new materials, both of which we believe may exhibit magnetic properties [200-202]. This could also be extended to other common TMD materials by changing either the predeposited metal (Nb, Ta, or W), or the evaporated chalcogenide (in particular to Se). Demonstrating that this growth method can be used on the existing library of TMD materials would add even more value to this templated-growth methodology.

4.7 Acknowledgements

This research was supported by funding from the Center for Emergent Materials: an NSF MRSEC, Award Number DMR-1420451. Technical support was provided by the NanoSystems Laboratory and NanoTech West at OSU.

4.8 References

10. Novoselov, K.S., *et al.*, *Two-Dimensional Gas of Massless Dirac Fermions in Graphene.* Nature. **438**(7065): p. 197-200. 2005. http://dx.doi.org/10.1038/nature04233

82. Berger, A.J., *et al.*, *Correlating spin transport and electrode magnetization in a graphene spin valve: Simultaneous magnetic microscopy and non-local measurements.* Applied Physics Letters. **107**(14). 2015. http://dx.doi.org/10.1063/1.4932673

83. Novoselov, K.S., *et al.*, *Two-dimensional atomic crystals.* Proceedings of the National Academy of Sciences of the United States of America. **102**(30): p. 10451-10453. 2005. http://dx.doi.org/10.1073/pnas.0502848102

84. Bhimanapati, G.R., *et al.*, *Recent Advances in Two-Dimensional Materials beyond Graphene.* ACS Nano. **9**(12): p. 11509-11539. 2015. http://dx.doi.org/10.1021/acsnano.5b05556

86. Butler, S.Z., *et al.*, *Progress, Challenges, and Opportunities in Two-Dimensional Materials Beyond Graphene.* ACS Nano. **7**(4): p. 2898-2926. 2013. http://dx.doi.org/10.1021/nn400280c

91. Wang, Q.H., *et al.*, *Electronics and optoelectronics of two-dimensional transition metal dichalcogenides.* Nature Nanotechnology. **7**(11): p. 699-712. 2012. http://dx.doi.org/10.1038/nnano.2012.193

94. Mak, K.F., *et al.*, *Atomically thin MoS2: a new direct-gap semiconductor.* Physical Review Letters. **105**(13): p. 136805. 2010. http://dx.doi.org/10.1103/PhysRevLett.105.136805

95. Splendiani, A., *et al.*, *Emerging photoluminescence in monolayer MoS2.* Nano Letters. **10**(4): p. 1271-1275. 2010. http://dx.doi.org/10.1021/nl903868w

96. Lee, G.-h., *et al.*, *Highly Stable , Dual-Gated MoS2 Transistors Encapsulated by Hexagonal Boron Nitride with Gate-Controllable Contact, Resistane and Threshold Voltage.* ACS Nano. **9**: p. 7019-7019. 2015. http://dx.doi.org/10.1021/acsnano.5b01341

97. Choi, W., *et al.*, *High-detectivity multilayer MoS2 phototransistors with spectral response from ultraviolet to infrared.* Advanced Materials. **24**(43): p. 5832-5836. 2012. http://dx.doi.org/10.1002/adma.201201909

98. Bertolazzi, S., D. Krasnozhon, and A. Kis, *Nonvolatile memory cells based on MoS2/graphene heterostructures.* ACS Nano. **7**(4): p. 3246-3252. 2013. http://dx.doi.org/10.1021/nn3059136

99. Bao, W., *et al.*, *High mobility ambipolar MoS2 field-effect transistors: Substrate and dielectric effects.* Applied Physics Letters. **102**(4). 2013. http://dx.doi.org/10.1063/1.4789365

100. Bertolazzi, S., J. Brivio, and A. Kis, *Stretching and breaking of ultrathin MoS2.* ACS Nano. **5**(12): p. 9703-9709. 2011. http://dx.doi.org/10.1021/nn203879f

101. Heiranian, M., A.B. Farimani, and N.R. Aluru, *Water desalination with a single-layer MoS2 nanopore.* Nature Communications. **6**: p. 1-6. 2015. http://dx.doi.org/10.1038/ncomms9616

103. Akinwande, D., N. Petrone, and J. Hone, *Two-dimensional flexible nanoelectronics.* Nature Communications. **5**: p. 5678-5678. 2014. http://dx.doi.org/10.1038/ncomms6678

104. Kam, K.K. and B.A. Parkinson, *Detailed Photocurrent Spectroscopy.* Journal of Physical Chemistry. **86**: p. 463-467. 1982. http://dx.doi.org/10.1021/j100393a010

105. Smith, R.J.*, et al.*, *Large-scale exfoliation of inorganic layered compounds in aqueous surfactant solutions.* Advanced Materials. **23**(34): p. 3944-3948. 2011. http://dx.doi.org/10.1002/adma.201102584

107. Lebègue, S. and O. Eriksson, *Electronic structure of two-dimensional crystals from ab initio theory.* Physical Review B. **79**(11): p. 4-7. 2009. http://dx.doi.org/10.1103/PhysRevB.79.115409

108. Kuc, A., N. Zibouche, and T. Heine, *Influence of quantum confinement on the electronic structure of the transition metal sulfide TS2.* Physical Review B. **83**(24): p. 245213-245213. 2011. http://dx.doi.org/10.1103/PhysRevB.83.245213

110. Radisavljevic, B.*, et al.*, *Single-layer MoS2 transistors.* Nature Nanotechnology. **6**(3): p. 147-150. 2011. http://dx.doi.org/10.1038/nnano.2010.279

112. Kim, K.K.*, et al.*, *Synthesis of monolayer hexagonal boron nitride on Cu foil using chemical vapor deposition.* Nano Letters. **12**(1): p. 161-166. 2012. http://dx.doi.org/10.1021/nl203249a

113. Mak, K.F.*, et al.*, *The valley Hall effect in MoS_2 transistors.* Science. **344**(6191): p. 1489-92. 2014. http://dx.doi.org/10.1126/science.1250140

114. Mak, K.F.*, et al.*, *Control of valley polarization in monolayer MoS2 by optical helicity.* Nature Nanotechnology. **7**(8): p. 494-498. 2012. http://dx.doi.org/10.1038/nnano.2012.96

117. Lee, C.*, et al.*, *Anomalous lattice vibrations of single-and few-layer MoS2.* ACS Nano. **4**(5): p. 2695-700. 2010. http://dx.doi.org/10.1021/nn1003937

120. Stewart, T.B. and P.D. Fleischauer, *Chemistry of sputtered molybdenum disulfide films.* Inorganic Chemistry. **21**(6): p. 2426-2431. 1982. http://dx.doi.org/10.1021/ic00136a060

123. Wu, S.*, et al.*, *Vapor-Solid Growth of High Optical Quality MoS2 Monolayers with Near-Unity Valley Polarization.* ACS Nano. **7**(3): p. 2768-2772. 2013. http://dx.doi.org/10.1021/nn4002038

127. Lee, Y.H.*, et al.*, *Synthesis of large-area MoS2 atomic layers with chemical vapor deposition.* Advanced Materials. **24**(17): p. 2320-2325. 2012. http://dx.doi.org/10.1002/adma.201104798

128. Najmaei, S.*, et al.*, *Vapour phase growth and grain boundary structure of molybdenum disulphide atomic layers.* Nature Materials. **12**(8): p. 754-9. 2013. http://dx.doi.org/10.1038/nmat3673

130. van der Zande, A.M.*, et al.*, *Grains and grain boundaries in highly crystalline monolayer molybdenum disulphide.* Nature Materials. **12**(6): p. 554-61. 2013. http://dx.doi.org/10.1038/nmat3633

131. Dumcenco, D.*, et al.*, *Large-area MoS2 grown using H2S as the sulphur source.* 2D Materials. **2**(4): p. 044005-044005. 2015. http://dx.doi.org/10.1088/2053-1583/2/4/044005

132. Dumcenco, D.*, et al.*, *Large-Area Epitaxial Monolayer MoS2.* ACS Nano. **10**(1021). 2015. http://dx.doi.org/10.1021/acsnano.5b01281

133. Baek, S.H., Y. Choi, and W. Choi, *Large-Area Growth of Uniform Single-Layer MoS2 Thin Films by Chemical Vapor Deposition.* Nanoscale Research Letters. **10**(1): p. 388-388. 2015. http://dx.doi.org/10.1186/s11671-015-1094-x

136. Kang, K.*, et al.*, *High-mobility three-atom-thick semiconducting films with wafer-scale homogeneity.* Nature. **520**(7549): p. 656-660. 2015. http://dx.doi.org/10.1038/nature14417

137. Jang, Y.*, et al.*, *Wafer-scale, conformal and direct growth of MoS2 thin filmsby atomic layer deposition.* Applied Surface Science. **365**: p. 160-165. 2016. http://dx.doi.org/10.1016/j.apsusc.2016.01.038

138. Zhan, Y.*, et al.*, *Large-area vapor-phase growth and characterization of MoS2 atomic layers on a SiO2 substrate.* Small. **8**(7): p. 966-971. 2012. http://dx.doi.org/10.1002/smll.201102654

139. Laskar, M.R.*, et al.*, *Large Area Single Crystal (0001) Oriented MoS2 Thin Films.* Applied Physics Letters. **102**: p. 252108-252108. 2013. http://dx.doi.org/10.1063/1.4811410

140. Lee, Y.*, et al.*, *Synthesis of wafer-scale uniform molybdenum disulfide films with control over the layer number using a gas phase sulfur precursor.* Nanoscale. **6**(5): p. 2821-6. 2014. http://dx.doi.org/10.1039/c3nr05993f

141. Gatensby, R.*, et al.*, *Controlled synthesis of transition metal dichalcogenide thin films for electronic applications.* Applied Surface Science. **297**: p. 139-146. 2014. http://dx.doi.org/10.1016/j.apsusc.2014.01.103

143. Liu, H.*, et al.*, *Towards large area and continuous MoS2 atomic layers via vapor-phase growth: thermal vapor sulfurization.* Nanotechnology. **25**(40): p. 405702-405702. 2014. http://dx.doi.org/10.1088/0957-4484/25/40/405702

146. Han, G.H.*, et al.*, *Seeded growth of highly crystalline molybdenum disulphide monolayers at controlled locations.* Nature Communications. **6**: p. 6128-6128. 2015. http://dx.doi.org/10.1038/ncomms7128

147. Sun, D.*, et al.*, *Chemical vapor deposition growth of a periodic array of single-layer MoS2 islands via lithographic patterning of an SiO2/Si substrate.* 2D Materials. **2**(4): p. 045014-045014. 2015. http://dx.doi.org/10.1088/2053-1583/2/4/045014

170. Geim, A.K. and I.V. Grigorieva, *Van der Waals heterostructures.* Nature. **499**(7459): p. 419-25. 2013. http://dx.doi.org/10.1038/nature12385

171. Niu, T. and A. Li, *From two-dimensional materials to heterostructures.* Progress in Surface Science. **90**(1): p. 21-45. 2015. http://dx.doi.org/10.1016/j.progsurf.2014.11.001

188. Qian, X.*, et al.*, *Quantum spin Hall effect in two- dimensional transition metal dichalcogenides.* Science express. **10**(November): p. 1126-1126. 2014. http://dx.doi.org/10.1126/science.1256815

189. Wang, F.*, et al.*, *Ionic Liquid Gating of Suspended MoS2 Field Effect Transistor Devices.* Nano Letters. **15**(8): p. 5284-5288. 2015. http://dx.doi.org/10.1021/acs.nanolett.5b01610

190. Presolski, S. and M. Pumera, *Covalent functionalization of MoS2.* Materials Today. **19**(3): p. 140-145. 2016. http://dx.doi.org/10.1016/j.mattod.2015.08.019

191. Sarkar, D., *et al.*, *Functionalization of Transition Metal Dichalcogenides with Metallic Nanoparticles: Implications for Doping and Gas-Sensing.* Nano Letters. **15**(5): p. 2852-2862. 2015. http://dx.doi.org/10.1021/nl504454u

192. Vazquez-Mena, O., *et al.*, *Resistless nanofabrication by stencil lithography: A review.* Microelectronic Engineering. **132**: p. 236-254. 2015. http://dx.doi.org/10.1016/j.mee.2014.08.003

193. Scheuschner, N., *et al.*, *Photoluminescence of freestanding single- and few-layer MoS2.* Physical Review B - Condensed Matter and Materials Physics. **89**(12): p. 2-7. 2014. http://dx.doi.org/10.1103/PhysRevB.89.125406

194. Feng, Y., *et al.*, *Synthesis of Large-Area Highly Crystalline Monolayer Molybdenum Disulfide with Tunable Grain Size in a H2 Atmosphere.* ACS Applied Materials and Interfaces. **7**(40): p. 22587-22593. 2015. http://dx.doi.org/10.1021/acsami.5b07038

195. Yoshimoto, M., *et al.*, *Atomic-scale formation of ultrasmooth surfaces on sapphire substrates for high-quality thin-film fabrication.* Applied Physics Letters. **67**(18): p. 2615-2617. 1995. http://dx.doi.org/10.1063/1.114313

196. Li, X., *et al.*, *Role of hydrogen in chemical vapor deposition growth of MoS2 atomic layers.* Nanoscale. p. 8398-8404. 2015. http://dx.doi.org/10.1039/C5NR00904A

197. Ji, Q., *et al.*, *Epitaxial Monolayer MoS2 with Novel Photoluminescence.* Nano Letters. **13**(8): p. 130730131307000-130730131307000. 2013. http://dx.doi.org/10.1021/nl401938t

198. Islam, M.R., *et al.*, *Tuning the electrical property via defect engineering of single layer MoS2 by oxygen plasma.* Nanoscale. **6**(17): p. 10033-9. 2014. http://dx.doi.org/10.1039/c4nr02142h

199. Chakraborty, B., *et al.*, *Symmetry-dependent phonon renormalization in monolayer MoS2 transistor.* Physical Review B. **85**(16): p. 2-5. 2012. http://dx.doi.org/10.1103/PhysRevB.85.161403

200. Zhang, H., L.-M. Liu, and W.-M. Lau, *Dimension-dependent phase transition and magnetic properties of VS2.* Journal of Materials Chemistry A. **1**(36): p. 10821-10821. 2013. http://dx.doi.org/10.1039/c3ta12098h

201. Zhuang, H.L. and R.G. Hennig, *Stability and magnetism of strongly correlated single-layer VS2.* Physical Review B. **93**(5): p. 054429-054429. 2016. http://dx.doi.org/10.1103/PhysRevB.93.054429

202. Xu, K., *et al.*, *Ultrathin nanosheets of vanadium diselenide: A metallic two-dimensional material with ferromagnetic charge-density-wave behavior.* Angewandte Chemie - International Edition. **52**(40): p. 10477-10481. 2013. http://dx.doi.org/10.1002/anie.201304337

Chapter 5: Toward Scanning Probe and Transmission Microscopy of Local Defects in Active Graphene Electronic Devices

5.1 Introduction

Graphene's isolation in 2004 by Geim and Novoselov [1]—for which they were awarded the Nobel prize in 2010—has led to an explosion of discovery and research both around graphene itself as well as a host of other related two-dimensional materials. This atomically thin material exhibits a host of excellent electronic [2-8], spintronic [29], thermal [27, 28], mechanical [27, 28, 30], and optical properties [33-35]. These properties have earned it considerable attention for potential applications in flexible and transparent electronics, stacked heterostructures, and as a unique platform for exploring new physics [8, 9, 23-26]. In particular, its linear gapless band structure around the K and K′ points results in high carrier mobilities in excess of 100 000 $cm^2V^{-1}s^{-1}$ [12-14]—more than two orders of magnitude greater than Si—and the ability to easily tune the carrier type and density through use of a back-gate.

Despite the many enticing properties exhibited by graphene, the lack of a band gap, correlated electron effects, and spin-orbit coupling dramatically reduces its utility in optoelectronics, spintronics, and other emerging fields. Other than carrier density, which is easily manipulated, these other appealing properties are considerably more difficult to

tune without the destruction of graphene's attractive carrier mobility [7, 74-76]. One of the few successful methods of manipulating graphene's electronic properties has been through the chemical modification of graphene [77]. In particular the hydrogenation and fluorination of graphene (graphane and flourographene respectively) [78, 79] as well as graphene doping via deposition of transition metal adatoms [80] have been investigated. However, in these and other cases, these chemical modifications are done on a substrate wide scale, where it is difficult to correlate the atomic level changes to the large area transport properties.

In this chapter, we look at the progress toward investigating how the local graphene environment affects the observable electronic and spin transport. This is accomplished through scanning probe and tunneling microscopy measurements on active electronic graphene devices. First, we look at the development of a customized scanning probe microscope (SPM) which is capable of electrostatic, atomic, and magnetic force microscopies. We also describe the synthesis of highly customizable graphene field effect transistor (FET) devices from chemical vapor deposition (CVD) synthesized graphene for use in this microscope. Second, we investigate additional developments and techniques necessary to use these fabricated graphene FETs in a scanning tunneling microscope (STM) to explore how chemical changes at the atomic scale affect the large-scale transport properties in graphene.

Both of these are on-going projects, and much remains to be done. However, initial proof-of concept results are shown here. The SPM work is performed in collaboration with Andy Berger from the Hammel lab at The Ohio State University (OSU), who designed and

built the customized SPM system, and performed the simultaneous scanning and electrical measurements on the graphene FET devices. The STM work is conducted in collaboration with Grady Gambrel and Shawna Hollen of the Jay Gupta lab at OSU, with Grady performing the STM imaging and *in situ* device measurements. I performed Graphene device development and synthesis for both of these projects.

5.2 SPM Study of Charge and in Graphene[1]

5.2.1 Custom SPM System

Understanding the complex properties of electronic and spintronic devices at the micro- and nanoscale is a topic of intense interest as it becomes increasingly important for scientific progress and technological applications. *In-operando* characterization of such devices by scanned probe techniques is particularly well-suited for the microscopic study of these properties. We have developed a scanned probe microscope (SPM) capable of both standard force imaging (atomic, magnetic, and electrostatic) and simultaneous electrical transport measurements. This system utilizes flexible and inexpensive FPGA (field programmable gate array) hardware and a custom software framework developed in National Instrument's LabVIEW to perform the various aspects of microscope operation and device measurement. Using this system, we demonstrate electrostatic force microscopy of an electrically-biased graphene FET device. The combination of SPM and electrical

[1] This work is described fully in the publication *Review of Scientific Instruments* **85,** 123702 (2014) [81]

transport also enables imaging of the transport response to a localized perturbation provided by the scanned cantilever tip.

The SPM system was used for all data collected in Section 5.2 and is shown in various levels of detail in **Figure 5.1**. For a full description of the instrumentation and theory of operation of this microscope, see Ref. [81].

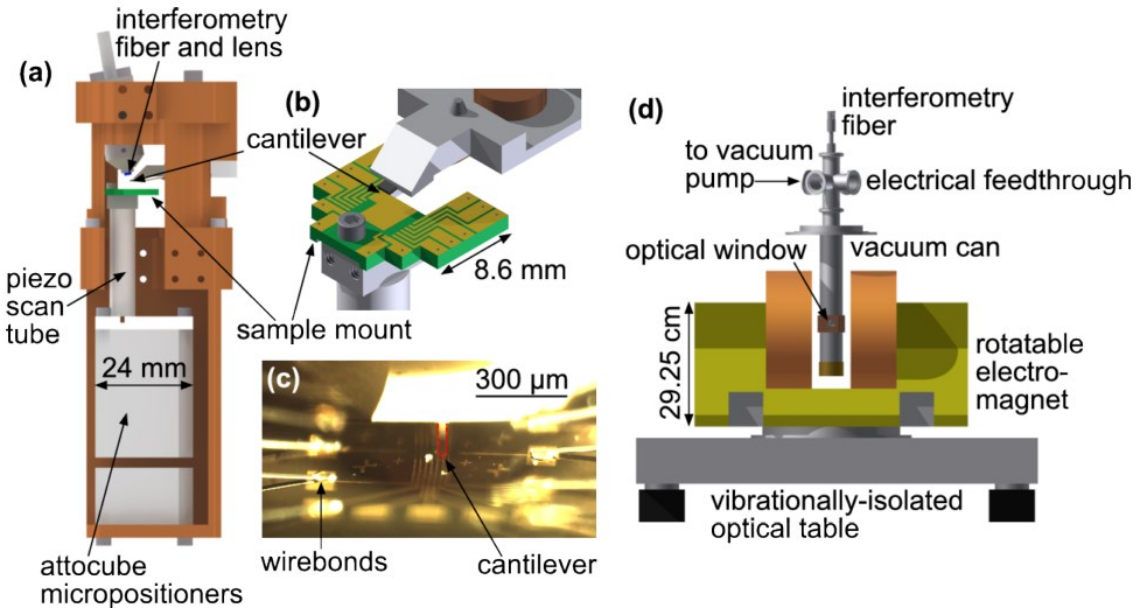

Figure 5.1 *Scanning Probe Microscope Setup.*

(a) Microscope scan head. (b) Schematic diagram of cantilever and electrical sample holder. (c) Optical view through window of sample and cantilever, showing the device (center of the image) and wire bonds (along the edges). The cantilever is outlined in red. (d) Schematic of entire microscope.

5.2.2 Device Fabrication

Much of the initial work on graphene was performed on samples exfoliated from bulk HOPG crystals onto SiO_2 substrates [1]. This produces graphene of excellent crystalline and electronic quality [2, 12]. However, it is not suitable for large devices or mass

production. In an attempt to remedy this shortcoming, a large number of potentially scalable growth methods have been developed [2, 4, 34, 39-52]. Of these, growth via chemical vapor deposition (CVD) on Cu has emerged as one of the most convenient and promising routes toward high-quality, single layer graphene [39, 40, 50]. After growth the graphene is transferred from the Cu growth substrate to one of choice (typically SiO_2/Si) by one of several methods [53-61]. Typically this is done using a poly(methyl methacrylate) (PMMA) assisted transfer method [58, 60, 61].

The graphene FET device is fabricated from CVD grown graphene purchased from Graphene Supermarket. A full description of the device synthesis with all relevant lithographic parameters is provided in **Appendix A.** We provide an abbreviated description here. Samples purchased are 1 cm^2 of graphene on SiO_2(285 nm)/Si(p-type). This graphene is grown via CVD on Cu foils [50], and subsequently transferred to SiO_2 using PMMA for support [60, 61]. These samples are coated with PMMA to protect the graphene films, and then cleaved into 5 × 5 mm samples. This protective PMMA coating is subsequently removed in acetone.

A two-step lithographic process is performed to first define and deposit metallic contacts and then to etch the graphene film into the correct Hall bar shape. In the first step, samples are recoated with a copolymer/PMMA. After electron beam lithography (EBL) and development, a Ti(1 nm)/Au(100 nm) metallic film is deposited using electron beam evaporation. Subsequently, lift-off is done in hot acetone (75 °C, in a water bath) leaving the metallic contacts on top of the graphene sheet. This hot acetone step is critical (see Section 5.3.2) to help remove any organic residue from the resist.

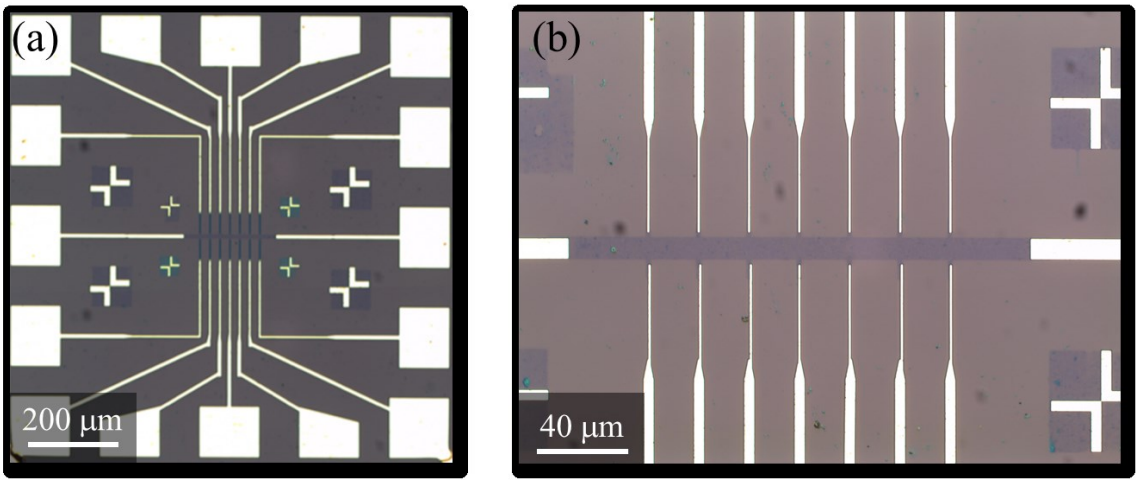

Figure 5.2 *Graphene Hall Bar.*

Optical micrograph of completed graphene Hall bar device. (a) Full device. (b) Zoom in of the central region showing the distinct graphene bar (darker purple) in the center of the device. This graphene bar has a width of 10 μm.

In the second patterning step, a PMMA/HSQ (hydrogen silsesquioxane) resist stack is used. The PMMA under-layer is used as a sacrificial layer to protect the graphene from the exposed HSQ (a negative resist), which would otherwise be permanently affixed to the graphene. The second EBL and development is performed, leaving a Hall bar shaped mask in the HSQ. The exposed PMMA and underlying graphene is etched using reactive ion oxygen plasma etching. Finally, the remaining PMMA/HSQ is removed in a hot acetone soak for 2-5 hours. An optical micrograph of a completed device is shown in in **Figure 5.2**(a).

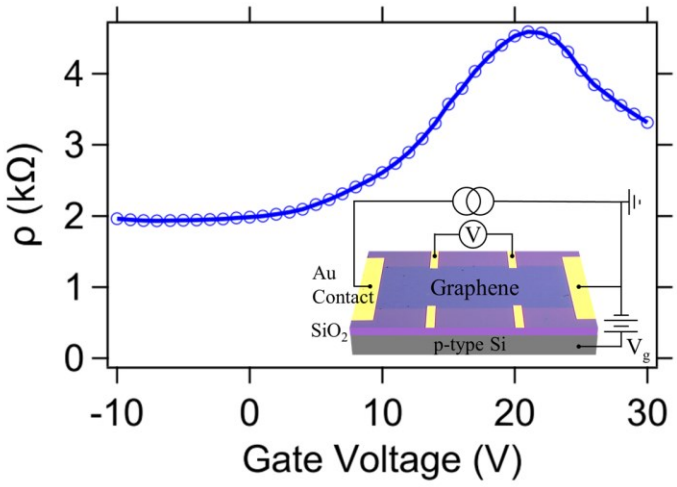

Figure 5.3 *Graphene FET Measurement.*

Four-probe gate-dependence of graphene resistivity acquired in SPM setup, showing the characteristic Dirac peak near V_G = 20 V. Inset: schematic of measurement configuration.

An example of a transport measurement obtained with a device mounted in our microscope is shown in **Figure 5.3**. The device-under-test is a graphene field-effect transistor (FET), patterned in a Hall bar geometry. In this geometry, a gate voltage is applied to the doped Si substrate which shifts the Fermi energy (E_F) of the graphene through the linear band structure. When the E_F passes through the charge neutrality point (known as the Dirac point) of the band structure, the carrier density decreases to nearly zero, causing the resistivity of the device to increase (the Dirac peak). A Dirac peak at zero applied gate voltage would indicate no doping. In this device (and in most devices on SiO_2 substrates), the peak is shifted toward a positive gate voltage, which is an indication of p-type doping in the channel.

5.2.3 Charge Transport in Graphene

Using the custom SPM system developed, we acquired scanned electrostatic force microscopy (EFM) images of an electrically-biased graphene field effect transistor (CVD graphene on SiO_2(285 nm)/p-Si) in order to demonstrate the ability to perform integrated scanning and current-voltage measurements. In an EFM measurement, the cantilever frequency is shifted by the capacitive interaction between tip and sample [203].

$$\delta f = -\frac{1}{2}\left(\frac{d^2C}{dz^2}\right)V^2$$

where C is the capacitance of the tip-sample system, and V is the potential difference between tip and surface.

In **Figure 5.4** we show the measured cantilever frequency shift for two configurations of the graphene Hall cross: electrical current flowing left to right (**Figure 5.4**(a)), or right to left (**Figure 5.4**(b)). The cantilever is sensitive only to voltage differences between itself and the sample. The cantilever (which has a conductive chromium coating) is grounded, so the grounded electrical contact causes a negligible frequency shift. By contrast, the biased electrical contact shows a dramatic 2 Hz frequency shift relative to the cantilever's natural frequency. By incorporating a closed-loop Kelvin probe microscopy (KPM) technique, the sample's surface potential (in units of Volts) could be directly measured. The technique can also be used to characterize the quality of contact to graphene [204]. Even without a KPM controller, **Figure 5.4** makes evident the large voltage drops due to contact resistance between the gold electrodes and the graphene. Voltage drops in the graphene itself are also visible, particularly in the narrow regions, but appear smaller than

those from the contact resistance due to the V^2 dependence of δf. Three-point current-voltage measurements of the gold/graphene contacts found contact resistances of 11.5 kΩ and 10.3 kΩ for the left and right contacts, respectively. The total two-point resistance between the pair was found to be 36.6 kΩ, leaving the graphene channel with a 14.8 kΩ resistance. Because the graphene channel extends far above and below the image (~100 μm), current spreading is also observed. The inhomogeneity in local voltage requires further investigation, but is likely a result of charge impurities of the underlying SiO_2, or arises from residue on the graphene from the lithography processes involved in device fabrication.

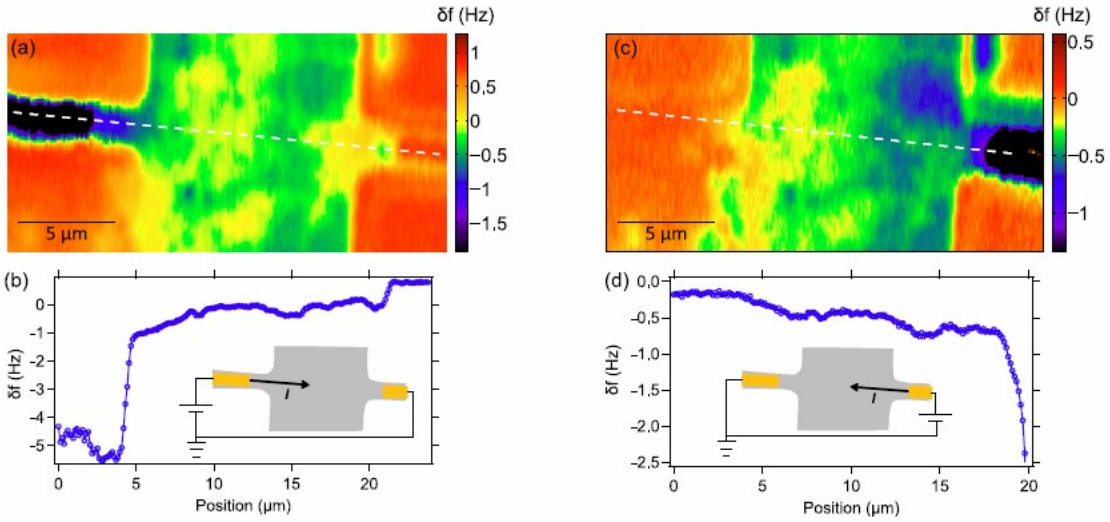

Figure 5.4 *EFM Images of a Biased Graphene Hall Cross*.

(a) 100 μA applied with left contact at V = $+V_0$, right contact at ground. (c) 100 μA applied with right contact at V = $+V_0$, left contact at ground. Panel (b) shows the line-cut indicated by white dashes in (a), while (d) represents the line-cut from (c). Insets in (b) and (d) show a schematic of the setup.

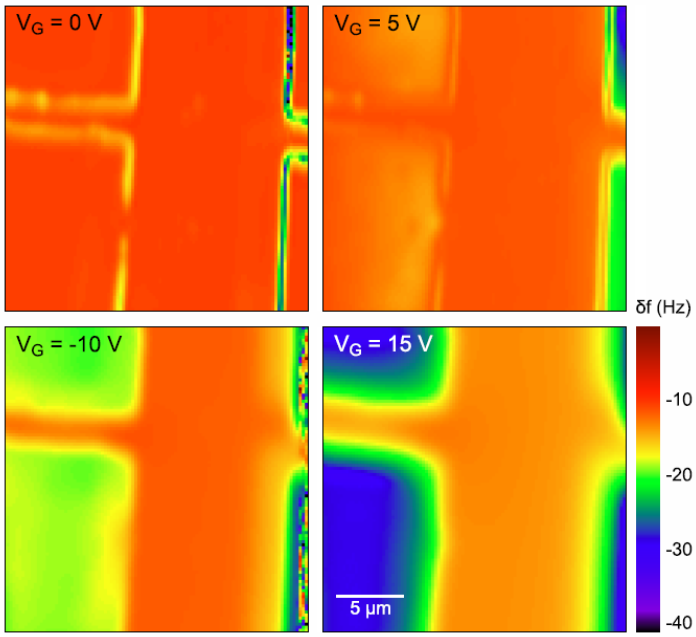

Figure 5.5 *EFM of a Graphene Hall Cross Under Varying Gate Bias.*

The force on the cantilever is sensitive only to V^2, and insensitive to the sign of the gate bias. When held above the graphene (and gold electrodes), the cantilever is shielded from the applied back gate, and experiences relatively little frequency shift. This technique could be used to easily locate a device, since the electrostatic force is fairly long-ranged [205]. All images, with the exception of V_G = 15 V, were taken at a nominal scan height of 340 nm. The cantilever was retracted to a height of 970 nm in order to acquire the image with V_G = 15 V, due to the increased electrostatic force causing tip-sample contact.

We have also acquired images under varying back gate conditions, as shown in **Figure 5.5**. The gate potential exerts a force on the cantilever, shifting its frequency. The image contrast is provided by shielding of the applied back gate by the grounded device (graphene and gold contacts), above which the cantilever experiences almost no frequency shift. The force on the cantilever does not depend on the sign of the voltage difference (since it is proportional to V^2). For example, an attractive force (negative frequency shift) is evident above the unshielded gate for both −10 V and +15 V. Because of the long range of electrostatic forces as compared to topographic forces, these images suggest a means for

helping to locate a device through a capacitance navigation technique [205]. This technique is demonstrated using the STM in Section 5.3.1.

5.2.4 Future Directions

Because of the flexibility of the software and hardware being used, it would be straightforward to expand the imaging and measurement modes of this instrument beyond cantilever force detection. For example, using a biased conducting tip, the device conductance could be monitored as a function of tip position (scanned gate imaging) [206-208]. Alternatively, the Hall voltage of a device such as that used in **Figure 5.4** could be monitored in order to quantify the stray magnetic field of an MFM tip [209]. This system has also been used in a magnetic force microscopy mode to correlate the magnetization of the magnetic electrodes on a graphene spin valve to the non-local spin signal [82]. It could be further employed to create a spin map of a graphene based lateral spin valve by monitoring the effect of a magnetic cantilever tip on the device's non-local voltage, as in scanned spin-precession imaging [210, 211]. Additional measurement protocols can be added in order to perform sensitive measurements. For example, the cantilever oscillations could be used as a lock-in reference, while monitoring the device voltage. Again, the modularity of the PXI chassis, the reprogrammability of the FPGA and control software, and the ease of interfacing LabVIEW with external instrumentation will make such measurements possible and relatively easy to implement.

5.3 Toward Simultaneous STM and Transport Studies in Graphene

For many potential device applications, the ability to tune (or introduce) a band gap and incorporate intrinsic dopants in graphene is critical. With the 2D, all surface nature of graphene, the material is extremely sensitive to its surrounding. This sensitivity can be utilized to manipulate the optical and electronic properties of this material through surface functionalization. Several approaches toward the surface functionalization with limited success of electronic tuning include substitutional doping, adatom binding, and the creation of lattice defects [212, 213]. In particular, the hydrogenation of graphene (graphane) shows evidence of opening up a band gap [78, 214]. Additionally, the use of vacancies as sites for the introduction of various dopants has been of limited experimental success, but often this results in the degradation of transport quality [215-227]. There is strong theoretical and experimental evidence to suggest that single carbon vacancies in the graphene lattice have magnetic moments [228-230]. Also, recently González-Herrero, *et al.* demonstrated local control of magnetism in graphene through the controlled chemisorption of hydrogen atoms on the surface [231].

Scanning tunneling microscopy (STM), with its ability to probe and modify the local atomic structure of surfaces, is a natural technique to apply toward the study of defects and surface modification of graphene. Indeed, graphene has already been imaged by STM on a wide variety of surfaces [214, 226, 232-234]. Recently, the Gupta group at The Ohio State University has used ultrahigh vacuum (UHV) grown graphene on Cu(111) to investigate natively occurring defects [235]. However, there is a clear need for studies that combine scanning (and modification) of the graphene surface with simultaneous *in-situ* electronic

transport measurements. This combination of techniques would aide in the investigation of how local changes to the atomic structure of graphene affect the macroscopic transport. One example of this in the literature is from Zhang *et al.* [236]. They successfully applied a gate voltage to exfoliated graphene flakes while performing scanning tunneling spectroscopy to investigate the electronic structure of the graphene. Here, we report on the progress toward simultaneous STM and electronic transport measurements as well as the initial experimental results. I primarily contributed to this through through the fabrication of graphene devices and the development of cleaning techniques to prepare samples for STM measurement. STM measurements were performed by the Gupta group.

5.3.1 Device Synthesis and STM considerations

Graphene Hall bar devices for this work were fabricated from CVD grown graphene using the same procedure described in Section 5.2.2 and **Appendix A**. A completed device is shown in **Figure 5.6**(a). Due to additional constraints imposed by the simultaneous STM and transport measurements, the device looks significantly different from the device shown in Section 5.2 (see **Figure 5.2**(a)). One of these challenges is the limited visual access to the sample when loaded in the STM. In addition, finding the small (10-100 μm) graphene device on the large (5 mm) insulating substrate without damaging the STM tip is a major hurdle (**Figure 5.6**(b)). Finally, the cleanliness of the graphene is important since samples are typically contaminated with organic residues during the transfer and lithographic processing steps.

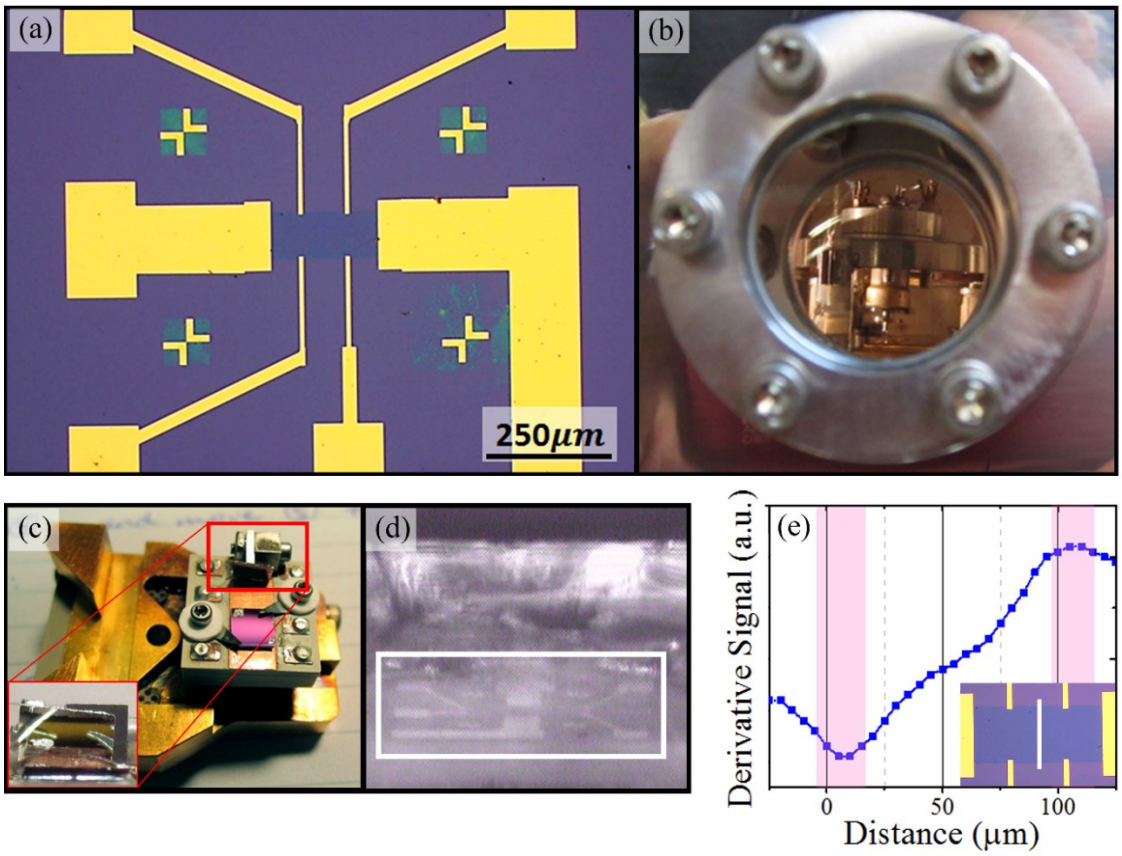

Figure 5.6 *Locating a Graphene Device.*

(a) Optical micrograph of first-generation graphene Hall bar device for STM measurements. (b) Picture of the STM viewport with the STM head in the center of the image. (c) STM device holder with sample mounted, showing the addition of a mirror for improved visual access to the device. The inset shows a horizontal view of the mirror. (d) Video image of a Hall bar device (white box) showing the difficulty in navigating an STM tip around with this limited visual access. (e) Example of the capacitance navigation technique for locating graphene edges on a device. Data taken across white line in inset.

The problem of limited visual access and graphene location is solved via a three-step solution. First, adding a mirror to the STM sample holder (**Figure 5.6**(c)) allows better sample illumination and enhances the intensity of the light reflected by the Au pattern on the sample. These effects dramatically increase device visibility (**Figure 5.6**(d)). In addition to these STM modifications, the device itself is modified to help locate the graphene in the microscope. The device is reshaped in an asymmetric manner with larger—

and thus better reflecting—Au contact pads, which aide in finding the graphene portion of the device. Further, these first-generation devices are designed with 100 μm graphene bars to make it easier to find the graphene. In the future, the width of the graphene bar will be decreased so that the scanning size of the STM tip makes up a significant fraction of the graphene bar width. Smaller widths dramatically increase the likelihood that changes in the graphene chemistry induced by the STM will have a noticeable effect on the transport properties.

Finally, the difficulty in locating the graphene bar with the STM tip is solved through the use of a capacitance navigation technique (as in Ref. [205]). The scanning range of the tip is exceedingly small (80 × 80 nm), compared to the size of the graphene substrate (5 × 5 mm). In this capacitance method the graphene device is grounded and a voltage is applied to the device back-gate. The STM tip is retracted from the sample to a height of 1-10 μm, and used in a fast-scan mode to monitor the derivative signal of the capacitance (essentially scanning the changes in the electric field). The peaks in this signal provide the location of the edges of the grounded conducting device. This technique works across the Au contacts as well as the graphene device itself. An example of the results of this process is shown in **Figure 5.6**(e). This electric field environment with the back-gate applied can be seen in the SPM measurements of similar graphene devices in **Figure 5.5**. The large block-like Au pads are designed so that this capacitance scanning can be used in an iterative manner. See Ref [205] for a description of this protocol. This process can be used to locate conducting edges on structures a micron in width, and possibly smaller.

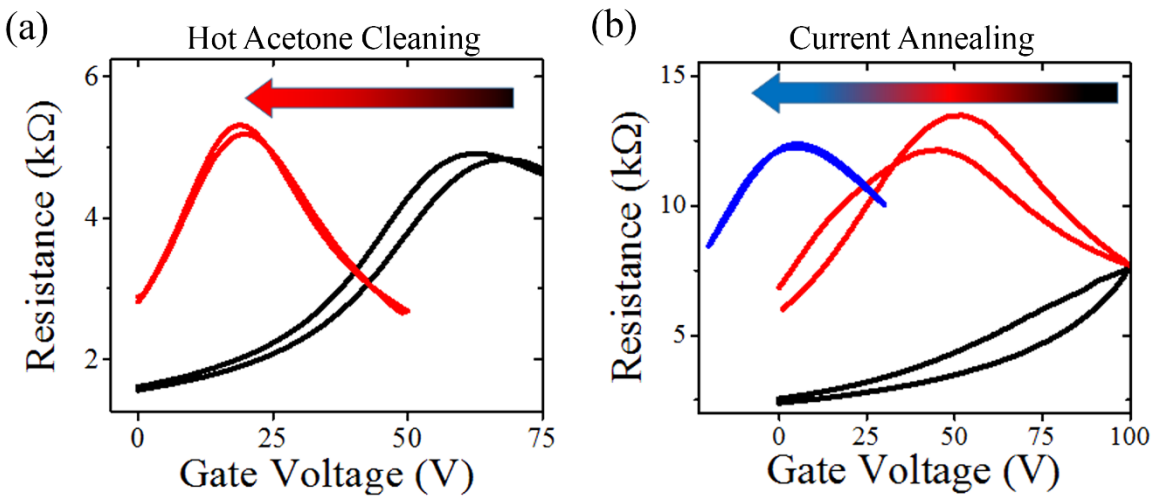

Figure 5.7 *Cleaning a Graphene Device.*

(a) Transport effects of hot acetone cleaning showing resistance vs. gate voltage for a graphene Hall bar device before cleaning (black) and after cleaning (red). (b) Transport effects of *in-situ* vacuum current annealing showing resistance vs. gate voltage for a graphene Hall bar device before current annealing (black), after one current annealing step (red), and after a second, longer current annealing step (blue). Note that the Dirac peak shifts well over 100V, and indicates almost zero doping afterwards.

Since we are interested in investigating graphene at an atomic scale, it is critical that the surface of the graphene is clean. This is a notorious problem with graphene that has been exposed to organic resists such as PMMA. The samples used here were exposed to resist contamination during both the transfer procedure (directly after the CVD growth on Cu), and during the two-step device fabrication process. We use a two-step cleaning procedure to remove any remaining resist residue on the graphene surface. First we perform a soak in hot acetone for 2-5 hours at 75 °C (in a water bath). We confirm the effect of this cleaning step through four-probe resistance measurements as a function of gate voltage. In contaminated graphene, the Dirac peak tends to be quite broad, and far from zero applied gate voltage. This indicates strong n-type doping with poor mobility (field effect transistor mobility is the proportional to the slope of the gated response). The effect of this hot

acetone cleaning step is shown in **Figure 5.7**(a), where the Dirac peak shifts 50 V closer to zero, and becomes considerably sharper.

The second annealing step takes place inside the STM load lock chamber, under vacuum. This step entails passing a high current (around 1 mA) through the graphene device under vacuum (as in Ref [72]) . This method, which desorbs contaminants from the surface, is highly effective and the results are shown in **Figure 5.7**(b). In this instance, the current annealing is performed in two-steps, shifting the Dirac peak by more than 100 V (the Dirac peak was not visible in the initial scan, as the gate voltage is limited to 100 V to prevent damage to the device), to nearly 0 V indicating only minor doping. Similarly to the hot acetone cleaning, we also see the peak width decrease, indicating a higher mobility in the sample after the cleaning. Devices are prepared using a combination of these two methods, with the *in-situ* annealing removing smaller scale organic contaminants and adsorbates from the graphene's exposure to air.

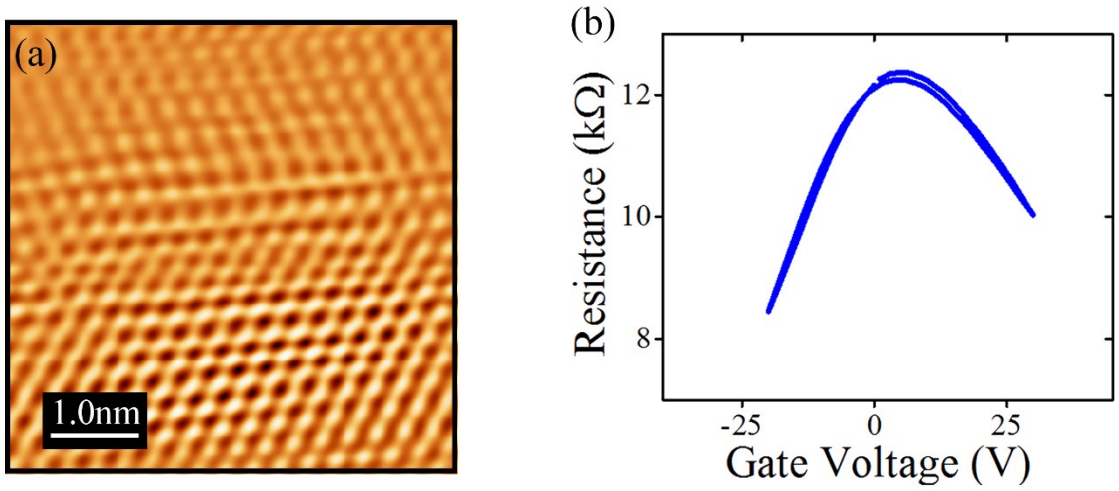

Figure 5.8 *STM and Transport Results*.

(a) STM image of a CVD grown, 100 μm wide, graphene Hall bar device. (b) Resistance vs gate voltage scan for a graphene Hall bar taken *in situ* after both the hot acetone and current annealing steps are performed.

5.3.2 Preliminary Results

With the combination of the two cleaning techniques, as well as the capacitance navigation technique, it is indeed possible to both locate the graphene Hall bar device with the STM tip and to perform an STM scan and transport measurements on the device. In this case, the scans were not completed simultaneously, but rather directly after each other (i.e. the transport properties were measured, followed by an STM scan). These proof-of-concept measurements are shown in **Figure 5.8**. The STM image in **Figure 5.8**(a) demonstrates the expected honey-comb lattice of graphene, however, the distance in this initial image is uncalibrated (the scale present is an estimation), so the observed lattice parameter cannot be matched directly to that of graphene. The *in-situ* transport resistance vs. gate voltage data in **Figure 5.8**(b) shows the expected Dirac peak around 0 V applied gate voltage, indicating a low doping.

5.3.3 Ongoing Work

These initial combined STM and *in situ* electronic transport measurements on graphene Hall bar device synthesized from CVD grown graphene indicate that many of the challenges involved in this project have been overcome. To our knowledge, this is the first time that STM has been performed on a fully functioning graphene device synthesized using standard lithography techniques. Already a second generation of devices have been synthesized—implementing lessons learned from the first generation devices. An example of the second generation device is shown in **Figure 5.9**. There are several differences in this device. First of all, the contact pattern is considerably different. After working with capacitance navigation technique on the first devices, we found that a device pattern with more steps from the large contact pads to the graphene would work considerably better. Additionally, the width of the graphene device is reduced from 100 μm to 10 μm in this device (some devices were as narrow as 1 μm). The size reduction allows the scanning range of the STM tip to be of a similar order of magnitude to the graphene Hall bar width. This nominally makes the local scanning affects and chemical modifications generated by the STM tip visible in the transport data. In particular, we are interested in looking at the effects of an *in-situ* partial hydrogenation technique (currently being pioneered by the Gupta group) on the electronic transport measurements.

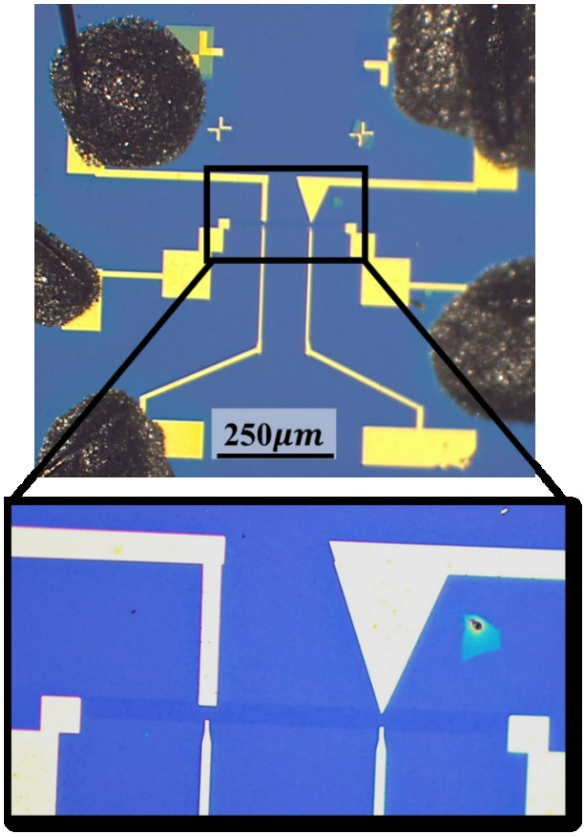

Figure 5.9 *Second Generation STM-Ready Graphene Device*.

(Top) Optical micrograph of 2nd generation graphene Hall bar prepared for simultaneous STM scanning and electrical transport measurements. (Bottom) zoomed in area of the central, graphene device region showing the 10 μm wide graphene region.

In order to better control the growth and transfer process of the graphene, an in-house graphene growth and transfer effort has been started. This effort is being executed by a group of undergraduate students and is named "The Graphene Factory." This group, started by Shawna Hollen and currently co-lead by Sara Mueller and myself, is in its third operating year at The Ohio State University, and the group has already had significant success at producing graphene grown on Cu substrates via CVD processes and transferred to SiO_2. This graphene will be utilized for these experiments as well as other graphene related efforts at The Ohio State University in the future.

5.4 Conclusion

In conclusion, we have made significant inroads toward the simultaneous scanning (via SPM or STM techniques) and electronic transport measurements on graphene Hall bar devices synthesized from CVD grown graphene. In particular, we've developed graphene device synthesis processes and geometries that can be use in both customized STM and SPM setups. Using a custom-made SPM instrument, EFM proof-of-concept studies have been performed on these graphene devices in both typical two-probe and gated contact geometries, demonstrating the sensitivity of the setup to the voltage landscape of the device under measurement (the former geometry) and the shielding effect of the graphene on the gated setup (the latter geometry). Utilizing the flexibility of this setup, we intend on expanding the capabilities of this system to investigate how localized, cantilever generated electromagnetic fields influence spin and electronic transport in graphene. Additionally, we have developed unique device geometries, cleaning techniques, and the ability to locate and approach the graphene device in our STM setup to make these combined microscopy and transport techniques possible. In addition, initial data has been taking STM scanning techniques on these graphene samples. These preliminary results demonstrate that the initial device and technique development has been successful. Additional modifications—primarily to the device geometry—are already being implemented and should be tested (along with the exciting partial hydrogenation technique) in the near future. By investigating the connection between localized surface modifications of graphene devices to the electronic transport in these devices, we hope to shed light on possible techniques to

tune the electronic properties of graphene without destroying the high mobility seen in this material.

5.5 Acknowledgements

This research was supported by funding from the Center for Emergent Materials: an NSF MRSEC, Award Number DMR-1420451, and DMR-0820414 and by the Army Research Office, ARO Award No. W911NF-12-1-0587. Technical support was provided by the NanoSystems Laboratory and NanoTech West at OSU

5.6 References

1. Novoselov, K.S., *et al.*, *Electric field effect in atomically thin carbon films.* Science. **306**(5696): p. 666-669. 2004. http://dx.doi.org/10.1126/science.1102896

2. Geim, A.K. and K.S. Novoselov, *The rise of graphene.* Nature Materials. **6**(3): p. 183-191. 2007. http://dx.doi.org/10.1038/nmat1849

3. Castro Neto, A.H., *et al.*, *The electronic properties of graphene.* Reviews of Modern Physics. **81**(1): p. 109-162. 2009. http://dx.doi.org/10.1103/RevModPhys.81.109

4. Cooper, D.R. and B. D'Anjou, *Experimental review of graphene.* ISRN Condensed Matter Physics. p. 501686-501686. 2012. http://dx.doi.org/10.5402/2012/501686

5. Xu, M., *et al.*, *Graphene-Like Two-Dimensional Materials.* Chemical Reviews. **113**(5): p. 3766-3798. 2013. http://dx.doi.org/10.1021/cr300263a

6. Geim, A.K., *Graphene: status and prospects.* Science. **324**(5934): p. 1530-4. 2009. http://dx.doi.org/10.1126/science.1158877

7. Novoselov, K.S., *et al.*, *A roadmap for graphene.* Nature. **490**(7419): p. 192-200. 2012. http://dx.doi.org/10.1038/nature11458

8. Das Sarma, S., *et al.*, *Electronic transport in two-dimensional graphene.* Reviews of Modern Physics. **83**(2): p. 407-470. 2011. http://dx.doi.org/10.1103/RevModPhys.83.407

9. Katsnelson, M.I., K.S. Novoselov, and a.K. Geim, *Chirial tunnelling and the Klein paradox in graphene.* Nature Physics. **2**(September): p. 620-625. 2006. http://dx.doi.org/10.1038/nphys384

12. Bolotin, K.I., *et al.*, *Ultrahigh electron mobility in suspended graphene.* Solid State Communications. **146**(9-10): p. 351-355. 2008. http://dx.doi.org/10.1016/j.ssc.2008.02.024

13. Morozov, S., *et al.*, *Giant Intrinsic Carrier Mobilities in Graphene and Its Bilayer.* Physical Review Letters. **100**(1): p. 016602-016602. 2008. http://dx.doi.org/10.1103/PhysRevLett.100.016602

14. Lau, C.N., W. Bao, and J. Velasco, *Properties of suspended graphene membranes.* Materials Today. **15**(6): p. 238-245. 2012. http://dx.doi.org/10.1016/S1369-7021(12)70114-1

23. Hynes, J.T., *et al.*, *The Focusing of Electron Flow and a Veselago Lens in Graphene p-n Junctions.* Science. **315**: p. 1252-1256. 2007. http://dx.doi.org/10.1126/science.1138020

24. Rickhaus, P., *et al.*, *Guiding of Electrons in a Few-Mode Ballistic Graphene Channel.* Nano Letters. **15**(9): p. 5819-5825. 2015. http://dx.doi.org/10.1021/acs.nanolett.5b01877

25. Singh, A.K., *et al.*, *Graphene based ballistic rectifiers.* Carbon. **84**(1): p. 124-129. 2015. http://dx.doi.org/10.1016/j.carbon.2014.11.064

26. Wilmart, Q., *et al.*, *A Klein-tunneling transistor with ballistic graphene.* 2D Materials. **1**(1): p. 011006-011006. 2014. http://dx.doi.org/10.1088/2053-1583/1/1/011006

27. Balandin, A.A., *Thermal properties of graphene and nanostructured carbon materials.* Nature Materials. **10**(8): p. 569-569. 2011. http://dx.doi.org/10.1038/nmat3064

28. Balandin, A.a.*, et al.*, *Superior Thermal Conductivity of Single-Layer Graphene.* Nano Letters. **8**(3): p. 902-907. 2008. http://dx.doi.org/10.1021/nl0731872

29. Han, W.*, et al.*, *Graphene spintronics.* Nature Nanotechnology. **9**(10): p. 794-807. 2014. http://dx.doi.org/10.1038/nnano.2014.214

30. Lee, C.*, et al.*, *Measurement of the Elastic Properties and Intrinsic Strength of Monolayer Graphene.* Science. **321**(July): p. 385-388. 2008. http://dx.doi.org/10.1126/science.1157996

33. Bonaccorso, F.*, et al.*, *2D materials. Graphene, related two-dimensional crystals, and hybrid systems for energy conversion and storage.* Science. **347**(6217): p. 1246501-1246501. 2015. http://dx.doi.org/10.1126/science.1246501

34. Das, S.*, et al.*, *Graphene synthesis and application for solar cells.* Journal of Materials Research. **29**(03): p. 299-319. 2014. http://dx.doi.org/10.1557/jmr.2013.297

35. Yin, Z.*, et al.*, *Graphene-Based materials for solar cell applications.* Advanced Energy Materials. **4**(1): p. 1-19. 2014. http://dx.doi.org/10.1002/aenm.201300574

39. Zhang, Y., L. Zhang, and C. Zhou, *Review of chemical vapor deposition of graphene and related applications.* Accounts of Chemical Research. **46**(10): p. 2329-2339. 2013. http://dx.doi.org/10.1021/ar300203n

40. Mattevi, C., H. Kim, and M. Chhowalla, *A review of chemical vapour deposition of graphene on copper.* Journal of Materials Chemistry. **21**(10): p. 3324-3334. 2011. http://dx.doi.org/10.1039/C0JM02126A

41. Kosynkin, D.V.*, et al.*, *Longitudinal unzipping of carbon nanotubes to form graphene nanoribbons.* Nature. **458**(7240): p. 872-876. 2009. http://dx.doi.org/10.1038/nature07872

42. Dreyer, D.R., R.S. Ruoff, and C.W. Bielawski, *From conception to realization: An historial account of graphene and some perspectives for its future.* Angewandte Chemie - International Edition. **49**(49): p. 9336-9344. 2010. http://dx.doi.org/10.1002/anie.201003024

43. Wintterlin, J. and M.L. Bocquet, *Graphene on metal surfaces.* Surface Science. **603**(10-12): p. 1841-1852. 2009. http://dx.doi.org/10.1016/j.susc.2008.08.037

44. Hernandez, Y.*, et al.*, *High-yield production of graphene by liquid-phase exfoliation of graphite.* Nature Nanotechnology. **3**(9): p. 563-568. 2008. http://dx.doi.org/10.1038/nnano.2008.215

45. Hackley, J.*, et al.*, *Graphitic carbon growth on Si(111) using solid source molecular beam epitaxy.* Applied Physics Letters. **95**(13): p. 1-4. 2009. http://dx.doi.org/10.1063/1.3242029

46. Virojanadara, C.*, et al.*, *Homogeneous large-area graphene layer growth on 6H-SiC(0001).* Physical Review B. **78**(24): p. 1-6. 2008. http://dx.doi.org/10.1103/PhysRevB.78.245403

47. Segal, M., *Selling graphene by the ton.* Nature Nanotechnology. **4**(10): p. 612-614. 2009. http://dx.doi.org/10.1038/nnano.2009.279

48. Riedl, C., C. Coletti, and U. Starke, *Structural and electronic properties of epitaxial graphene on SiC(0001): a review of growth, characterization, transfer doping and hydrogen intercalation.* Journal of Physics D: Applied Physics. **43**(37): p. 374009-374009. 2010. http://dx.doi.org/10.1088/0022-3727/43/37/374009

49. Yan, Z.*, et al.*, *Toward the synthesis of wafer-scale single-crystal graphene on copper foils.* ACS Nano. **6**(10): p. 9110-9117. 2012. http://dx.doi.org/10.1021/nn303352k

50. Kunkes, E.L.*, et al.*, *Large-Area Synthesis of High-Quality and Uniform Graphene Films on Copper Foil.* Science. **1381**(2002): p. 3-6. 2008. http://dx.doi.org/10.1126/science.1171245

51. Bae, S.*, et al.*, *Roll-to-roll production of 30-inch graphene films for transparent electrodes.* Nature Nanotechnology. **5**(8): p. 574-578. 2010. http://dx.doi.org/10.1038/nnano.2010.132

52. Kim, K.S.*, et al.*, *Large-scale pattern growth of graphene films for stretchable transparent electrodes.* Nature. **457**(7230): p. 706-10. 2009. http://dx.doi.org/10.1038/nature07719

53. Kang, J.*, et al.*, *Graphene transfer: key for applications.* Nanoscale. **4**: p. 5527-5537. 2012. http://dx.doi.org/10.1039/c2nr31317k

54. Gao, L.*, et al.*, *Repeated growth and bubbling transfer of graphene with millimetre-size single-crystal grains using platinum.* Nature Communications. **3**: p. 699-699. 2012. http://dx.doi.org/10.1038/ncomms1702

55. Mafra, D.L., T. Ming, and J. Kong, *Facile graphene transfer directly to target substrates with a reusable metal catalyst.* Nanoscale. **7**(36): p. 14807-14812. 2015. http://dx.doi.org/10.1039/C5NR03892H

56. Lin, W.-H.*, et al.*, *A Direct and Polymer-Free Method for Transferring Graphene Grown by Chemical Vapor Deposition to Any Substrate.* ACS Nano. **8**(2): p. 1784-1791. 2014. http://dx.doi.org/10.1021/nn406170d

57. Song, J.*, et al.*, *A general method for transferring graphene onto soft surfaces.* Nature Nanotechnology. **8**(5): p. 356-62. 2013. http://dx.doi.org/10.1038/nnano.2013.63

58. Barin, G.B.*, et al.*, *Optimized graphene transfer: Influence of polymethylmethacrylate (PMMA) layer concentration and baking time on grapheme final performance.* Carbon. **84**(C): p. 82-90. 2015. http://dx.doi.org/10.1016/j.carbon.2014.11.040

59. Ko, P.J.*, et al.*, *Simple method to transfer graphene from metallic catalytic substrates to flexible surfaces without chemical etching.* Journal of Physics: Conference Series. **433**(1): p. 012002-012002. 2013. http://dx.doi.org/10.1088/1742-6596/433/1/012002

60. Li, X.*, et al.*, *Transfer of large-area graphene films for high-performance transparent conductive electrodes.* Nano Letters. **9**(12): p. 4359-63. 2009. http://dx.doi.org/10.1021/nl902623y

61. Liang, X.*, et al.*, *Toward clean and crackless transfer of graphene.* ACS Nano. **5**(11): p. 9144-53. 2011. http://dx.doi.org/10.1021/nn203377t

72. Moser, J., a. Barreiro, and a. Bachtold, *Current-induced cleaning of graphene.* Applied Physics Letters. **91**(16): p. 163513-163513. 2007. http://dx.doi.org/10.1063/1.2789673

74. Jariwala, D., A. Srivastava, and P.M. Ajayan, *Graphene Synthesis and Band Gap Opening.* Journal of Nanoscience and Nanotechnology. **11**(8): p. 6621-6641. 2011. http://dx.doi.org/10.1166/jnn.2011.5001

75. Schwierz, F., *Graphene transistors.* Nature Nanotechnology. **5**(7): p. 487-96. 2010. http://dx.doi.org/10.1038/nnano.2010.89

76. Kim, K.*, et al.*, *A role for graphene in silicon-based semiconductor devices.* Nature. **479**(7373): p. 338-44. 2011. http://dx.doi.org/10.1038/nature10680

77. Lonkar, S.P., Y.S. Deshmukh, and A.A. Abdala, *Recent advances in chemical modifications of graphene.* Nano Research. 2014. http://dx.doi.org/10.1007/s12274-014-0622-9

78. Elias, D.C.*, et al.*, *Control of graphene's properties by reversible hydrogenation: evidence for graphane.* Science. **323**(5914): p. 610-3. 2009. http://dx.doi.org/10.1126/science.1167130

79. Nair, R.R.*, et al.*, *Fluorographene: A two-dimensional counterpart of Teflon.* Small. **6**(24): p. 2877-2884. 2010. http://dx.doi.org/10.1002/smll.201001555

80. Pi, K.*, et al.*, *Electronic doping and scattering by transition metals on graphene.* Physical Review B. **80**(7): p. 1-5. 2009. http://dx.doi.org/10.1103/PhysRevB.80.075406

81. Berger, A.J.*, et al.*, *A versatile LabVIEW and field-programmable gate array-based scanning probe microscope for in operando electronic device characterization.* Review of Scientific Instruments. **85**(12): p. 1-12. 2014. http://dx.doi.org/10.1063/1.4902934

82. Berger, A.J.*, et al.*, *Correlating spin transport and electrode magnetization in a graphene spin valve: Simultaneous magnetic microscopy and non-local measurements.* Applied Physics Letters. **107**(14). 2015. http://dx.doi.org/10.1063/1.4932673

203. Girard, P., *Electrostatic force microscopy: principles and some applications to semiconductors.* Nanotechnology. **12**(4): p. 485-490. 2001. http://dx.doi.org/10.1088/0957-4484/12/4/321

204. Yu, Y.-J.*, et al.*, *Tuning the Graphene Work Function by Electric Field Effect.* Nano Letters. **9**(10): p. 3430-3434. 2009. http://dx.doi.org/10.1021/nl901572a

205. Li, G., A. Luican, and E.Y. Andrei, *Self-navigation of a scanning tunneling microscope tip toward a micron-sized graphene sample.* Review of Scientific Instruments. **82**(7): p. 0-5. 2011. http://dx.doi.org/10.1063/1.3605664

206. Topinka, M.A.*, et al.*, *Imaging Coherent Electron Flow from a Quantum Point Contact.* Science. **289**(5488): p. 2323-2326. 2000. http://dx.doi.org/10.1126/science.289.5488.2323

207. Berezovsky, J.*, et al.*, *Imaging coherent transport in graphene. Part I: mapping universal conductance fluctuations.* Nanotechnology. **21**(27): p. 274013-274013. 2010. http://dx.doi.org/10.1088/0957-4484/21/27/274013

208. Topinka, M.A.*, et al.*, *Coherent branched flow in a two-dimensional electron gas.* Nature. **410**(6825): p. 183-186. 2001. http://dx.doi.org/10.1038/35065553

209. Panchal, V.*, et al.*, *Magnetic Scanning Probe Calibration Using Graphene Hall Sensor.* IEEE Transactions on Magnetics. **49**(7): p. 3520-3523. 2013. http://dx.doi.org/10.1109/TMAG.2013.2243127

210. Bhallamudi, V.P., *et al.*, *Imaging spin properties using spatially varying magnetic fields.* Journal of Applied Physics. **111**(1): p. 1-5. 2012. http://dx.doi.org/10.1063/1.3673259

211. Bhallamudi, V.P., *et al.*, *Experimental demonstration of scanned spin-precession microscopy.* Physical Review Letters. **111**(11): p. 1-5. 2013. http://dx.doi.org/10.1103/PhysRevLett.111.117201

212. Boukhvalov, D.W. and M.I. Katsnelson, *Chemical functionalization of graphene.* Journal of Physics: Condensed Matter. **21**(34): p. 344205-344205. 2009. http://dx.doi.org/10.1088/0953-8984/21/34/344205

213. Wang, B., Y.S. Puzyrev, and S.T. Pantelides, *Enhanced chemical reactions of oxygen at grain boundaries in polycrystalline graphene.* Polyhedron. **64**: p. 158-162. 2013. http://dx.doi.org/10.1016/j.poly.2013.03.032

214. Balog, R., *et al.*, *Bandgap opening in graphene induced by patterned hydrogen adsorption.* Nature Materials. **9**(4): p. 315-319. 2010. http://dx.doi.org/10.1038/nmat2710

215. Wang, H., *et al.*, *Doping monolayer graphene with single atom substitutions.* Nano Letters. **12**(1): p. 141-144. 2012. http://dx.doi.org/10.1021/nl2031629

216. Pantelides, S.T., *et al.*, *Defects and doping and their role in functionalizing graphene.* MRS Bulletin. **37**(12): p. 1187-1194. 2012. http://dx.doi.org/10.1557/mrs.2012.187

217. Bangert, U. and R. Zan, *Electronic functionalisation of graphene via external doping and dosing.* International Material Reviews. **60**(3): p. 133-149. 2015. http://dx.doi.org/10.1179/1743280414Y.0000000047

218. Vicarelli, L., *et al.*, *Controlling defects in graphene for optimizing the electrical properties of graphene nanodevices.* ACS Nano. **9**(4): p. 3428-3435. 2015. http://dx.doi.org/10.1021/acsnano.5b01762

219. Peres, N.M.R., F. Guinea, and A.H. Castro Neto, *Electronic properties of disordered two-dimensional carbon.* Physical Review B. **73**(12): p. 1-23. 2006. http://dx.doi.org/10.1103/PhysRevB.73.125411

220. Lherbier, A., *et al.*, *Charge Transport in Chemically Doped 2D Graphene.* Physical Review Letters. **101**(3): p. 036808-036808. 2008. http://dx.doi.org/10.1103/PhysRevLett.101.036808

221. Tsetseris, L., B. Wang, and S.T. Pantelides, *Substitutional doping of graphene: The role of carbon divacancies.* Physical Review B. **89**(3): p. 3-6. 2014. http://dx.doi.org/10.1103/PhysRevB.89.035411

222. Ugeda, M.M., *et al.*, *Electronic and structural characterization of divacancies in irradiated graphene.* Physical Review B. **85**(12): p. 2-6. 2012. http://dx.doi.org/10.1103/PhysRevB.85.121402

223. Wei, D., *et al.*, *Synthesis of N-doped graphene by chemical vapor deposition and its electrical properties.* Nano Letters. **9**(5): p. 1752-8. 2009. http://dx.doi.org/10.1021/nl803279t

224. Guo, B., *et al.*, *Controllable N-Doping of Graphene.* Nano Letters. p. 4975-4980. 2010. http://dx.doi.org/10.1021/nl103079j

225. Zhao, L., *et al.*, *Visualizing Individual Nitrogen Dopants in Monolayer Graphene.* Science. **333**: p. 999-1003. 2011. http://dx.doi.org/10.1007/s13398-014-0173-7.2

226. Zhao, L., *et al.*, *Local atomic and electronic structure of boron chemical doping in monolayer graphene.* Nano Letters. **13**(10): p. 4659-4665. 2013. http://dx.doi.org/10.1021/nl401781d

227. Tison, Y., *et al.*, *Electronic interaction between nitrogen atoms in doped graphene.* ACS Nano. **9**(1): p. 670-678. 2015. http://dx.doi.org/10.1021/nn506074u

228. Yazyev, O.V. and L. Helm, *Defect-induced magnetism in graphene.* Physical Review B. **75**(12): p. 1-5. 2007. http://dx.doi.org/10.1103/PhysRevB.75.125408

229. Ugeda, M.M., *et al.*, *Missing atom as a source of carbon magnetism.* Physical Review Letters. **104**(9): p. 1-4. 2010. http://dx.doi.org/10.1103/PhysRevLett.104.096804

230. Nair, R.R., *et al.*, *Spin-half paramagnetism in graphene induced by point defects.* Nature Physics. **8**(3): p. 199-202. 2012. http://dx.doi.org/10.1038/nphys2183

231. González-Herrero, H., *et al.*, *Atomic-scale control of graphene magnetism by using hydrogen atoms.* Science. **352**(6284): p. 437-441. 2016. http://dx.doi.org/10.1126/science.aad8038

232. Luican, A., G. Li, and E.Y. Andrei, *Scanning tunneling microscopy and spectroscopy of graphene layers on graphite.* Solid State Communications. **149**(27-28): p. 1151-1156. 2009. http://dx.doi.org/10.1016/j.ssc.2009.02.059

233. Stolyarova, E., *et al.*, *High-resolution scanning tunneling microscopy imaging of mesoscopic graphene sheets on an insulating surface.* Proceedings of the National Academy of Sciences of the United States of America. **104**(22): p. 9209-9212. 2007. http://dx.doi.org/10.1073/pnas.0703337104

234. Hollen, S.M., *et al.*, *Modification of electronic surface states by graphene islands on Cu(111).* Physical Review B. **91**(19): p. 30-35. 2015. http://dx.doi.org/10.1103/PhysRevB.91.195425

235. Hollen, S.M., *et al.*, *Native defects in ultra-high vacuum grown graphene islands on Cu(1 1 1).* Journal of Physics. Condensed Matter. **28**(3): p. 034003-034003. 2016. http://dx.doi.org/10.1088/0953-8984/28/3/034003

236. Zhang, Y., *et al.*, *Giant phonon-induced conductance in scanning tunnelling spectroscopy of gate-tunable graphene.* Nature Physics. **4**(8): p. 627-630. 2008. http://dx.doi.org/10.1038/nphys1022

Chapter 6: Conclusion

In just over a decade, the number of truly two-dimensional systems has exploded from the singular discovery of graphene in 2004, to the 40+ members of the transition metal dichalcogenides, the recent initial development of group IV graphene and graphane analogs in the past 2-3 years, and phosphorene in just this last year (to name only a few). These numerous materials exhibit a host of interesting and unique electronic, optoelectronic, and mechanical properties. This dissertation has detailed three distinct contributions to this growing body of research, which are summarized here.

1. Electronic transport measurements and finite element analysis were conducted on phosphorous doped germanane multi-layered crystals finding a strong dependency on water-vapor exposure and an anisotropy of up to 10^{11} between resistivity laterally in a single flake and vertically between the planes of stacked flakes. These results suggest the interesting possibility of measuring exotic single-layer properties in the top layer of a multilayered group IV graphane crystal by making electronic contact to only the top surface.

2. A novel growth methodology was developed which produces uniform, high-quality, templated MoS_2 by the sulfurization of Mo deposited through a SiN stencil. This resist-less stenciled sulfurization methodology is a facile and inexpensive

route to pre-patterned MoS_2 monolayer films without concern for organic contaminants which can aide in the investigation of sulfurization growth dynamics and have the potential to be a powerful tool for the creation of vertically stacked 2D heterostructures.

3. A considerable amount of progress has been made toward simultaneous scanning (via SPM or STM techniques) and electronic transport measurements on graphene Hall bar devices synthesized from CVD grown graphene. This work includes the development and synthesis of instrument specific graphene Hall bar devices, and of methodologies for finding and imaging this devices. Investigating the connection between localized surface modifications of graphene and electronic will help shed light on possible techniques to tune the electronic properties of graphene without destroying the high mobility seen in this material.

These three distinct contributions demonstrate the both the powerful potential, and the challenges pertaining to extreme sensitivity of these all surface 2D material systems to surface interactions. In GeH, we observed that the transport in multi-layer samples is dominated by the sensitivity of the surface layers to water in the atmosphere. The utilization of SiN masks in a TMD growth process critically enables the creation of patterned single-layer MoS_2 films with pristine surfaces suitable for subsequent modification via functionalization and mechanical stacking. Finally, in graphene we observed the challenges involved in synthesizing clean graphene devices that can be used in STM and SPM transport studies which will be used to investigate the effects of local surface functionalization on the transport in graphene. While three distinct materials and

projects, they all demonstrate the importance of the study of these surface interactions and the development of pristine 2D surfaces is to the ever-growing field of two-dimensional materials.

Bibliography

1. Novoselov, K.S., *et al.*, *Electric field effect in atomically thin carbon films.* Science. **306**(5696): p. 666-669. 2004. http://dx.doi.org/10.1126/science.1102896

2. Geim, A.K. and K.S. Novoselov, *The rise of graphene.* Nature Materials. **6**(3): p. 183-191. 2007. http://dx.doi.org/10.1038/nmat1849

3. Castro Neto, A.H., *et al.*, *The electronic properties of graphene.* Reviews of Modern Physics. **81**(1): p. 109-162. 2009. http://dx.doi.org/10.1103/RevModPhys.81.109

4. Cooper, D.R. and B. D'Anjou, *Experimental review of graphene.* ISRN Condensed Matter Physics. p. 501686-501686. 2012. http://dx.doi.org/10.5402/2012/501686

5. Xu, M., *et al.*, *Graphene-Like Two-Dimensional Materials.* Chemical Reviews. **113**(5): p. 3766-3798. 2013. http://dx.doi.org/10.1021/cr300263a

6. Geim, A.K., *Graphene: status and prospects.* Science. **324**(5934): p. 1530-4. 2009. http://dx.doi.org/10.1126/science.1158877

7. Novoselov, K.S., *et al.*, *A roadmap for graphene.* Nature. **490**(7419): p. 192-200. 2012. http://dx.doi.org/10.1038/nature11458

8. Das Sarma, S., *et al.*, *Electronic transport in two-dimensional graphene.* Reviews of Modern Physics. **83**(2): p. 407-470. 2011. http://dx.doi.org/10.1103/RevModPhys.83.407

9. Katsnelson, M.I., K.S. Novoselov, and a.K. Geim, *Chirial tunnelling and the Klein paradox in graphene.* Nature Physics. **2**(September): p. 620-625. 2006. http://dx.doi.org/10.1038/nphys384

10. Novoselov, K.S., *et al.*, *Two-Dimensional Gas of Massless Dirac Fermions in Graphene.* Nature. **438**(7065): p. 197-200. 2005. http://dx.doi.org/10.1038/nature04233

11. Novoselov, K.S., *et al.*, *Room-Temperature Quantum Hall Effect in Graphene.* Science. **315**(5817): p. 1379-1379. 2007. http://dx.doi.org/10.1126/science.1137201

12. Bolotin, K.I., *et al.*, *Ultrahigh electron mobility in suspended graphene.* Solid State Communications. **146**(9-10): p. 351-355. 2008. http://dx.doi.org/10.1016/j.ssc.2008.02.024

13. Morozov, S., *et al.*, *Giant Intrinsic Carrier Mobilities in Graphene and Its Bilayer.* Physical Review Letters. **100**(1): p. 016602-016602. 2008. http://dx.doi.org/10.1103/PhysRevLett.100.016602

14. Lau, C.N., W. Bao, and J. Velasco, *Properties of suspended graphene membranes.* Materials Today. **15**(6): p. 238-245. 2012. http://dx.doi.org/10.1016/S1369-7021(12)70114-1

15. Zhang, Y., *et al.*, *Experimental observation of the quantum Hall effect and Berry's phase in graphene.* Nature. **438**(7065): p. 201-204. 2005. http://dx.doi.org/10.1038/nature04235

16. Du, X., *et al.*, *Fractional quantum Hall effect and insulating phase of Dirac electrons in graphene.* Nature. **462**(7270): p. 192-5. 2009. http://dx.doi.org/10.1038/nature08522

17. Nagashio, K., *et al.*, *Electrical transport properties of graphene on SiO2 with specific surface structures.* Journal of Applied Physics. **110**(2). 2011. http://dx.doi.org/10.1063/1.3611394

18. Dean, C.R., *et al.*, *Boron nitride substrates for high-quality graphene electronics.* Nature Nanotechnology. **5**(10): p. 722-6. 2010. http://dx.doi.org/10.1038/nnano.2010.172

19. Mayorov, A.S., *et al.*, *Direct evidence for micron-scale ballistic transport in encapsulated graphene at room temperature.* Nano Letters. **11**: p. 2396-2399. 2011. http://dx.doi.org/10.1021/nl200758b

20. Wang, L., *et al.*, *One-dimensional electrical contact to a two-dimensional material.* Science. **342**(6158): p. 614-7. 2013. http://dx.doi.org/10.1126/science.1244358

21. Banszerus, L., *et al.*, *Ballistic transport exceeding 28 um in CVD grown graphene.* Nano Letters. **16**: p. 1387-1391. 2015. http://dx.doi.org/10.1021/acs.nanolett.5b04840

22. Wang, L., *et al.*, *Fractional fractal quantum Hall effect in graphene superlattices.* Science. **350**(6265): p. 1231-1231. 2015. http://dx.doi.org/10.1126/science.aad2102

23. Hynes, J.T., *et al.*, *The Focusing of Electron Flow and a Veselago Lens in Graphene p-n Junctions.* Science. **315**: p. 1252-1256. 2007. http://dx.doi.org/10.1126/science.1138020

24. Rickhaus, P., *et al.*, *Guiding of Electrons in a Few-Mode Ballistic Graphene Channel.* Nano Letters. **15**(9): p. 5819-5825. 2015. http://dx.doi.org/10.1021/acs.nanolett.5b01877

25. Singh, A.K., *et al.*, *Graphene based ballistic rectifiers.* Carbon. **84**(1): p. 124-129. 2015. http://dx.doi.org/10.1016/j.carbon.2014.11.064

26. Wilmart, Q., *et al.*, *A Klein-tunneling transistor with ballistic graphene.* 2D Materials. **1**(1): p. 011006-011006. 2014. http://dx.doi.org/10.1088/2053-1583/1/1/011006

27. Balandin, A.A., *Thermal properties of graphene and nanostructured carbon materials.* Nature Materials. **10**(8): p. 569-569. 2011. http://dx.doi.org/10.1038/nmat3064

28. Balandin, A.a., *et al.*, *Superior Thermal Conductivity of Single-Layer Graphene.* Nano Letters. **8**(3): p. 902-907. 2008. http://dx.doi.org/10.1021/nl0731872

29. Han, W., *et al.*, *Graphene spintronics.* Nature Nanotechnology. **9**(10): p. 794-807. 2014. http://dx.doi.org/10.1038/nnano.2014.214

30. Lee, C., *et al.*, *Measurement of the Elastic Properties and Intrinsic Strength of Monolayer Graphene.* Science. **321**(July): p. 385-388. 2008. http://dx.doi.org/10.1126/science.1157996

31. Chen, S., *et al.*, *Oxidation resistance of graphene-coated Cu and Cu Ni alloy.* ACS nano. **5**(2): p. 1321-7. 2011. http://dx.doi.org/10.1021/nn103028d

32. Bunch, J.S., *et al.*, *Impermeable atomic membranes from graphene sheets.* Nano Letters. **8**(8): p. 2458-2462. 2008. http://dx.doi.org/10.1021/nl801457b

33. Bonaccorso, F., *et al.*, *2D materials. Graphene, related two-dimensional crystals, and hybrid systems for energy conversion and storage.* Science. **347**(6217): p. 1246501-1246501. 2015. http://dx.doi.org/10.1126/science.1246501

34. Das, S., *et al.*, *Graphene synthesis and application for solar cells.* Journal of Materials Research. **29**(03): p. 299-319. 2014. http://dx.doi.org/10.1557/jmr.2013.297

35. Yin, Z., *et al.*, *Graphene-Based materials for solar cell applications.* Advanced Energy Materials. **4**(1): p. 1-19. 2014. http://dx.doi.org/10.1002/aenm.201300574

36. Blake, P., *et al.*, *Making graphene visible.* Applied Physics Letters. **91**(6): p. 33-36. 2007. http://dx.doi.org/10.1063/1.2768624

37. Nair, R.R., *et al.*, *Fine structure constant defines visual transparency of graphene.* Science. **320**(5881): p. 1308-1308. 2008. http://dx.doi.org/10.1126/science.1156965

38. Bonaccorso, F., *et al.*, *Graphene Photonics and Optoelectronics.* Nature Photonics. **4**(9): p. 611-622. 2010. http://dx.doi.org/10.1038/nphoton.2010.186

39. Zhang, Y., L. Zhang, and C. Zhou, *Review of chemical vapor deposition of graphene and related applications.* Accounts of Chemical Research. **46**(10): p. 2329-2339. 2013. http://dx.doi.org/10.1021/ar300203n

40. Mattevi, C., H. Kim, and M. Chhowalla, *A review of chemical vapour deposition of graphene on copper.* Journal of Materials Chemistry. **21**(10): p. 3324-3334. 2011. http://dx.doi.org/10.1039/C0JM02126A

41. Kosynkin, D.V., *et al.*, *Longitudinal unzipping of carbon nanotubes to form graphene nanoribbons.* Nature. **458**(7240): p. 872-876. 2009. http://dx.doi.org/10.1038/nature07872

42. Dreyer, D.R., R.S. Ruoff, and C.W. Bielawski, *From conception to realization: An historial account of graphene and some perspectives for its future.* Angewandte Chemie - International Edition. **49**(49): p. 9336-9344. 2010. http://dx.doi.org/10.1002/anie.201003024

43. Wintterlin, J. and M.L. Bocquet, *Graphene on metal surfaces.* Surface Science. **603**(10-12): p. 1841-1852. 2009. http://dx.doi.org/10.1016/j.susc.2008.08.037

44. Hernandez, Y., *et al.*, *High-yield production of graphene by liquid-phase exfoliation of graphite.* Nature Nanotechnology. **3**(9): p. 563-568. 2008. http://dx.doi.org/10.1038/nnano.2008.215

45. Hackley, J., *et al.*, *Graphitic carbon growth on Si(111) using solid source molecular beam epitaxy.* Applied Physics Letters. **95**(13): p. 1-4. 2009. http://dx.doi.org/10.1063/1.3242029

46. Virojanadara, C., *et al.*, *Homogeneous large-area graphene layer growth on 6H-SiC(0001).* Physical Review B. **78**(24): p. 1-6. 2008. http://dx.doi.org/10.1103/PhysRevB.78.245403

47. Segal, M., *Selling graphene by the ton.* Nature Nanotechnology. **4**(10): p. 612-614. 2009. http://dx.doi.org/10.1038/nnano.2009.279

48. Riedl, C., C. Coletti, and U. Starke, *Structural and electronic properties of epitaxial graphene on SiC(0001): a review of growth, characterization, transfer doping and hydrogen intercalation.* Journal of Physics D: Applied Physics. **43**(37): p. 374009-374009. 2010. http://dx.doi.org/10.1088/0022-3727/43/37/374009

49. Yan, Z.*, et al.*, *Toward the synthesis of wafer-scale single-crystal graphene on copper foils.* ACS Nano. **6**(10): p. 9110-9117. 2012. http://dx.doi.org/10.1021/nn303352k

50. Kunkes, E.L.*, et al.*, *Large-Area Synthesis of High-Quality and Uniform Graphene Films on Copper Foil.* Science. **1381**(2002): p. 3-6. 2008. http://dx.doi.org/10.1126/science.1171245

51. Bae, S.*, et al.*, *Roll-to-roll production of 30-inch graphene films for transparent electrodes.* Nature Nanotechnology. **5**(8): p. 574-578. 2010. http://dx.doi.org/10.1038/nnano.2010.132

52. Kim, K.S.*, et al.*, *Large-scale pattern growth of graphene films for stretchable transparent electrodes.* Nature. **457**(7230): p. 706-10. 2009. http://dx.doi.org/10.1038/nature07719

53. Kang, J.*, et al.*, *Graphene transfer: key for applications.* Nanoscale. **4**: p. 5527-5537. 2012. http://dx.doi.org/10.1039/c2nr31317k

54. Gao, L.*, et al.*, *Repeated growth and bubbling transfer of graphene with millimetre-size single-crystal grains using platinum.* Nature Communications. **3**: p. 699-699. 2012. http://dx.doi.org/10.1038/ncomms1702

55. Mafra, D.L., T. Ming, and J. Kong, *Facile graphene transfer directly to target substrates with a reusable metal catalyst.* Nanoscale. **7**(36): p. 14807-14812. 2015. http://dx.doi.org/10.1039/C5NR03892H

56. Lin, W.-H.*, et al.*, *A Direct and Polymer-Free Method for Transferring Graphene Grown by Chemical Vapor Deposition to Any Substrate.* ACS Nano. **8**(2): p. 1784-1791. 2014. http://dx.doi.org/10.1021/nn406170d

57. Song, J.*, et al.*, *A general method for transferring graphene onto soft surfaces.* Nature Nanotechnology. **8**(5): p. 356-62. 2013. http://dx.doi.org/10.1038/nnano.2013.63

58. Barin, G.B.*, et al.*, *Optimized graphene transfer: Influence of polymethylmethacrylate (PMMA) layer concentration and baking time on grapheme final performance.* Carbon. **84**(C): p. 82-90. 2015. http://dx.doi.org/10.1016/j.carbon.2014.11.040

59. Ko, P.J.*, et al.*, *Simple method to transfer graphene from metallic catalytic substrates to flexible surfaces without chemical etching.* Journal of Physics: Conference Series. **433**(1): p. 012002-012002. 2013. http://dx.doi.org/10.1088/1742-6596/433/1/012002

60. Li, X.*, et al.*, *Transfer of large-area graphene films for high-performance transparent conductive electrodes.* Nano Letters. **9**(12): p. 4359-63. 2009. http://dx.doi.org/10.1021/nl902623y

61. Liang, X.*, et al.*, *Toward clean and crackless transfer of graphene.* ACS Nano. **5**(11): p. 9144-53. 2011. http://dx.doi.org/10.1021/nn203377t

62. Novoselov, K.S. and a.H. Castro Neto, *Two-dimensional crystals-based heterostructures: materials with tailored properties.* Physica Scripta. **T146**: p. 014006-014006. 2012. http://dx.doi.org/10.1088/0031-8949/2012/T146/014006

63. Kumar, A. and C.H. Lee, *Synthesis and Biomedical Applications of Graphene: Present and Future Trends*. Advances in Graphene Science. 2013.

64. Li, X.*, et al.*, *Evolution of graphene growth on Ni and Cu by carbon isotope labeling.* Nano Letters. **9**(12): p. 4268-4272. 2009. http://dx.doi.org/10.1021/nl902515k

65. Li, X.*, et al.*, *Large-area graphene single crystals grown by low-pressure chemical vapor deposition of methane on copper.* JACS Communication. **133**(9): p. 2816-2819. 2011. http://dx.doi.org/10.1021/ja109793s

66. Hao, Y.*, et al.*, *The role of surface oxygen in the growth of large single-crystal graphene on copper.* Science. **342**(6159): p. 720-3. 2013. http://dx.doi.org/10.1126/science.1243879

67. Banszerus, L.*, et al.*, *Ultrahigh-mobility graphene devices from chemical vapor deposition on reusable copper.* Science Advances. **1**(6): p. 1-6. 2015. http://dx.doi.org/10.1126/sciadv.1500222

68. Huang, P.Y.*, et al.*, *Grains and grain boundaries in single-layer graphene atomic patchwork quilts.* Nature. **469**(7330): p. 389-92. 2011. http://dx.doi.org/10.1038/nature09718

69. Brown, L.*, et al.*, *Polycrystalline graphene with single crystalline electronic structure.* Nano Letters. **14**(10): p. 5706-5711. 2014. http://dx.doi.org/10.1021/nl502445j

70. Cheng, Z.*, et al.*, *Toward intrinsic graphene surfaces: a systematic study on thermal annealing and wet-chemical treatment of SiO2-supported graphene devices.* Nano Letters. **11**(2): p. 767-71. 2011. http://dx.doi.org/10.1021/nl103977d

71. Lin, Y.-C.*, et al.*, *Graphene annealing: how clean can it be?* Nano Letters. **12**(1): p. 414-9. 2012. http://dx.doi.org/10.1021/nl203733r

72. Moser, J., a. Barreiro, and a. Bachtold, *Current-induced cleaning of graphene.* Applied Physics Letters. **91**(16): p. 163513-163513. 2007. http://dx.doi.org/10.1063/1.2789673

73. Wang, Y.*, et al.*, *Electrochemical delamination of CVD-grown graphene film: Toward the recyclable use of copper catalyst.* ACS Nano. **5**(12): p. 9927-9933. 2011. http://dx.doi.org/10.1021/nn203700w

74. Jariwala, D., A. Srivastava, and P.M. Ajayan, *Graphene Synthesis and Band Gap Opening.* Journal of Nanoscience and Nanotechnology. **11**(8): p. 6621-6641. 2011. http://dx.doi.org/10.1166/jnn.2011.5001

75. Schwierz, F., *Graphene transistors.* Nature Nanotechnology. **5**(7): p. 487-96. 2010. http://dx.doi.org/10.1038/nnano.2010.89

76. Kim, K.*, et al.*, *A role for graphene in silicon-based semiconductor devices.* Nature. **479**(7373): p. 338-44. 2011. http://dx.doi.org/10.1038/nature10680

77. Lonkar, S.P., Y.S. Deshmukh, and A.A. Abdala, *Recent advances in chemical modifications of graphene.* Nano Research. 2014. http://dx.doi.org/10.1007/s12274-014-0622-9

78. Elias, D.C.*, et al.*, *Control of graphene's properties by reversible hydrogenation: evidence for graphane.* Science. **323**(5914): p. 610-3. 2009. http://dx.doi.org/10.1126/science.1167130

79. Nair, R.R., *et al.*, *Fluorographene: A two-dimensional counterpart of Teflon.* Small. **6**(24): p. 2877-2884. 2010. http://dx.doi.org/10.1002/smll.201001555

80. Pi, K., *et al.*, *Electronic doping and scattering by transition metals on graphene.* Physical Review B. **80**(7): p. 1-5. 2009. http://dx.doi.org/10.1103/PhysRevB.80.075406

81. Berger, A.J., *et al.*, *A versatile LabVIEW and field-programmable gate array-based scanning probe microscope for in operando electronic device characterization.* Review of Scientific Instruments. **85**(12): p. 1-12. 2014. http://dx.doi.org/10.1063/1.4902934

82. Berger, A.J., *et al.*, *Correlating spin transport and electrode magnetization in a graphene spin valve: Simultaneous magnetic microscopy and non-local measurements.* Applied Physics Letters. **107**(14). 2015. http://dx.doi.org/10.1063/1.4932673

83. Novoselov, K.S., *et al.*, *Two-dimensional atomic crystals.* Proceedings of the National Academy of Sciences of the United States of America. **102**(30): p. 10451-10453. 2005. http://dx.doi.org/10.1073/pnas.0502848102

84. Bhimanapati, G.R., *et al.*, *Recent Advances in Two-Dimensional Materials beyond Graphene.* ACS Nano. **9**(12): p. 11509-11539. 2015. http://dx.doi.org/10.1021/acsnano.5b05556

85. Das, S., *et al.*, *Beyond Graphene: Progress in Novel Two-Dimensional Materials and van der Waals Solids.* Annual Review of Materials Research. **45**(1): p. 1-27. 2015. http://dx.doi.org/10.1146/annurev-matsci-070214-021034

86. Butler, S.Z., *et al.*, *Progress, Challenges, and Opportunities in Two-Dimensional Materials Beyond Graphene.* ACS Nano. **7**(4): p. 2898-2926. 2013. http://dx.doi.org/10.1021/nn400280c

87. Mas-Ballesté, R., *et al.*, *2D materials: to graphene and beyond.* Nanoscale. **3**(1): p. 20-30. 2011. http://dx.doi.org/10.1039/c0nr00323a

88. Gupta, A., T. Sakthivel, and S. Seal, *Recent development in 2D materials beyond graphene.* Progress in Materials Science. **73**: p. 44-126. 2015. http://dx.doi.org/10.1016/j.pmatsci.2015.02.002

89. Wilson, J.A. and A.D. Yoffe, *The transition metal dichalcogenides discussion and interpretation of the observed optical, electrical and structural properties.* Advances in Physics. **18**(73): p. 193-335. 1969. http://dx.doi.org/10.1080/00018736900101307

90. Ataca, C., H. Sahin, and S. Ciraci, *Stable, Single-Layer MX2 Transition-Metal Oxides and Dichalcogenides in a Honeycomb-Like Structure.* The Journal of Physical Chemistry C. **116**: p. 8983-8999. 2012. http://dx.doi.org/10.1021/jp212558p

91. Wang, Q.H., *et al.*, *Electronics and optoelectronics of two-dimensional transition metal dichalcogenides.* Nature Nanotechnology. **7**(11): p. 699-712. 2012. http://dx.doi.org/10.1038/nnano.2012.193

92. Chhowalla, M., *et al.*, *The chemistry of two-dimensional layered transition metal dichalcogenide nanosheets.* Nature Chemistry. **5**(4): p. 263-75. 2013. http://dx.doi.org/10.1038/nchem.1589

93. Jariwala, D., *et al.*, *Emerging Device Applications for for Semiconducting Two-Dimensional Transition Metal Dichalcogenides.* ACS Nano. **8**(2): p. 1102-1120. 2014. http://dx.doi.org/10.1021/nn500064s

94. Mak, K.F., *et al.*, *Atomically thin MoS2: a new direct-gap semiconductor.* Physical Review Letters. **105**(13): p. 136805. 2010. http://dx.doi.org/10.1103/PhysRevLett.105.136805

95. Splendiani, A., *et al.*, *Emerging photoluminescence in monolayer MoS2.* Nano Letters. **10**(4): p. 1271-1275. 2010. http://dx.doi.org/10.1021/nl903868w

96. Lee, G.-h., *et al.*, *Highly Stable , Dual-Gated MoS2 Transistors Encapsulated by Hexagonal Boron Nitride with Gate-Controllable Contact, Resistane and Threshold Voltage.* ACS Nano. **9**: p. 7019-7019. 2015. http://dx.doi.org/10.1021/acsnano.5b01341

97. Choi, W., *et al.*, *High-detectivity multilayer MoS2 phototransistors with spectral response from ultraviolet to infrared.* Advanced Materials. **24**(43): p. 5832-5836. 2012. http://dx.doi.org/10.1002/adma.201201909

98. Bertolazzi, S., D. Krasnozhon, and A. Kis, *Nonvolatile memory cells based on MoS2/graphene heterostructures.* ACS Nano. **7**(4): p. 3246-3252. 2013. http://dx.doi.org/10.1021/nn3059136

99. Bao, W., *et al.*, *High mobility ambipolar MoS2 field-effect transistors: Substrate and dielectric effects.* Applied Physics Letters. **102**(4). 2013. http://dx.doi.org/10.1063/1.4789365

100. Bertolazzi, S., J. Brivio, and A. Kis, *Stretching and breaking of ultrathin MoS2.* ACS Nano. **5**(12): p. 9703-9709. 2011. http://dx.doi.org/10.1021/nn203879f

101. Heiranian, M., A.B. Farimani, and N.R. Aluru, *Water desalination with a single-layer MoS2 nanopore.* Nature Communications. **6**: p. 1-6. 2015. http://dx.doi.org/10.1038/ncomms9616

102. Lee, G.-H., *et al.*, *Flexible and Transparent MoS2 Field-Effect Transistors on Hexagonal Boron Nitride-Graphene Heterostructures.* ACS Nano. **7**(9): p. 7931-7936. 2013. http://dx.doi.org/10.1021/nn402954e

103. Akinwande, D., N. Petrone, and J. Hone, *Two-dimensional flexible nanoelectronics.* Nature Communications. **5**: p. 5678-5678. 2014. http://dx.doi.org/10.1038/ncomms6678

104. Kam, K.K. and B.A. Parkinson, *Detailed Photocurrent Spectroscopy.* Journal of Physical Chemistry. **86**: p. 463-467. 1982. http://dx.doi.org/10.1021/j100393a010

105. Smith, R.J., *et al.*, *Large-scale exfoliation of inorganic layered compounds in aqueous surfactant solutions.* Advanced Materials. **23**(34): p. 3944-3948. 2011. http://dx.doi.org/10.1002/adma.201102584

106. Hunt, B., *et al.*, *Massive Dirac fermions and Hofstadter butterfly in van der Waals heterostructure.* Science. **340**(6139): p. 1427-1430. 2013. http://dx.doi.org/10.1126/science.1237240

107. Lebègue, S. and O. Eriksson, *Electronic structure of two-dimensional crystals from ab initio theory.* Physical Review B. **79**(11): p. 4-7. 2009. http://dx.doi.org/10.1103/PhysRevB.79.115409

108. Kuc, A., N. Zibouche, and T. Heine, *Influence of quantum confinement on the electronic structure of the transition metal sulfide TS2.* Physical Review B. **83**(24): p. 245213-245213. 2011. http://dx.doi.org/10.1103/PhysRevB.83.245213

109. Chang, H.Y., *et al.*, *High-performance, highly bendable MoS2 transistors with high-K dielectrics for flexible low-power systems.* ACS Nano. **7**(6): p. 5446-5452. 2013. http://dx.doi.org/10.1021/nn401429w

110. Radisavljevic, B., *et al.*, *Single-layer MoS2 transistors.* Nature Nanotechnology. **6**(3): p. 147-150. 2011. http://dx.doi.org/10.1038/nnano.2010.279

111. Radisavljevic, B., M.B. Whitwick, and A. Kis, *Integrated circuits and logic operations based on single-layer MoS2.* ACS Nano. **5**(12): p. 9934-9938. 2011. http://dx.doi.org/10.1021/nn203715c

112. Kim, K.K., *et al.*, *Synthesis of monolayer hexagonal boron nitride on Cu foil using chemical vapor deposition.* Nano Letters. **12**(1): p. 161-166. 2012. http://dx.doi.org/10.1021/nl203249a

113. Mak, K.F., *et al.*, *The valley Hall effect in MoS_2 transistors.* Science. **344**(6191): p. 1489-92. 2014. http://dx.doi.org/10.1126/science.1250140

114. Mak, K.F., *et al.*, *Control of valley polarization in monolayer MoS2 by optical helicity.* Nature Nanotechnology. **7**(8): p. 494-498. 2012. http://dx.doi.org/10.1038/nnano.2012.96

115. Zeng, H., *et al.*, *Valley polarization in MoS2 monolayers by optical pumping.* Nature Nanotechnology. **7**(8): p. 490-493. 2012. http://dx.doi.org/10.1038/nnano.2012.95

116. Benameur, M.M., *et al.*, *Visibility of dichalcogenide nanolayers.* Nanotechnology. **22**(12): p. 125706-125706. 2011. http://dx.doi.org/10.1088/0957-4484/22/12/125706

117. Lee, C., *et al.*, *Anomalous lattice vibrations of single-and few-layer MoS2.* ACS Nano. **4**(5): p. 2695-700. 2010. http://dx.doi.org/10.1021/nn1003937

118. Li, H., *et al.*, *From bulk to monolayer MoS2: Evolution of Raman scattering.* Advanced Functional Materials. **22**(7): p. 1385-1390. 2012. http://dx.doi.org/10.1002/adfm.201102111

119. Mak, K.F., *et al.*, *Tightly bound trions in monolayer MoS2.* Nature Materials. **12**(3): p. 207-11. 2013. http://dx.doi.org/10.1038/nmat3505

120. Stewart, T.B. and P.D. Fleischauer, *Chemistry of sputtered molybdenum disulfide films.* Inorganic Chemistry. **21**(6): p. 2426-2431. 1982. http://dx.doi.org/10.1021/ic00136a060

121. Bichsel, R. and F. Levy, *Morphological and Compositional Properties of MoSe2 Films Prepared by R.F. Magnetron Sputtering.* Thin Solid Films. **116**(1): p. 367-372. 1984. http://dx.doi.org/10.1016/0040-6090(85)90031-8

122. Ellmer, K., *et al.*, *Deposition of c-oriented tungsten disulfide (WS2) films by reactive DC magnetron sputtering from a W-target in Ar/H2S.* Journal of Crystal Growth. **182**(3–4): p. 389-393. 1997. http://dx.doi.org/10.1016/S0022-0248(97)00355-2

123. Wu, S., *et al.*, *Vapor-Solid Growth of High Optical Quality MoS2 Monolayers with Near-Unity Valley Polarization.* ACS Nano. **7**(3): p. 2768-2772. 2013. http://dx.doi.org/10.1021/nn4002038

124. Liu, K.K., *et al.*, *Growth of large-area and highly crystalline MoS2 thin layers on insulating substrates.* Nano Letters. **12**(3): p. 1538-1544. 2012. http://dx.doi.org/10.1021/nl2043612

125. Yu, Y., *et al.*, *Controlled scalable synthesis of uniform, high-quality monolayer and few-layer MoS2 films.* Scientific Reports. **3**: p. 1866-1866. 2013. http://dx.doi.org/10.1038/srep01866

126. Ji, Q., *et al.*, *Chemical vapour deposition of group-VIB metal dichalcogenide monolayers: engineered substrates from amorphous to single crystalline.* Chemical Society Reviews. p. 2587-2602. 2015. http://dx.doi.org/10.1039/C4CS00258J

127. Lee, Y.H., *et al.*, *Synthesis of large-area MoS2 atomic layers with chemical vapor deposition.* Advanced Materials. **24**(17): p. 2320-2325. 2012. http://dx.doi.org/10.1002/adma.201104798

128. Najmaei, S., *et al.*, *Vapour phase growth and grain boundary structure of molybdenum disulphide atomic layers.* Nature Materials. **12**(8): p. 754-9. 2013. http://dx.doi.org/10.1038/nmat3673

129. Mann, J., *et al.*, *Facile growth of monolayer MoS2 film areas on SiO2.* European Physical Journal B. **86**(5): p. 2-5. 2013. http://dx.doi.org/10.1140/epjb/e2013-31011-y

130. van der Zande, A.M., *et al.*, *Grains and grain boundaries in highly crystalline monolayer molybdenum disulphide.* Nature Materials. **12**(6): p. 554-61. 2013. http://dx.doi.org/10.1038/nmat3633

131. Dumcenco, D., *et al.*, *Large-area MoS2 grown using H2S as the sulphur source.* 2D Materials. **2**(4): p. 044005-044005. 2015. http://dx.doi.org/10.1088/2053-1583/2/4/044005

132. Dumcenco, D., *et al.*, *Large-Area Epitaxial Monolayer MoS2.* ACS Nano. **10**(1021). 2015. http://dx.doi.org/10.1021/acsnano.5b01281

133. Baek, S.H., Y. Choi, and W. Choi, *Large-Area Growth of Uniform Single-Layer MoS2 Thin Films by Chemical Vapor Deposition.* Nanoscale Research Letters. **10**(1): p. 388-388. 2015. http://dx.doi.org/10.1186/s11671-015-1094-x

134. Plechinger, G., *et al.*, *A direct comparison of CVD-grown and exfoliated MoS2 using optical spectroscopy.* Physical Review Letters. **064008**(100): p. 1-7. 2013. http://dx.doi.org/10.1088/0268-1242/29/6/064008

135. V, K.K., *et al.*, *Predictive approach to CVD of crystalline layers of TMDs: The case of MoS2.* Nanoscale. **7**: p. 7802-7810. 2015. http://dx.doi.org/10.1039/C4NR07080A

136. Kang, K., *et al.*, *High-mobility three-atom-thick semiconducting films with wafer-scale homogeneity.* Nature. **520**(7549): p. 656-660. 2015. http://dx.doi.org/10.1038/nature14417

137. Jang, Y., *et al.*, *Wafer-scale, conformal and direct growth of MoS2 thin filmsby atomic layer deposition.* Applied Surface Science. **365**: p. 160-165. 2016. http://dx.doi.org/10.1016/j.apsusc.2016.01.038

138. Zhan, Y., *et al.*, *Large-area vapor-phase growth and characterization of MoS2 atomic layers on a SiO2 substrate.* Small. **8**(7): p. 966-971. 2012. http://dx.doi.org/10.1002/smll.201102654

139. Laskar, M.R., *et al.*, *Large Area Single Crystal (0001) Oriented MoS2 Thin Films.* Applied Physics Letters. **102**: p. 252108-252108. 2013. http://dx.doi.org/10.1063/1.4811410

140. Lee, Y., *et al.*, *Synthesis of wafer-scale uniform molybdenum disulfide films with control over the layer number using a gas phase sulfur precursor.* Nanoscale. **6**(5): p. 2821-6. 2014. http://dx.doi.org/10.1039/c3nr05993f

141. Gatensby, R., *et al.*, *Controlled synthesis of transition metal dichalcogenide thin films for electronic applications.* Applied Surface Science. **297**: p. 139-146. 2014. http://dx.doi.org/10.1016/j.apsusc.2014.01.103

142. Orofeo, C.M., *et al.*, *Scalable synthesis of layer-controlled WS2 and MoS2 sheets by sulfurization of thin metal films.* Applied Physics Letters. **105**: p. 083112-083112. 2014. http://dx.doi.org/10.1063/1.4893978

143. Liu, H., *et al.*, *Towards large area and continuous MoS2 atomic layers via vapor-phase growth: thermal vapor sulfurization.* Nanotechnology. **25**(40): p. 405702-405702. 2014. http://dx.doi.org/10.1088/0957-4484/25/40/405702

144. Lin, Y.-C., *et al.*, *Wafer-scale MoS2 thin layers prepared by MoO3 sulfurization.* Nanoscale. **4**(20): p. 6637-6637. 2012. http://dx.doi.org/10.1039/c2nr31833d

145. Wang, X., *et al.*, *Controlled Synthesis of Highly Crystalline MoS2 Flakes by Chemical Vapor Deposition.* Journal of the American Chemical Society. **135**: p. 5-8. 2013. http://dx.doi.org/10.1021/ja4013485

146. Han, G.H., *et al.*, *Seeded growth of highly crystalline molybdenum disulphide monolayers at controlled locations.* Nature Communications. **6**: p. 6128-6128. 2015. http://dx.doi.org/10.1038/ncomms7128

147. Sun, D., *et al.*, *Chemical vapor deposition growth of a periodic array of single-layer MoS2 islands via lithographic patterning of an SiO2/Si substrate.* 2D Materials. **2**(4): p. 045014-045014. 2015. http://dx.doi.org/10.1088/2053-1583/2/4/045014

148. Vogt, P., *et al.*, *Silicene: Compelling Experimental Evidence for Graphenelike Two-Dimensional Silicon.* Physical Review Letters. **108**(15): p. 155501-155501. 2012. http://dx.doi.org/10.1103/PhysRevLett.108.155501

149. Acun, A., *et al.*, *Germanene: the germanium analogue of graphene.* Journal of Physics: Condensed Matter. **27**(44): p. 443002-443002. 2015. http://dx.doi.org/10.1088/0953-8984/27/44/443002

150. Tao, L., *et al.*, *Silicene field-effect transistors operating at room temperature.* Nature Nanotechnology. **10**(3): p. 227-231. 2015. http://dx.doi.org/10.1038/nnano.2014.325

151. Kara, A., *et al.*, *A review on silicene - New candidate for electronics.* Surface Science Reports. **67**(1): p. 1-18. 2012. http://dx.doi.org/10.1016/j.surfrep.2011.10.001

152. Dávila, M.E. and G. Le Lay, *Few layer epitaxial germanene: a novel two-dimensional Dirac material.* Scientific Reports. **6**(August 2015): p. 20714-20714. 2016. http://dx.doi.org/10.1038/srep20714

153. Dávila, M.E., *et al.*, *Germanene: A novel two-dimensional germanium allotrope akin to graphene and silicene.* New Journal of Physics. **16**: p. 095002-095002. 2014. http://dx.doi.org/10.1088/1367-2630/16/9/095002

154. Zhu, F.-F., *et al.*, *Epitaxial growth of two-dimensional stanene.* Nature Materials. **14**: p. 1020-1025. 2015. http://dx.doi.org/10.1038/NMAT4384

155. Bianco, E., *et al.*, *Stability and Exfoliation of Germanane: A Germanium Graphane Analogue.* ACS Nano. **7**(5): p. 4414-4421. 2013. http://dx.doi.org/10.1021/nn4009406

156. Jiang, S., *et al.*, *Improving the stability and optical properties of germanane via one-step covalent methyl-termination.* Nature Communications. **5**: p. 3389-3389. 2014. http://dx.doi.org/10.1038/ncomms4389

157. Arguilla, M.Q., *et al.*, *Synthesis and Stability of Two-Dimensional Ge/Sn Graphane Alloys.* Chemistry of Materials. **26**: p. 6941-6946. 2014. http://dx.doi.org/10.1021/cm502755q

158. Jiang, S., *et al.*, *Covalently-controlled properties by design in group IV graphane analogues.* Accounts of Chemical Research. **48**(1): p. 144-151. 2015. http://dx.doi.org/10.1021/ar500296e

159. Xu, Y., *et al.*, *Large-Gap Quantum Spin Hall Insulators in Tin Films.* Physical Review Letters. **111**(13): p. 136804-136804. 2013. http://dx.doi.org/10.1103/PhysRevLett.111.136804

160. Liu, C.C., W. Feng, and Y. Yao, *Quantum spin Hall effect in silicene and two-dimensional germanium.* Physical Review Letters. **107**(7): p. 1-4. 2011. http://dx.doi.org/10.1103/PhysRevLett.107.076802

161. Restrepo, O.D., *et al.*, *Tunable gaps and enhanced mobilities in strain-engineered silicane.* Journal of Applied Physics. **115**(3). 2014. http://dx.doi.org/10.1063/1.4860988

162. Pinchuk, I.V., *et al.*, *Epitaxial co-deposition growth of CaGe2 films by molecular beam epitaxy for large area germanane.* Journal of Materials Research. **29**(03): p. 410-416. 2014. http://dx.doi.org/10.1557/jmr.2014.2

163. Vogg, G., *et al.*, *Epitaxial alloy films of Zintl-phase Ca(Si1−xGex)2.* Journal of Crystal Growth. **223**(4): p. 573-576. 2001. http://dx.doi.org/10.1016/S0022-0248(01)00686-8

164. Slotman, G.J. and A. Fasolino, *Structure, stability and defects of single layer hexagonal BN in comparison to graphene.* Journal of Physics: Condensed Matter. **25**(4): p. 045009-045009. 2013. http://dx.doi.org/10.1088/0953-8984/25/4/045009

165. Song, L., *et al.*, *Large scale growth and characterization of atomic hexagonal boron nitride layers.* Nano Letters. **10**(8): p. 3209-3215. 2010. http://dx.doi.org/10.1021/nl1022139

166. Liu, H., *et al.*, *Phosphorene : An Unexplored 2D Semiconductor with a High Hole Mobility.* ACS Nano. **8**(4): p. 4033-4041. 2014. http://dx.doi.org/10.1021/nn501226z

167. Li, L., *et al.*, *Black phosphorus field-effect transistors.* Nature Nanotechnology. **9**(5): p. 1-17. 2014. http://dx.doi.org/10.1038/nnano.2014.35

168. Kim, J.-S., *et al.*, *Toward air-stable multilayer phosphorene thin-films and transistors.* Scientific Reports. **5**: p. 8989-8989. 2015. http://dx.doi.org/10.1038/srep08989

169. Kou, L., C. Chen, and S.C. Smith, *Phosphorene: Fabrication, Properties, and Applications.* The Journal of Physical Chemistry Letters. **6**(14): p. 2794-2805. 2015. http://dx.doi.org/10.1021/acs.jpclett.5b01094

170. Geim, A.K. and I.V. Grigorieva, *Van der Waals heterostructures.* Nature. **499**(7459): p. 419-25. 2013. http://dx.doi.org/10.1038/nature12385

171. Niu, T. and A. Li, *From two-dimensional materials to heterostructures.* Progress in Surface Science. **90**(1): p. 21-45. 2015. http://dx.doi.org/10.1016/j.progsurf.2014.11.001

172. Lotsch, B.V., *Vertical 2D Heterostructures.* Annual Review of Materials Research. **45**(1): p. 85-109. 2015. http://dx.doi.org/10.1146/annurev-matsci-070214-020934

173. Lee, C.-H.*, et al.*, *Atomically thin p–n junctions with van der Waals heterointerfaces.* Nature Nanotechnology. **9**(9): p. 676-681. 2014. http://dx.doi.org/10.1038/nnano.2014.150

174. Young, J.R.*, et al.*, *Water activated doping and transport in multilayered germanane crystals.* Journal of Physics: Condensed Matter. **28**: p. 34001-34001. 2016. http://dx.doi.org/10.1088/0953-8984/28/3/034001

175. Frindt, R.F., *Superconductivity in Ultrathin NbSe2 Layers.* Physical Review Letters. **28**(5): p. 299-301. 1972. http://dx.doi.org/10.1103/PhysRevLett.28.299

176. Frindt, R.F., *Single Crystals of MoS2 Several Molecular Layers Thick.* Journal of Applied Physics. **37**(4): p. 1928-1929. 1966. http://dx.doi.org/10.1063/1.1708627

177. Allen, M.J., V.C. Tung, and R.B. Kaner, *Honeycomb carbon: a review of graphene.* Chemical Reviews. **110**(1): p. 132-145. 2009. http://dx.doi.org/10.1021/cr900070d

178. Gong, Y.*, et al.*, *Vertical and in-plane heterostructures from WS2/MoS2 monolayers.* Nature Materials. **13**(12): p. 1135-1142. 2014. http://dx.doi.org/10.1038/nmat4091

179. Eda, G. and S.A. Maier, *Two-Dimensional Crystals: Managing Light for Optoelectronics.* ACS Nano. **7**(7): p. 5660-5665. 2013. http://dx.doi.org/10.1021/nn403159y

180. Voiry, D.*, et al.*, *Covalent functionalization of monolayered transition metal dichalcogenides by phase engineering.* Nature Chemistry. **7**(1): p. 45-49. 2015. http://dx.doi.org/10.1038/nchem.2108

181. Vogg, G., M. Brandt, and M. Stutzmann, *Polygermyne—a prototype system for layered germanium polymers.* Advanced Materials. **12**(17): p. 1278-1281. 2000. http://dx.doi.org/10.1002/1521-4095(200009)12:17<1278::AID-ADMA1278>3.0.CO;2-Y

182. Edman, L.*, et al.*, *Electrical resistivity of single-crystal graphite under pressure: An anisotropic three-dimensional semimetal.* Physical Review B. **57**(11): p. 6227-6230. 1998. http://dx.doi.org/10.1103/PhysRevB.57.6227

183. Brandt, M., T. Puchert, and M. Stutzmann, *Electronic transport in crystalline siloxene.* Solid State Communications. **102**(5): p. 365-368. 1997. http://dx.doi.org/10.1016/S0038-1098(97)00010-0

184. Baugher, B.W.H.*, et al.*, *Intrinsic electronic transport properties of high-quality monolayer and bilayer MoS2.* Nano Letters. **13**(9): p. 4212-4216. 2013. http://dx.doi.org/10.1021/nl401916s

185. Dresselhaus, M.S. and G. Dresselhaus, *Intercalation compounds of graphite.* Advances in Physics. **30**(2): p. 139-326. 1981. http://dx.doi.org/10.1080/00018738100101367

186. Maier, F.*, et al.*, *Origin of Surface Conductivity in Diamond.* Physical Review Letters. **85**(16): p. 3472-3475. 2000. http://dx.doi.org/10.1103/PhysRevLett.85.3472

187. Amamou, W., *et al.*, *Large area epitaxial germanane for electronic devices.* 2D Materials. **2**: p. 035012-035012. 2015. http://dx.doi.org/10.1088/2053-1583/2/3/035012

188. Qian, X., *et al.*, *Quantum spin Hall effect in two- dimensional transition metal dichalcogenides.* Science express. **10**(November): p. 1126-1126. 2014. http://dx.doi.org/10.1126/science.1256815

189. Wang, F., *et al.*, *Ionic Liquid Gating of Suspended MoS2 Field Effect Transistor Devices.* Nano Letters. **15**(8): p. 5284-5288. 2015. http://dx.doi.org/10.1021/acs.nanolett.5b01610

190. Presolski, S. and M. Pumera, *Covalent functionalization of MoS2.* Materials Today. **19**(3): p. 140-145. 2016. http://dx.doi.org/10.1016/j.mattod.2015.08.019

191. Sarkar, D., *et al.*, *Functionalization of Transition Metal Dichalcogenides with Metallic Nanoparticles: Implications for Doping and Gas-Sensing.* Nano Letters. **15**(5): p. 2852-2862. 2015. http://dx.doi.org/10.1021/nl504454u

192. Vazquez-Mena, O., *et al.*, *Resistless nanofabrication by stencil lithography: A review.* Microelectronic Engineering. **132**: p. 236-254. 2015. http://dx.doi.org/10.1016/j.mee.2014.08.003

193. Scheuschner, N., *et al.*, *Photoluminescence of freestanding single- and few-layer MoS2.* Physical Review B - Condensed Matter and Materials Physics. **89**(12): p. 2-7. 2014. http://dx.doi.org/10.1103/PhysRevB.89.125406

194. Feng, Y., *et al.*, *Synthesis of Large-Area Highly Crystalline Monolayer Molybdenum Disulfide with Tunable Grain Size in a H2 Atmosphere.* ACS Applied Materials and Interfaces. **7**(40): p. 22587-22593. 2015. http://dx.doi.org/10.1021/acsami.5b07038

195. Yoshimoto, M., *et al.*, *Atomic-scale formation of ultrasmooth surfaces on sapphire substrates for high-quality thin-film fabrication.* Applied Physics Letters. **67**(18): p. 2615-2617. 1995. http://dx.doi.org/10.1063/1.114313

196. Li, X., *et al.*, *Role of hydrogen in chemical vapor deposition growth of MoS2 atomic layers.* Nanoscale. p. 8398-8404. 2015. http://dx.doi.org/10.1039/C5NR00904A

197. Ji, Q., *et al.*, *Epitaxial Monolayer MoS2 with Novel Photoluminescence.* Nano Letters. **13**(8): p. 130730131307000-130730131307000. 2013. http://dx.doi.org/10.1021/nl401938t

198. Islam, M.R., *et al.*, *Tuning the electrical property via defect engineering of single layer MoS2 by oxygen plasma.* Nanoscale. **6**(17): p. 10033-9. 2014. http://dx.doi.org/10.1039/c4nr02142h

199. Chakraborty, B., *et al.*, *Symmetry-dependent phonon renormalization in monolayer MoS2 transistor.* Physical Review B. **85**(16): p. 2-5. 2012. http://dx.doi.org/10.1103/PhysRevB.85.161403

200. Zhang, H., L.-M. Liu, and W.-M. Lau, *Dimension-dependent phase transition and magnetic properties of VS2.* Journal of Materials Chemistry A. **1**(36): p. 10821-10821. 2013. http://dx.doi.org/10.1039/c3ta12098h

201. Zhuang, H.L. and R.G. Hennig, *Stability and magnetism of strongly correlated single-layer VS2.* Physical Review B. **93**(5): p. 054429-054429. 2016. http://dx.doi.org/10.1103/PhysRevB.93.054429

202. Xu, K., *et al.*, *Ultrathin nanosheets of vanadium diselenide: A metallic two-dimensional material with ferromagnetic charge-density-wave behavior.* Angewandte Chemie - International Edition. **52**(40): p. 10477-10481. 2013. http://dx.doi.org/10.1002/anie.201304337

203. Girard, P., *Electrostatic force microscopy: principles and some applications to semiconductors.* Nanotechnology. **12**(4): p. 485-490. 2001. http://dx.doi.org/10.1088/0957-4484/12/4/321

204. Yu, Y.-J., *et al.*, *Tuning the Graphene Work Function by Electric Field Effect.* Nano Letters. **9**(10): p. 3430-3434. 2009. http://dx.doi.org/10.1021/nl901572a

205. Li, G., A. Luican, and E.Y. Andrei, *Self-navigation of a scanning tunneling microscope tip toward a micron-sized graphene sample.* Review of Scientific Instruments. **82**(7): p. 0-5. 2011. http://dx.doi.org/10.1063/1.3605664

206. Topinka, M.A., *et al.*, *Imaging Coherent Electron Flow from a Quantum Point Contact.* Science. **289**(5488): p. 2323-2326. 2000. http://dx.doi.org/10.1126/science.289.5488.2323

207. Berezovsky, J., *et al.*, *Imaging coherent transport in graphene. Part I: mapping universal conductance fluctuations.* Nanotechnology. **21**(27): p. 274013-274013. 2010. http://dx.doi.org/10.1088/0957-4484/21/27/274013

208. Topinka, M.A., *et al.*, *Coherent branched flow in a two-dimensional electron gas.* Nature. **410**(6825): p. 183-186. 2001. http://dx.doi.org/10.1038/35065553

209. Panchal, V., *et al.*, *Magnetic Scanning Probe Calibration Using Graphene Hall Sensor.* IEEE Transactions on Magnetics. **49**(7): p. 3520-3523. 2013. http://dx.doi.org/10.1109/TMAG.2013.2243127

210. Bhallamudi, V.P., *et al.*, *Imaging spin properties using spatially varying magnetic fields.* Journal of Applied Physics. **111**(1): p. 1-5. 2012. http://dx.doi.org/10.1063/1.3673259

211. Bhallamudi, V.P., *et al.*, *Experimental demonstration of scanned spin-precession microscopy.* Physical Review Letters. **111**(11): p. 1-5. 2013. http://dx.doi.org/10.1103/PhysRevLett.111.117201

212. Boukhvalov, D.W. and M.I. Katsnelson, *Chemical functionalization of graphene.* Journal of Physics: Condensed Matter. **21**(34): p. 344205-344205. 2009. http://dx.doi.org/10.1088/0953-8984/21/34/344205

213. Wang, B., Y.S. Puzyrev, and S.T. Pantelides, *Enhanced chemical reactions of oxygen at grain boundaries in polycrystalline graphene.* Polyhedron. **64**: p. 158-162. 2013. http://dx.doi.org/10.1016/j.poly.2013.03.032

214. Balog, R., *et al.*, *Bandgap opening in graphene induced by patterned hydrogen adsorption.* Nature Materials. **9**(4): p. 315-319. 2010. http://dx.doi.org/10.1038/nmat2710

215. Wang, H., *et al.*, *Doping monolayer graphene with single atom substitutions.* Nano Letters. **12**(1): p. 141-144. 2012. http://dx.doi.org/10.1021/nl2031629

216. Pantelides, S.T., *et al.*, *Defects and doping and their role in functionalizing graphene.* MRS Bulletin. **37**(12): p. 1187-1194. 2012. http://dx.doi.org/10.1557/mrs.2012.187

217. Bangert, U. and R. Zan, *Electronic functionalisation of graphene via external doping and dosing.* International Material Reviews. **60**(3): p. 133-149. 2015. http://dx.doi.org/10.1179/1743280414Y.0000000047

218. Vicarelli, L.*, et al.*, *Controlling defects in graphene for optimizing the electrical properties of graphene nanodevices.* ACS Nano. **9**(4): p. 3428-3435. 2015. http://dx.doi.org/10.1021/acsnano.5b01762

219. Peres, N.M.R., F. Guinea, and A.H. Castro Neto, *Electronic properties of disordered two-dimensional carbon.* Physical Review B. **73**(12): p. 1-23. 2006. http://dx.doi.org/10.1103/PhysRevB.73.125411

220. Lherbier, A.*, et al.*, *Charge Transport in Chemically Doped 2D Graphene.* Physical Review Letters. **101**(3): p. 036808-036808. 2008. http://dx.doi.org/10.1103/PhysRevLett.101.036808

221. Tsetseris, L., B. Wang, and S.T. Pantelides, *Substitutional doping of graphene: The role of carbon divacancies.* Physical Review B. **89**(3): p. 3-6. 2014. http://dx.doi.org/10.1103/PhysRevB.89.035411

222. Ugeda, M.M.*, et al.*, *Electronic and structural characterization of divacancies in irradiated graphene.* Physical Review B. **85**(12): p. 2-6. 2012. http://dx.doi.org/10.1103/PhysRevB.85.121402

223. Wei, D.*, et al.*, *Synthesis of N-doped graphene by chemical vapor deposition and its electrical properties.* Nano Letters. **9**(5): p. 1752-8. 2009. http://dx.doi.org/10.1021/nl803279t

224. Guo, B.*, et al.*, *Controllable N-Doping of Graphene.* Nano Letters. p. 4975-4980. 2010. http://dx.doi.org/10.1021/nl103079j

225. Zhao, L.*, et al.*, *Visualizing Individual Nitrogen Dopants in Monolayer Graphene.* Science. **333**: p. 999-1003. 2011. http://dx.doi.org/10.1007/s13398-014-0173-7.2

226. Zhao, L.*, et al.*, *Local atomic and electronic structure of boron chemical doping in monolayer graphene.* Nano Letters. **13**(10): p. 4659-4665. 2013. http://dx.doi.org/10.1021/nl401781d

227. Tison, Y.*, et al.*, *Electronic interaction between nitrogen atoms in doped graphene.* ACS Nano. **9**(1): p. 670-678. 2015. http://dx.doi.org/10.1021/nn506074u

228. Yazyev, O.V. and L. Helm, *Defect-induced magnetism in graphene.* Physical Review B. **75**(12): p. 1-5. 2007. http://dx.doi.org/10.1103/PhysRevB.75.125408

229. Ugeda, M.M.*, et al.*, *Missing atom as a source of carbon magnetism.* Physical Review Letters. **104**(9): p. 1-4. 2010. http://dx.doi.org/10.1103/PhysRevLett.104.096804

230. Nair, R.R.*, et al.*, *Spin-half paramagnetism in graphene induced by point defects.* Nature Physics. **8**(3): p. 199-202. 2012. http://dx.doi.org/10.1038/nphys2183

231. González-Herrero, H.*, et al.*, *Atomic-scale control of graphene magnetism by using hydrogen atoms.* Science. **352**(6284): p. 437-441. 2016. http://dx.doi.org/10.1126/science.aad8038

232. Luican, A., G. Li, and E.Y. Andrei, *Scanning tunneling microscopy and spectroscopy of graphene layers on graphite.* Solid State Communications. **149**(27-28): p. 1151-1156. 2009. http://dx.doi.org/10.1016/j.ssc.2009.02.059

233. Stolyarova, E.*, et al.*, *High-resolution scanning tunneling microscopy imaging of mesoscopic graphene sheets on an insulating surface.* Proceedings of the National Academy of Sciences of the United States of America. **104**(22): p. 9209-9212. 2007. http://dx.doi.org/10.1073/pnas.0703337104

234. Hollen, S.M.*, et al.*, *Modification of electronic surface states by graphene islands on Cu(111).* Physical Review B. **91**(19): p. 30-35. 2015. http://dx.doi.org/10.1103/PhysRevB.91.195425

235. Hollen, S.M.*, et al.*, *Native defects in ultra-high vacuum grown graphene islands on Cu(1 1 1).* Journal of Physics. Condensed Matter. **28**(3): p. 034003-034003. 2016. http://dx.doi.org/10.1088/0953-8984/28/3/034003

236. Zhang, Y.*, et al.*, *Giant phonon-induced conductance in scanning tunnelling spectroscopy of gate-tunable graphene.* Nature Physics. **4**(8): p. 627-630. 2008. http://dx.doi.org/10.1038/nphys1022

Appendix A: Device Fabrication

In this appendix, we provide the detailed fabrication process for production of Hall bar style graphene devices. These devices are fabricated from CVD grown graphene sheets which have been transferred to SiO_2 substrates. Additionally, we discuss the method employed to synthesize magneto-transport devices around exfoliated flakes and the development of electron beam lithography (EBL) defined resolution limited electrodes.

A.1 Materials and Systems

Prior to describing the various processes involved in these device fabrication procedures, we provide the specific details of the supplies and systems involved, as well as some of the standard operating procedures used with them. Unless specifically mentioned in the process description the standard procedures below are used.

A.1.1 *Resists*

- **PMMA** – Poly(methyl methacrylate) is a positive resist purchased from MicroChem Corp. The type of PMMA used for these process is **950 PMMA A4** (product# M230004 0500L1GL). This is drop cast onto substrates using a glass

pipet (never use plastic), and consequently spun on and baked using the following parameters, resulting in a **170 nm thick** film:

- Spin Speed: 6 000 RPM
- Acceleration: 10 000 RPM/sec
- Time: 60 seconds
- Bake Temperature: 180 °C
- Bake Time: 5 min.

- **Copolymer** – Organic resist is used for bi-layer synthesis in combination with PMMA to create an under-cut during the lithographic process (due to its increased sensitivity to electron exposure), easing lift-off of deposited metals. This is purchased from MicroChem Corp. The type of copolymer used in these processes is **MMA (8.5) MAA EL 11** (product # M310011 0500L1GL). This is drop cast onto substrates using a glass pipet (never use plastic), and consequently spun on and baked using the following parameters, resulting in a **540 nm thick** film:

  - Spin Speed: 3 000 RPM
  - Acceleration: 10 000 RPM/sec
  - Time: 75 seconds
  - Bake Temperature: 150 °C
  - Bake Time: 2 min.

- **HSQ** - Hydrogen silsesquioxane, is a high resolution, negative electron beam resist, but is also sensitive to certain wavelengths of light (though from my experience, this seems to be a slow process with ambient/building light). Because of this, the

resist is kept covered from light (in the bottle, and once deposited on samples, typically by Al foil), except for the few seconds while it is being loaded and unloaded from the scanning electron microscope. This resist is obtained in small volumes (3-5 mL) from Nanotech West (specifically Aimee Price). It's purchased in larger quantities there from Dow Corning (**XR 1541-004**), and is 4% solids in MIBK. This resist is extremely sensitive to solvents, bases, and water. If exposed to any of these, it has a tendency to "gel" up, and become useless. This is one of the reasons it is decanted into very small volumes. It is drop cast onto substrates using a plastic syringe (never use glass), and consequently spun on and baked using the following parameters, resulting in a **60 nm thick** film:

- Spin Speed: 3 000 RPM
- Acceleration: 10 000 RPM/sec
- Time: 75 seconds
- 1st Bake Temperature: 120 °C
- 1st Bake Time: 2 min
- 2nd Bake Temperature: 200 °C
- 2st Bake Time: 3 min

Notes on resist handling: Resists are typically very sensitive to possible contaminants and can also degrade over time. To help avoid both of these potential pitfalls, certain protocols are followed when dealing with them.

1. Resists are usually purchased in larger volumes (500 mL) and decanted into smaller volume containers (5-25 mL)

2. For the larger volume containers, resist is only ever poured from this bottle into smaller bottles. Nothing is ever inserted into these containers in order to prevent contamination.
3. For the smaller bottles, a clean / new pipet or syringe is only inserted into the bottle to remove resist one time. If more resist is needed, a new pipet or syringe is used.
4. The caps are removed from the bottles for a minimal amount of time, only ever in a chemical hood, in an effort to prevent dust from entering the bottles.
5. Both the large or small bottles are kept refrigerated, in order to slow any potential degradation.
6. When removed from refrigerator, the resist bottles are warmed up to room temperature (15-30 minutes for small bottles, 1-3 hours for large bottles) before opening, to prevent the condensation of water on the inside of the bottle and an inrush of outside air due to pressure differences.
7. Bottles of resist (as well as other chemicals) should **never** be used after the expiration date even if refrigerated. The degradation of resists can be a slow process and can cause a process to stop working successfully in odd ways that are difficult to track back to the origin.
8. As a rule of thumb, small decanted bottles of resist should only be used for around 1 month (if used regularly) as they have a tendency to become contaminated due to regular opening and closing.

A.1.2 *Developers*

- **MIBK –** Methyl isobutyl ketone is an organic solvent, used as the active ingredient for the development of PMMA/Copolymer resists. Typically MIBK is mixed with isopropanol (IPA) in the ratio 1:3 (MIBK:IPA). While the development time is a synthesis parameter that can be manipulated, we typically hold this parameter

constant while adjusting the lithographic writing parameters to achieve desired results (for thicker resist stacks, this may not be possible). In all processes described here, the development time used is **45 seconds.**

- **MF-319 –** A base developer from Microposit with TMAH (Tetramethylammonium hydroxide: 2.45%) as the active ingredient. Used to develop many photoresists, for our work, we use this to develop HSQ resist, for a time of **2 minutes**.

A.1.3 *Device Synthesis Systems*

- **EBL –** Electron beam lithography is performed on FEI Helios Nanolab 600 dual beam focused ion beam (FIB)/scanning electron microscope (SEM), maintained by the NanoSystems Laboratory user facility at The Ohio State University. The writing process is carried out by the Nanometer Pattern Generation System (NPGS) software, developed by JC Nabity Lithography Systems.

- **Metal Deposition –** The metal depositions for our nano-lithography is performed in a Kurt J. Lesker Lab-18 thin film deposition system, using electron beam deposition. This system is again owned and maintained by Nanosystems Laboratory. Deposition rates and thickness are monitored by a quartz crystal monitor. Typical deposition rates are between **0.5-1 Å/sec.**

- **RIE –** Reactive ion etch. This is used in our process to etch PMMA and graphene using an Oxygen plasma. This low-damage inductively coupled plasma reactive ion etching (ICP-RIE) using a Plasma Therm SLR770 tool located at the Nanotech

West Laboratory at The Ohio State University. A Si wafer is used as a process wafer, and we do not use any pump oil (sometimes placed between sample and holder to improve etch reliability) in our process. We use the following etching parameters for this process to achieve a PMMA etch rate of **4.4 nm/sec.**

- RF1 (DCV) Voltage: 25 V
- RF2 Voltage: 200 V
- Gas Flow: 20 sccm O_2
- System Pressure: 5 mTorr
- System Temperature: 19 °C
- He Pressure: 5 mTorr

A.2 CVD Graphene Device Fabrication

Electronic devices (primarily Hall bar geometry) are synthesized through a two-step lithography process. In the first step, Ti/Au electrodes are deposited in a contact pattern on top of the graphene sheet, while in the second the graphene hall bar is defined and the remaining graphene is etched away. We provided the detailed instructions for this process here. This process is shown schematically in **Figure A.1.**

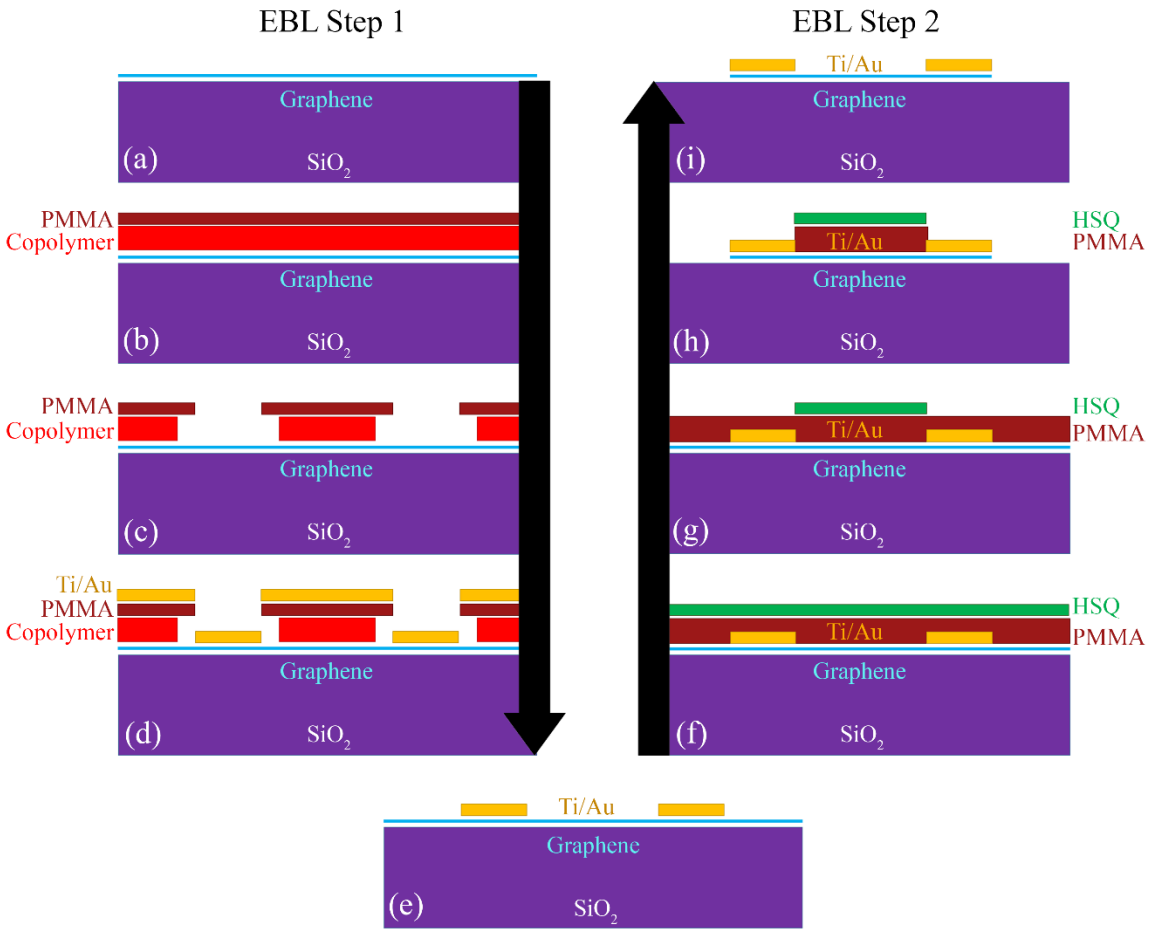

Figure A.1 *Graphene EBL Process*

Schematic of full lithography process. (a) Start with Graphene/SiO_2/Si sample. (b) Spin on and bake PMMA/Copolymer resists. (c) Perform contact pattern EBL and develop. (d) Deposit Ti/Au metal stack. (e) Lift-off resist/metal in hot acetone. (f) Deposit and bake HSQ/PMMA resists. (g) Perform graphene plateau EBL and develop HSQ. (h) Oxygen plasma etch through exposed PMMA/Graphene. (i) lift-off remaining HSQ/PMMA resists.

A.2.1 *Wafer Cleaving.*

The CVD graphene is purchased through Graphene Supermarket (graphene-supermarket.com), though in the future we intend to use graphene synthesized and transferred at The Ohio State University by the Graphene Factory. The CVD graphene is pre-transferred to SiO_2(285nm)/p-type SiO_2 wafers, and is roughly 1 mm^2 in size. These

samples are cleaved into four smaller samples (5 × 5 mm, providing 4 different samples to work with). The graphene is easily damaged by dust and scratching, so before cleaving it is coated with PMMA via spin coater, and baked. The samples are cleaved using a diamond scribe to scratch the PMMA/Graphene side of the wafer (i.e. the wafer is right-side-up). Scratches of less than 1 mm are made at the end points of the cleave line. The wafer is set on the edge of a glass slide, with the edge of the slide under the cleave locations (to act as a fulcrum), and the corners of the two sides are gently pressed with tweezers to cleave the substrate. This is repeated as needed. Subsequently the PMMA is removed from the sample by soaking in acetone for 30 minutes, followed by a rinse in Isopropanol and dried under N_2.

A.2.2 *First Lithographic Step*

Resist deposition and preparation. In this first step, we define the metallic electrical contacts on the graphene. First, the graphene sample is coated with a Copolymer (3 000 RPM, 10 000 RPM/sec, 75 sec, 150 °C bake for 2 min) and PMMA (6 000 RPM, 10 000 RPM/sec, 60 sec, 180 °C bake for 5 min.), and small scratches are made along the very lower edge of the sample, as well as in the corners for orientation, and SEM focusing. Using a 1 mL plastic syringe, a very small drop of 100 nm Au colloids (suspended in water) is placed in each the scratched corners. This leaves small bubbles of liquid in the four corners of the sample. These are removed by gently touching a Kimwipe to the bubble, which will wick the liquid of the substrate (leaving a large number of the Au colloids).

Great care should be taken during this step to keep this liquid only in the corners of the substrate, and not to touch or scratch the center of the resist covered sample.

SEM alignment and writing. The sample is loaded into the SEM with the edge scratch located along the bottom edge of the sample (as viewed in the SEM). Using standard SEM techniques, the sample should be raised to the working distance of 4.1 mm and focused on one of the corners (using the spherical Au colloids). Using the XT-align feature of the SEM, the bottom edge of the sample should be oriented along the x-axis (same edge as the long scratch). The lower left corner of the sample is assigned the location of (0, 0). With this completed the sample is now a well-defined coordinate grid, with an origin (lower left corner), and x- and y-axes (defined by the lower edge of the sample). **It is critical to note the exact points used to perform the XT-alignment, and the origin point.** Since this is a two-step write process, the same points will need to be located in the second step, to align to the first-layer write performed. Using the XY-focus feature of the NPGS EBL software (located as the button "Direct Stage Control" on the left of the main NPGS screen), the focus at the four corner scratches (focused using the Au colloids) should be recorded, setting a focal plane of the sample for writing. This XY-plane focus will allow the writing software to take into account any difference in the sample height as the sample is moved between write fields.

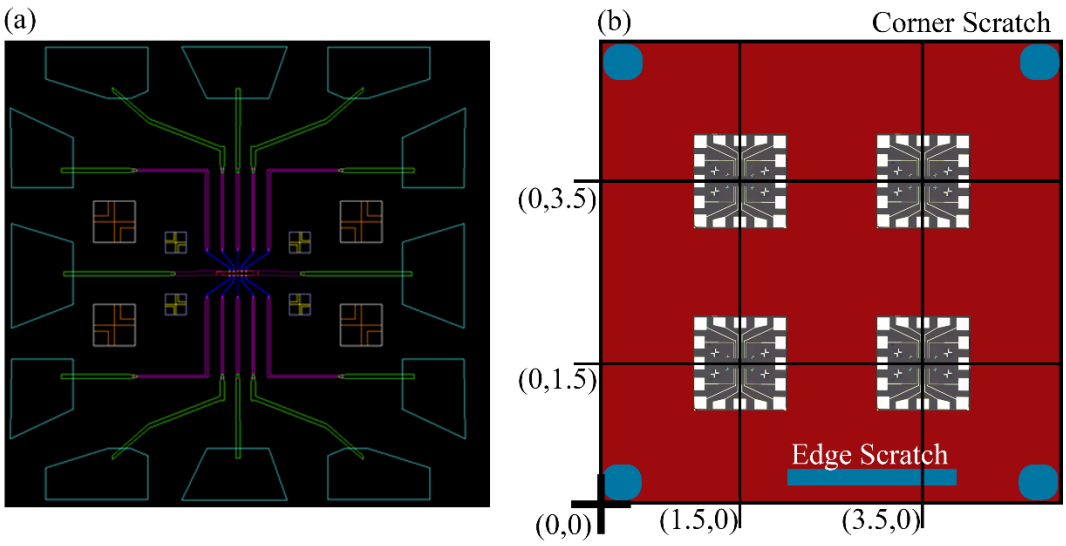

Figure A.2 *Graphene Device Schematic.*

(a) Standard Hall bar design, with different colors representing different currents and layers (write field width is 1.1 mm). (b) Layout of a typical graphene sample. Blue areas in the corner show the corner scratches where the Au colloids are deposited. The blue rectangle along the bottom edge is to allow for correct orientation of the sample in the SEM. The coordinate plane is arranged assigning the bottom edge as the x-axis, and the bottom left corner as the origin. Typically, four devices (~1.1 mm^2) are written on a sample. Locations are shown with units of mm.

Table A.1 *First EBL write parameters.*

Design Layer	Feature Color	Field Size[1]	Offset[2]	Mag.[3]	Spacing[4]	Config. Param.	Measured Current	Dose[5]
3	Blue	0.25	(0, 0)	500	8.85	-5	86	160
4	Purple	0.6	(6, -6)	200	22.13	-4	170	160
4	Yellow	0.6	(6, -6)	200	22.13	-4	170	160
5	Green	1.2	(16.5, -16.5)	100	44.25	-3	340	180
5	Orange	1.2	(16.5, -16.5)	100	44.25	-3	340	180
6	Light Blue	1.2	(16.5, -16.5)	100	44.25	0	340	200

The standard write pattern is shown in **Figure A.2**(a) (Files with "HallBar" in the name, there are several different slight variations). This ~1 mm^2 pattern is written (typically) in

[1] In mm (approximate)
[2] In μm
[3] Magnification
[4] Center to Center spacing, and Lines spacing, usually the same value
[5] Area Dose, in μC/cm^2

four locations on the substrate[6], shown schematically in **Figure A.2**(b). There are several different layers, defined by the magnification and current used in that layer. Different colored features in the same layer can have different dosing values. The larger the magnification factor, the higher resolution of the features (i.e. smaller features). The current and dosing for writing the different layers and features is different. All of these features (specified by layer and color used in the schematic) and their writing parameters are shown in **Table A.1.** One thing to note is the layer offset specified. This offset is a result of the changing current and magnification between the layers[7]. My personal experience has been that once determined, these offsets do not change noticeably over time. Additionally, the configuration parameter is what controls the SEM aperture (and hence the real current). This value is an integer and should correspond to the correct "Measured Current." These values are zero indexed at 2 700 pA current, and decrease or increase at intervals of ±1 as the current is increased or decreased. For example a current of 43 pA would have a configuration value of -6. The dosing values provides have been calibrated for this specific write. If current, spacing, voltage, magnification, resist, or feature size changes, the dosing will need to be recalculated. Finally, to write correctly the run file must have the "Disable XY Focus Control" and "Disable Automatic Control" settings toggled to the "no" value (yes, this is a double negative).

[6] I suggest using the "relative" location feature on the SEM software to move between write locations. This way, only the distance in location between the writes (and initially from the origin) need to be known.

[7] The layer offset is calibrated for this specific pattern (or layer write parameters). For other patterns or write parameters, these values will need to be determined. The recommended process for this is to write and develop the full pattern using no offsets, then to use an optical microscope to determine the offset that needs to be applied to correct the misalignment of the layers

Sample Development. After the writing is complete, the sample is developed in MIBK/IPA (1:3 ratio) for 45 seconds, and consequently rinsed in IPA for 30 seconds, and gently running deionized water (DI H_2O) for 15 seconds. While the development time of 45 seconds is suggested, if (after looking at sample under microscope), the sample did not develop completely, or there is obvious residue, additional development steps in 10 second increments may help. Overdevelopment can occur, but on this Hall bar pattern with a minimum feature size of 1 μm, this is unlikely.

Metal Deposition and Lift-off. Subsequently, metal is deposited onto the substrate. The typical metal stack used is Ti seeding layer (1 nm, 0.5 Å/sec) followed by Au (50-100 nm, 1-1.5 Å/sec). After metallization, the resist layers are lifted off in hot acetone (75 °C), with the hot acetone beaker sitting in a water bath for more uniform heating. Additionally, a watch-glass is placed over top of the hot acetone to prevent it from evaporating entirely. Lift-off is performed for 3-5 hours. After this time, the samples may need to be lightly agitated with a glass pipette, while still submerged, to remove any resist/metal still lightly stuck to the surface. It is extremely important that the sample not be removed from the acetone until all of the extra metal is removed from the surface. If the sample dries with unwanted metal still present on the surface, this metal will almost certainly be stuck permanently to the surface. After lift-off is complete, the sample should be rinsed in cold acetone, IPA, and dried with N_2 gun.

A.2.3 *Second Lithographic Step*

Resist deposition and preparation. In this second lithographic step, we define the graphene plateau. Much of this second lithographic step is similar to the first step. However, we begin by depositing a different resist stack. In this case we deposit a PMMA sacrificial layer—by which I mean, it's there only to protect the underlying graphene and does not play any part in the patterning process—spun and baked using the same parameters as before (6 000 RPM, 10 000 RPM/sec, 60 sec, 180 °C bake for 5 minutes). This followed by the spin on and bake of an HSQ resist (3 000 RPM, 10 000 RPM/sec, 60 sec, 120 °C bake for 2 min followed by 200 °C for 3 minutes). A couple comments on the HSQ. First, this resist is very sensitive to the environment. If exposed to solvent or solvent fumes, it will react, and no longer work. If a glass pipet is used, it will react and not work. A plastic syringe (typically use 1 mL syringe) is used for drop casting. Additionally, it is a **negative** resist. This means the portions that are exposed are the portions that remain after development (in contrast to PMMA, which is a **positive** resist, where the exposed portions develop away). Additionally, the HSQ is sensitive to ambient building light (though this is a slow process in my experience), so it should be kept covered as much as possible (usually by wrapping sample holder in Al foil).

After deposition of resists, the substrate is marked in the same way as before with a scratch along the same edge, small scratches in the corners, and of Au colloids deposited on those corners before being loaded into the SEM. Extra care is needed with the Au colloid deposition, because the water that contains them will react with the HSQ, essentially

exposing it. It's important to make the drops extremely small and keep them in the sample corners, away from the devices.

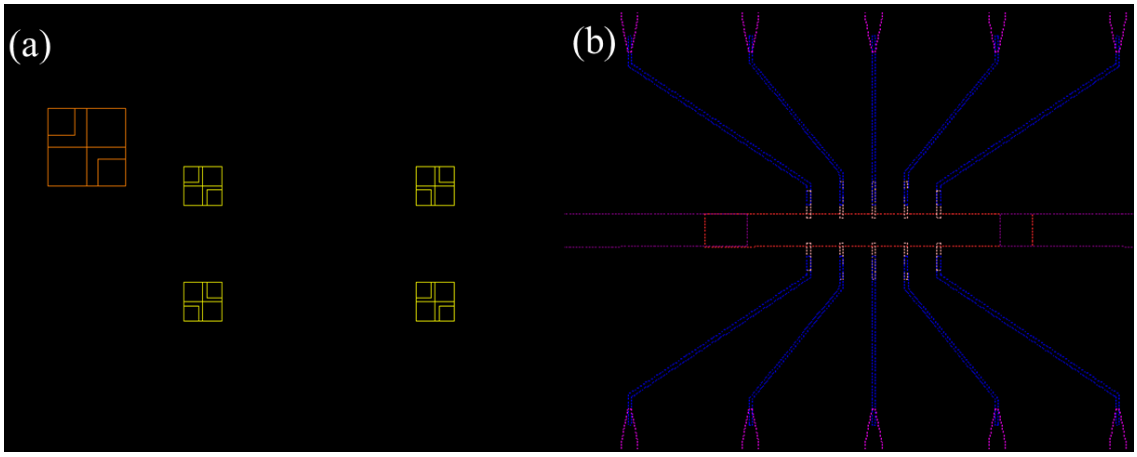

Figure A.3 *Second Graphene EBL Pattern*

CAD generated write files for the NPGS software for the second, graphene plateau alignment and write. (a) Shows the alignment file. The alignment cross overlays (line type: hidden) written in the first step are enclosed in boxes (line type: dashed) which will be scanned during the alignment step. (b) Zoomed in image of **Figure A.2**(a), showing the second layer write pattern consisting of the blue graphene hall bar, and the small pink graphene Hall bar legs.

Alignment and Pattern Writing. Since this is a second write that needs to be aligned to the first layer write performed above, we must align the sample very precisely. Using the X-T align feature of the SEM define the x-axis **using the same points as before**, and locate the origin point. Perform the X-Y focus plane procedure to map out the focal plane for the sample. After this, a two-stage alignment is performed, using the two sets of fiducials (alignment crosses, there are a large and small set), to take care of any lateral, magnification, or rotational offsets. This alignment is performed by specifying in the NPGS run file that the entity type is "Alignment" (followed by the second entity which is a "Pattern"). When run, the alignment windows (defined in the CAD file as a standard dashed

lines) will be scanned by the electron beam, with an overlay of the fiducial markers (defined by hidden lines), and these are repositioned on top of the correct imaged features. The first stage alignment is a "rough" alignment, and the second stage is a "fine" alignment performed using the same parameters of the first written layer. The alignment CAD is shown in **Figure A.3**(a), along with a zoom in of the full write file so that the second writing layer (the graphene bar) is visible **Figure A.3**(b). The second (yellow shapes) alignment step, has four windows which can be operated independently from each other during the alignment. This is done by placing each of the crosses and their respective scanning box in separate layers (4 total layers). The first layer is marked as "Start New Set" in the NPGS run file, while the following three layers are marked as "Windows." The parameters for the alignment are shown in **Table A.2**, while the second layer writing parameters are shown in **Table A.3**.

Table A.2 *Second EBL Alignment Parameters.*

Design Layer	Feature Color	Field Size[8]	Offset[9]	Mag.[10]	Spacing[11]	Config. Param.	Measured Current	Dose[12]
1	Orange	1.2	(0, 0)	100	508.88	-4	170	10
2-5	Yellow	0.4	(0, 0)	300	302.38	-7	21	20

[8] In mm (approximate)
[9] In μm
[10] Magnification
[11] Center to Center spacing, and Lines spacing, usually the same value
[12] In Counts

Table A.3 *Second EBL Write Parameters.*

Design Layer	Feature Color	Field Size[13]	Offset[14]	Mag.[15]	Spacing[16]	Config. Param.	Measured Current	Dose[17]
1	Red	0.4	(0, 0)	300	7.38	-7	21	130
2	Pink	0.4	(0, 0)	300	7.38	-7	21	130

Development and Etch. After exposure, the sample is developed in MF-319 for 2 minutes (again, if development is not finished, additional development time can help, though two minutes is typically sufficient) and rinsed in gently running DI H_2O. Make sure to check that the development was successful in an optical microscope. After development the PMMA and extraneous graphene is etched. This is typically performed on the ICP-RIE system (ETC04) located in the Nanotech West cleanroom (though in a pinch it could also be done in the lab-18 system in the NSL cleanroom, however, there is suspicion that this etch is too aggressive and damages the SiO_2; if needed the following parameters will work: 25 mTorr O_2, 50 W power, ramp up at 2 W/sec, etch for 4 minutes with 200 DCV, ramp down at 5 W/sec). The recipe used for the Nanotech West ICP-RIE etch is specified in Section A.1.3. No pump oil is needed for this etch. Etch time is 60 seconds, but if the plasma takes > 5 seconds to ignite, more time should be added, or a second shorter etch should be performed to account for this lost time.

[13] In mm (approximate)
[14] In µm
[15] Magnification
[16] Center to Center spacing, and Lines spacing, usually the same value
[17] Area Dose, in $\mu C/cm^2$

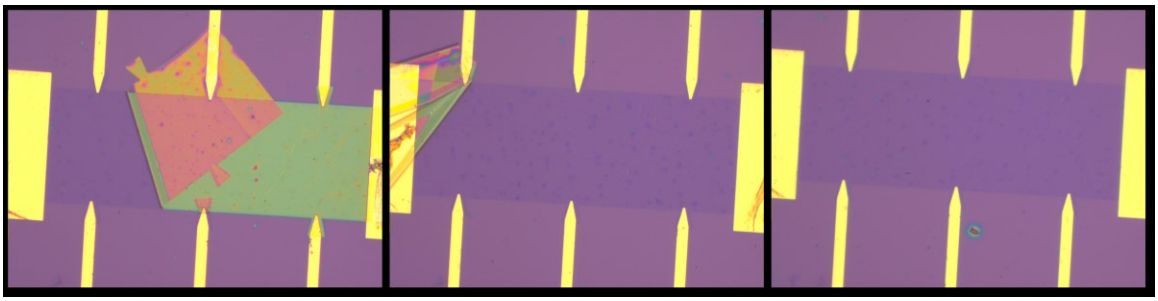

Figure A.4 *Failed HSQ Lift-Off.*

Image showing different states of lift-off on a 100 μm wide graphene device prepared for STM measurements. On the left, the resist barely lifted off at all. In the middle, the film mostly lifted off, but got stuck in the corner. In the right-most image the resist completely lifted off. In these images, the very small dark purple spots on the graphene are bilayer graphene. This particular set of samples was replaced by the supplier due to the higher than normal density of bi-layer graphene islands.

Lift-off. After etching, the purple colored SiO_2 substrate should be exposed (and visible) across the entire sample, except for the portion of graphene still protected by HSQ/PMMA. This should now be lifted off using another hot acetone soak for 3-5 hours (in a water bath). After this time, the sample should always be agitated lightly using a pipette in the acetone. Many times the remaining HSQ can get stuck on the edge, and then fails to lift off entirely (see **Figure A.4**). The agitation almost entirely solves this problem. An example of a completely successfully synthesized device (recently fabricated for Shawna Hollen at University of New Hampshire) is shown in **Figure A.5**.

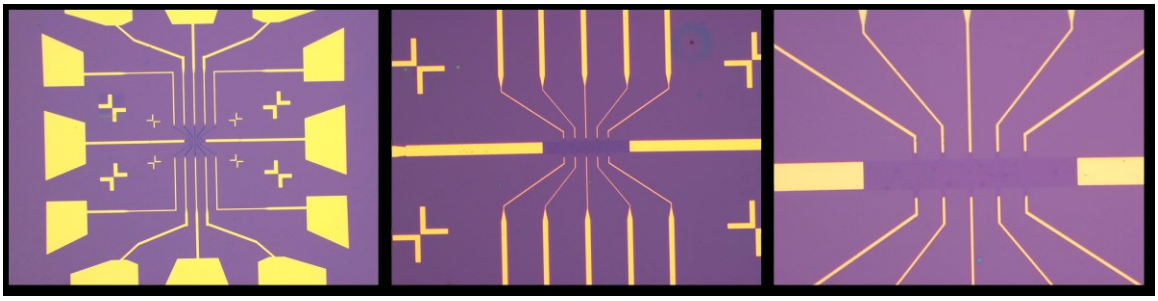

Figure A.5 Completed Graphene Device.

Optical micrograph images showing a recently fabricated graphene device at progressive zoom levels. The width of the device (electrode edge to electrode edge) is 1.1 mm, and the width of the graphene Hall device is 10 μm.

A.3 Exfoliated Device Fabrication

The fabrication of devices from exfoliated 2D materials is similar in many regards to the techniques described immediately above, however there are some critical differences which we will describe here. While exfoliated materials tend to be of a much higher quality, one of the advantages of patterning devices on substrate wide material (i.e. CVD grown graphene) is that the device can be fabricated anywhere on the substrate. For exfoliated materials on the other hand, the device must be designed and build around the exfoliated material, and the resulting device will likely be entirely unique, based on the shape of the exfoliated flake. This requires an extra alignment and device design step in the lithography process (though the etching step often is not needed). Additionally, often times additional lithography steps need to take place, such as the synthesis of a top gate (an additional step is needed for the dielectric deposition), or the two-stage Ti/Au & Au metallization steps used for germanane device synthesis described in **Chapter 3.** Here we will describe the typical process used for exfoliated germanane device synthesis.

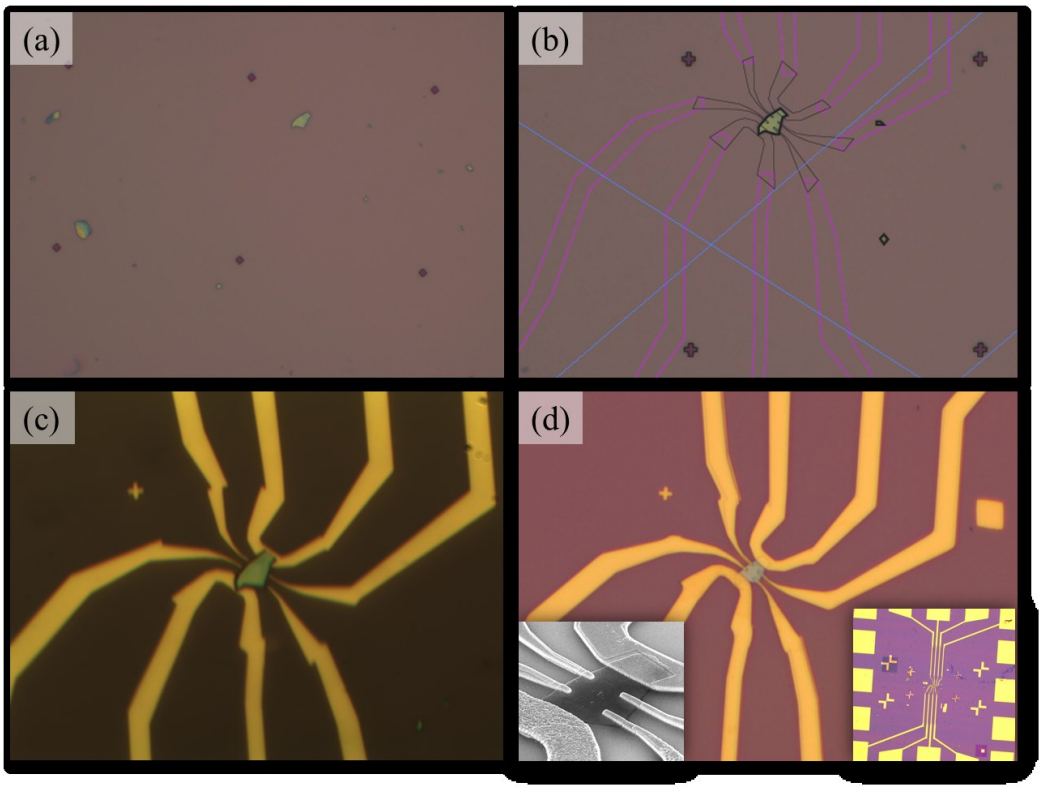

Figure A.6 *Germanane Device Synthesis.*

Optical micrographs of germanane devices during different portions of the process. (a) Immediately after alignment grid EBL and development. (b) The same shown with the designed device overlaid. Note the separation of layers by shape and color. The fine electrodes which will touch the GeH device will be dosed differently from those not touching the device. The thicker Source/Drain electrodes also are dosed differently. (c) Device after the first Ti/Au layer deposition. Here, none of the Ti/Au metal touches the device itself. (d) Final device with the additionally pure Au metal deposition, which does make contact to the flake. (left inset) SEM image of the device. (right inset) Optical micrograph of the full write field.

A.3.1 *Alignment Grid and Device Design*

Here we describe the additional alignment step necessary for the fabrication of exfoliated devices.

Exfoliation. The exfoliation process is typically carried out by collaborators (for the case of germanane flakes, Nick Cultrara or Fan Fan from Josh Goldberger's group), and so is not described here. After the actual exfoliation, thin and appropriately sized flakes (with

lateral dimensions of typically 5-10 μm), are located and characterized via optical microscopy and atomic force microscopy. The general location with respect to some larger reference point—typically a substrate corner—must be provided.

Resist Deposition and Preparation. Similar to the graphene Hall bar, we use the same resist stack and recipe, but with one exception: **Germanane is only stable up to 75 °C, so the baking recipe for the resists is modified slightly. The temperature for both bakes is restricted to 50 °C, the copolymer is baked for 3 hours, and the PMMA is baked for 30 minutes.** If the copolymer is not baked long enough to evaporate the solvent in the resist, during the PMMA bake the copolymer will shrink, and the result will be cracks in the resist stack, which can create shorts after the metal deposition and lift-off steps. After resist deposition, the samples corners and edges are marked, and Au colloids deposited as with graphene devices.

Alignment Grid Write. Using the same procedure as specified in the graphene device section for focusing and aligning to the sample, we write a 1 mm^2 grid in the general location of the flake of interest. This grid pattern has small cross hairs (~2 μm along each arm), spaced by 50 μm. Every five markers (spaced at a distance of 250 μm) the cross hairs are enclosed by boxes, and there are large, 20 μm^2 squares in the four corners of the image. The parameters for these different elements are provided in **Table A.4**, an optical micrograph of this grid written around a GeH flake is shown in **Figure A.6**(a), and an image of the CAD file written is shown in **Figure A.7**(a). The usual development procedure is followed for this pattern, however no metallization or lift-off is yet performed.

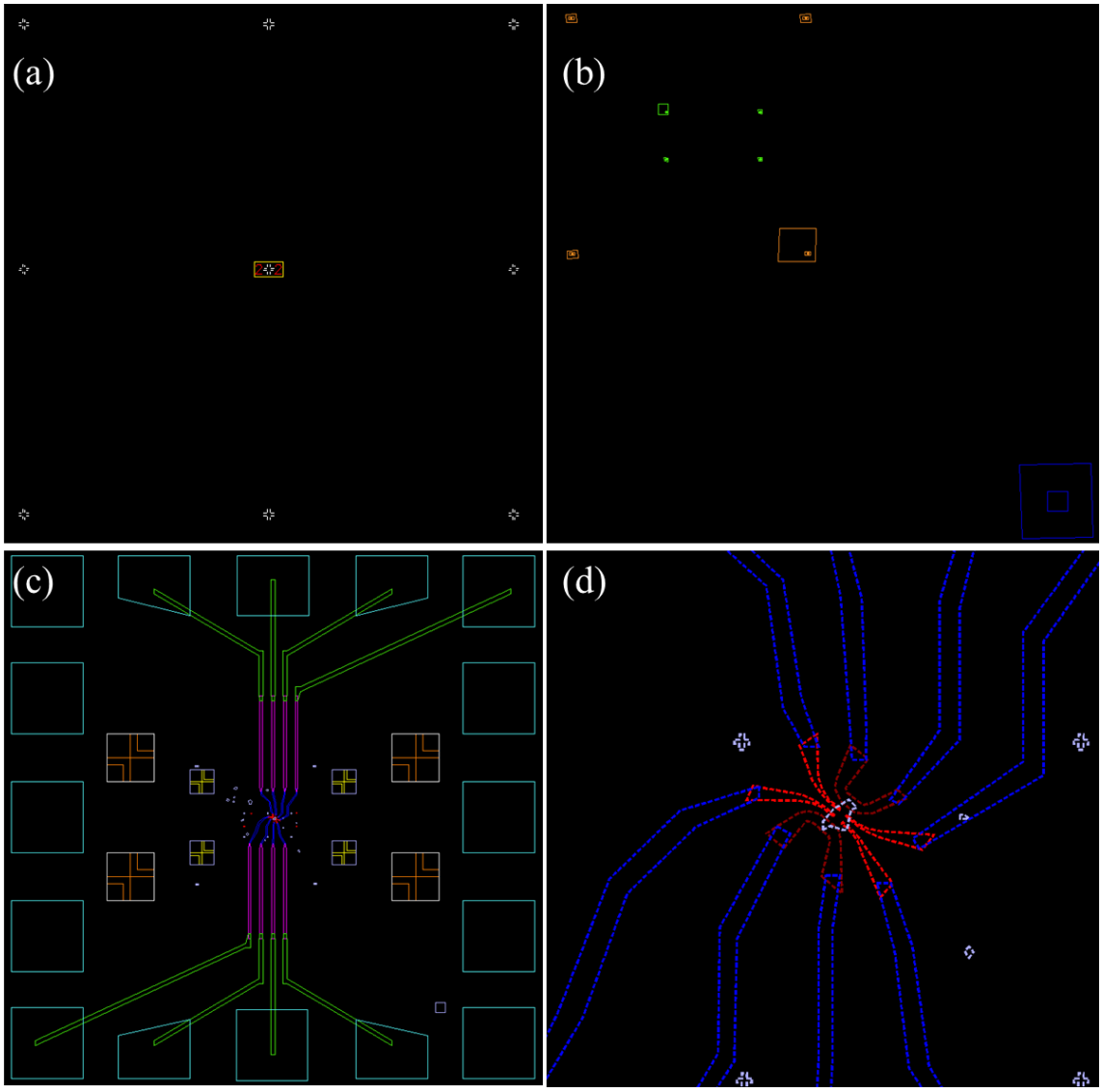

Figure A.7 *CAD Files for Exfoliated Devices.*

(a) CAD file showing a portion of the alignment grid written, with a distance of 50 μm between crosshairs (the number portion of the write was not used). (b) Alignment file used to align to the previously written alignment grid. (c) Example of customized contact pattern written around a GeH flake. (d) Zoomed in region of the pattern close to the GeH flake.

Pattern Design. The grid deposited here allows us to register the location of the GeH flake precisely on the substrate. We know where we wrote the grid, and now we can look and see where the flake falls in this grid. Optical micrographs are taken of the flake in the grid

at different magnifications (typically 50x, 20x, and 5x). These are then used to design the device around the specific flake. Typically I use Adobe Illustrator for this process, though it is possible to do in most CAD softwares. The images are loaded into the design software, and scaled appropriately (the cross hairs are spaced by 50 μm, and I usually let 1 μm = 1 mm in my designs). Once scaled correctly, the electrodes can be designed directly around the flake. For one example see **Figure A.6**(b). Typically, the electrodes can have widths down to 200-250 nm using this process (though I have been able to write down to 150 nm features after some parameter adjustments), though the end source/drain electrodes are typically written wider, at 0.5-1 μm. Spacing between the electrodes is typically maintained at 1 μm, due to the undercut created by the copolymer. Typically, only the electrodes, and the next layer outward are designed specifically for a device. The subsequent layer is adapted from the general Hall bar pattern developed in the graphene section.

Table A.4 *Alignment Grid Write Parameters.*

Design Layer	Feature Color	Field Size[18]	Offset[19]	Mag.[20]	Spacing[21]	Config. Param.	Measured Current	Dose[22]
1	White	1.2	(0, 0)	100	22.13	-6	43	130
2	Yellow	1.2	(0, 0)	100	22.13	-6	43	4
4	Blue	1.2	(0, 0)	100	22.13	-5	86	100

[18] In mm (approximate)
[19] In μm
[20] Magnification
[21] Center to Center spacing, and Lines spacing, usually the same value
[22] Area Dose, in $\mu C/cm^2$, for layers 1 and 4, but Line dose, in nC/cm for layer 2

A.3.2 *Flake Device Writing*

First Step Electrode Writing. After the designing is completed, this design can be exported to a .dwg file type, and imported into the NPGS CAD file. Typically, the imported shapes must be selected and exploded (edit > selection edit > explode shapes), and have the line type changed to "dashed" to be written correctly. This first layer will be a Ti/Au stack. We found that having Ti in contact with the GeH flake increases contact resistance, but the Ti seeding layer is helpful to keep the metal attached to the substrate. Consequently this write is performed on the contact leads all the way up to the GeH device, but then stopped (**Figure A.6**(c)). The electrodes on top of the GeH flake are written in the subsequent step **Figure A.6**(d). The alignment and write is performed as before, but in this case the alignment is done to the grid previously deposited, in a three-step alignment process[23]. The alignment and pattern write files are shown in **Figure A.7**(b)-(d)**,** and the parameters are recorded in **Table A.5** and the layers **Table A.6**. After writing, the same development and metal deposition procedure is used, but this time a metal stack of Ti(1 nm)/Au(25 nm) is used. Lift-off is performed in **room-temperature** acetone (to prevent amorphization in hot acetone), with subsequent IPA and DI H_2O rinses.

[23] The first alignment box in the 2nd and 3rd stage alignments are slightly larger and offset from the overlay. This is to account for the offset needed between the two layers, and keeps the alignment marker still in the scan range.

Table A.5 *Flake Alignment Parameters*

Design Layer	Feature Color	Field Size[24]	Offset[25]	Mag.[26]	Spacing[27]	Config. Param.	Measured Current	Dose[28]
1	Blue	1.2	(0, 0)	100	796.51	-5	86	30
3-6	Orange	0.6	(0, 0)	200	399.56	-7	21	30
7-10	Green	0.25	(0, 0)	500	48.68	-7	21	30

Table A.6 *Flake Write Parameters*

Design Layer	Feature Color	Field Size[29]	Offset[30]	Mag.[31]	Spacing[32]	Config. Param.	Measured Current	Dose[33]
1	Red	0.25	(0, 0)	500	4.43	-7	21	150
1	Dark Red	0.25	(0, 0)	500	4.43	-7	21	130
2	Blue	0.25	(0, 0)	500	8.85	-5	86	150
4	Purple	0.6	(6, -6)	200	22.13	-4	170	160
4	Yellow	0.6	(6, -6)	200	22.13	-4	170	160
5	Green	1.2	(16.5, -16.5)	100	44.25	-3	340	180
5	Orange	1.2	(16.5, -16.5)	100	44.25	-3	340	180
6	Light Blue	1.2	(16.5, -16.5)	100	44.25	0	340	200

Second Step Electrode Fabrication. After the first step electrodes are written, PMMA/Copolymer is spun on again, baked (at 50 °C again), and marked, all as previously. The second layer is written in the exact same way as the first layer, except now the electrodes will extend on the GeH, and in this case, we align to the Ti/Au fiducials written during the first step. The alignment is performed as in Section A.2.3, and the write is performed using the same parameters in **Table A.6** as the first layer write. Development is

[24] In mm^2 (approximate)
[25] In µm
[26] Magnification
[27] Center to Center spacing, and Lines spacing, usually the same value
[28] In Counts

[29] In mm^2 (approximate)
[30] In µm
[31] Magnification
[32] Center to Center spacing, and Lines spacing, usually the same value
[33] Area Dose, in $\mu C/cm^2$

performed as before, and the metallization is only Au (50-100nm), with lift-off again occurring in room-temperature acetone. A completed device is shown in **Figure A.6**(d).

A.4 Resolution Limited Electrodes

First, I clarify the statement "resolution limited electrodes." By this I mean the size and spacing of the electrodes are limited by a combination of our SEM capabilities, and chosen resist capabilities. EBL electrodes have been made with smaller feature sizes than those achieved here, but we believe that those achieved here are at the limits of our resists/SEM. We attempted to reach these limits in an effort to place electrodes on exfoliated germanane flakes, such that they make contact to a single-layer of the flakes, rather than different layers, in order to isolate transport through a single layer. Here we discuss the effect of different writing parameters on the possible electrode size and spacing, as well as the optimization of these different parameters.

- **Bilayer vs. Single Layer Resist** – For the above processes, we only discussed copolymer/PMMA resist stacks. This is because the undercut produced by the copolymer (shown schematically in **Figure A.1**) helps dramatically for the lift-off process of thicker metal depositions. However, this works against us in the attempt to reach resolution limited EBL. When features are spaced too closely together, the entire copolymer is etched away, and the PMMA over-layer can distort **Figure A.8**(a). For our copolymer/PMMA stack, we were able to achieve 65 nm wide electrodes, with a pitch of 500 nm. Examples of this are shown in **Figure A.8**(b). To reduce the electrode spacing further, we switched to a single-layer PMMA resist, which can cause more issues with lift-off, but allows production of smaller electrodes. Lift-off was improved by depositing thinner a thinner metallic stack of Ti(1 nm)/Au(25 nm). The highest resolution we were able

to achieve using **PMMA** was 25 nm wide, with an 80 nm pitch. However, the results for this were often inconsistent, so slightly larger dimensions were used (see **Figure A.8**(c)-(f)).

- **Current** – The current used during writes determines the width of the beam. So for smaller electrodes, smaller currents of **21 pA** were used. We found that further reduction of this value made no difference, other than increasing the write time.

- **Acceleration Voltage** – This parameter makes a large difference in the achievable electrode widths. Higher voltages, correspond to greater electron energies and greater penetration depth. This means that the electrons go further before scattering, and reduces the parasitic dosing of the electrodes, preventing overdosing directly around the electrode locations. We found best results with **30 kV** acceleration voltage (the highest achievable in our system). Many commercially designed EBL systems use voltages of 100-200 kV allowing higher definition feature writes.

- **Dosing** – The dosing of the electrodes is correlated with the current, acceleration voltage, pitch and the width used. In particular, for higher voltages a higher dosing must be used (since the PMMA is receiving less concentrated parasitic dosing). At 10 kV, typical dosing is around 100-200 $\mu C/cm^2$, while for 30 kV we were using values clower to 400-600 $\mu C/cm^2$. As electrodes are spaced closer together, the amount of dosing must be decreased (due to increased parasitic dosing effects), and for wider electrodes the dosing is decreased (also due to an increased in parasitic dosing). Both of these effects could be summed up as "pattern density." The denser the amount of writing, the lower the dosing needed.

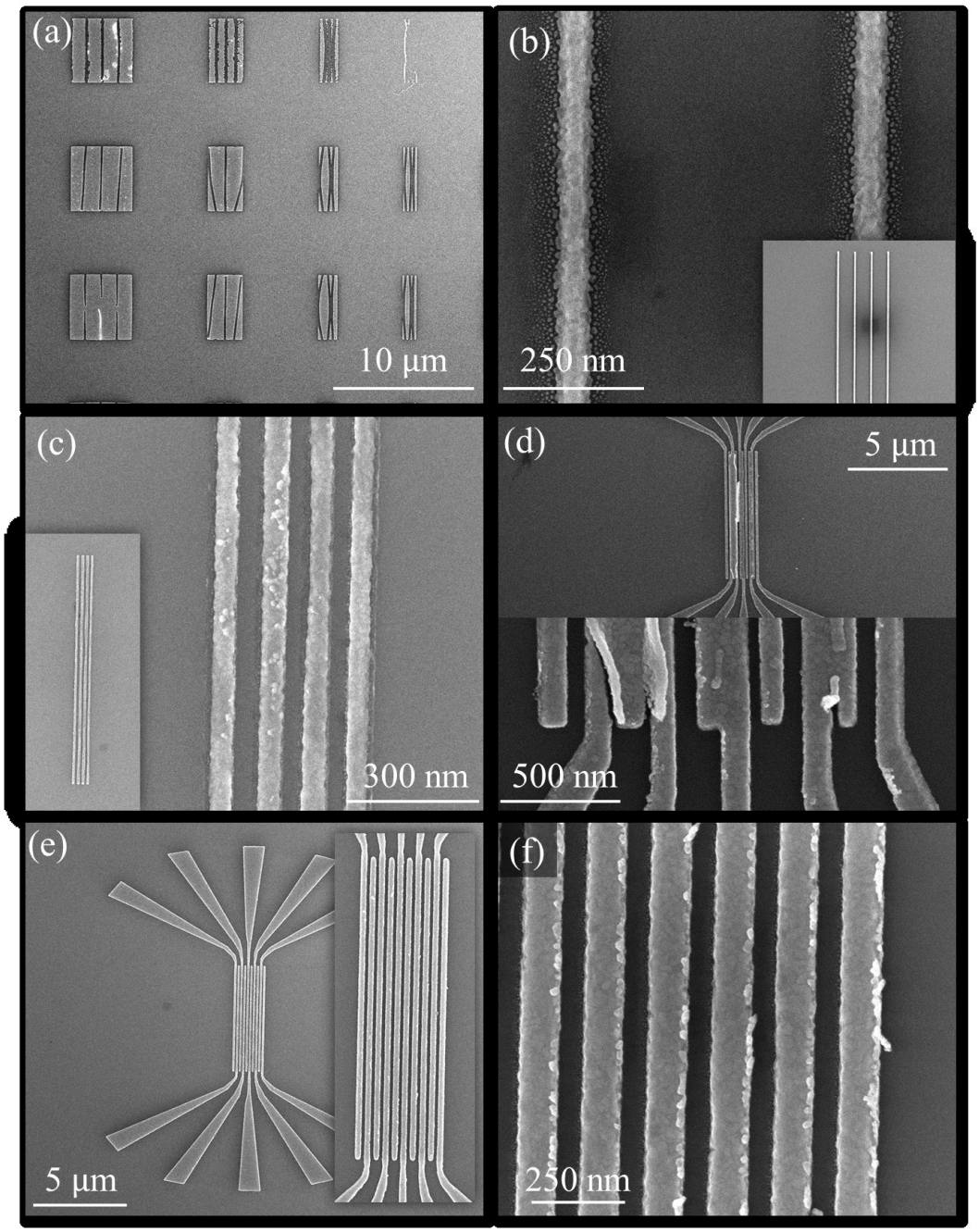

Figure A.8 *Resolution Limited Electrodes*

SEM images of metalized EBL electrodes written under different conditions. (a) Demonstration of issues with electrodes written in bi-layer resist (b) best written using bi-layer resist. 65 nm wide, 500 nm pitch. Inset: zoomed out demonstrating uniformity. (c) Best using only PMMA. 55 nm wide, 115 nm pitch. Inset: zoomed out demonstrating uniformity. (d) Larger array written in a pattern, showing issue that rises with the write order. (e) Array in pattern, using better ordering. 10 electrodes, 100 nm wide, 170 nm pitch. Inset and (f) show zoomed in views of the same electrode pattern. Larger array width and pitch were used to improve writing consistency.

- **Write Order –** This is a variable that we did not realize was an important parameter for a while. By "writing order," we mean the order in which the electrodes are written. This was discovered when creating a larger electrode arrays, and including it in a more realistic pattern. **Figure A.8**(d) shows an example of an electrode array written in a more-or-less random order, while **Figure A.8**(e)-(f) shows electrodes written in order from left to right. We believe this has to do with charging effects from the substrate redirecting the electron beam slightly. The magnitude of this effect is small, so it's only noticeable in this type of edge case of extremely small and dense pattern writing. In the orderly left to right writing, the charging effects are more consistent during the write, so a more ordered pattern is written. In the random case, the charging effects are highly inconsistent, resulting in erratic deflections of the beam.

While there are likely other considerations that may need to be made for these high resolution electrodes, we found these to be the most effective parameters to manipulate in our particular writing protocol. The most consistent, highest resolution, highest quality results that were attained are shown in **Figure A.8**(e)-(f). These electrodes were written in PMMA from left to right at 30 kV, 21 pA, and a dosing of 410 $\mu C/cm^2$. The result is a pitch of 170 nm and width of 100nm, with a deposition of 25 nm of Au. The aforementioned development and lift-off procedures were used here.

Appendix B: Templated MoS_2 Growth

B.1 SiN Stencil Synthesis

The SiN stencils are etched from amorphous, silicon-rich, transmission electron microscopy membranes purchased from Ted Pella, Inc. These membranes are produced by back-etching a 750 × 750 μm^2 window centered on a circular Si support frame which is 3 mm in diameter. In order to use a focused ion beam (in our case a FEI Helios Nanolab 600 dual beam focused ion beam (FIB) and scanning electron microscope (SEM)), the surface of the SiN must be coated with a conducting film, because the native SiN is very insulating. This insulating nature will cause issues during the write due to charging effects. We use a thin film of 50 nm of Ag as a conducting layer, deposited via electron beam deposition.

In order to make these membranes easier to handle during this metal deposition step (as well as all future processing steps), they are first mounted on a larger Si substrate (~ 1 cm^2) using a small bit of crystal bond. After mounting and metal deposition, the top surface of the membrane needs to be electrically connected to the Si substrate so the charge from the FIB has somewhere to go. This is done using a very small amount of silver paint.

Once mounted and electrically connected, the film is ready to be mounted into the FIB for mask writing. Using standard FIB operating procedure, the mask is brought to the 4.1 mm, focused, and subsequently adjusted to the eutectic height for rotation to the 52°

angle needed for FIB scanning and writing. The FIB beam should then be focused and aligned to the SEM so that the writing location can be determined by the non-etching SEM imaging, and then patterned by the FIB without any additional offsets.

The Nabity NPGS program is used for writing our FIB patterns. To use this program for FIB writing the "Magnification Scale" setting must be changed in the project used. To change this value, one must go to options > system files > pg.sys. Once this dialog is opened the option "Magnification Scale" should be entered as 145 000. For SEM patterning the value is 179 000. This value is used by NPGS to convert the CAD shapes into the correct size for writing.

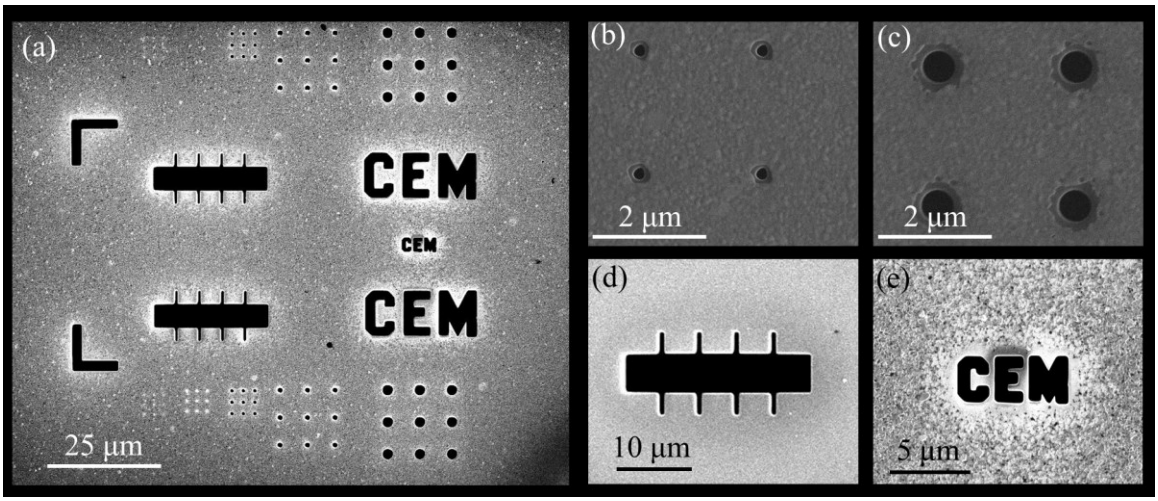

Figure B.1 *SiN Mask FIB Images.*

FIB images of SiN mask after FIB writing. (a) Full write field. (b) Zoomed in region of 100 nm diameter dots. (c) Zoomed in image of 500 nm dots. (d) Zoomed in image of Hall bar. (e) Zoomed in image of small CEM writing.

The FIB writing is conducted at 30 kV, with different currents and dosing for different shapes. These specifications are shown in **Table B.1**. The center-to-center distance and

line spacing used here was 10 nm, and the magnification for our writes was 1000 (corresponding to a total write field of 125 μm). The full standard mask written is shown in **Figure B.1**(a), as well as several zoomed in images showing more detail of portions of the written mask (**Figure B.1**(b)-(e)).

Table B.1 *SiN FIB Write Parameters.*

Feature[1]	**Current (pA)**	**Dosing ($\times 10^3$ μC/cm^2)**
100-200 nm dots	28	500
0.5-1 μm dots	460	400
2-5 μm dots	2 800	250
Fiducials	2 800	250
Hall Bar[2]	2 800	200 (Hall Bar) 250 (Voltage Probes)
CEM text	2 800	250
Small CEM text	460	400

After the writing is finished, the mask needs to be removed from the Si base substrate, and the Ag pain needs to be removed. These can both be accomplished at the same time by soaking in acetone for 2-3 hours. After the soak, the mask should be gently rinsed (via light stirring) in a clean beaker of acetone (to remove any remaining Ag paint or crystal bond), IPA, and then very lightly dried using N_2. Rough handling of the SiN membrane can easily result in a broken membrane.

[1] Features shown in **Figure B.1**

[2] 5 × 25 μm bar, with 1 μm wide hall probe widths

B.2 Preparation and Deposition of Mo Films

B.2.1 *SiN Mounting*

The sapphire substrates onto which the Mo is deposited are epi-ready, c-axis sapphire substrates cleaved from 0.432 mm thick, single-side-polished HEMCOR wafers purchased from Alfa Aesar (#45019). They are pre-annealed before Mo deposition for one hour at 1000 °C in air. After this annealing process, the SiN membrane must be mounted membrane side down. This is accomplished using the utmost care. The stencil must be held in place securely for the deposition, without blocking the membrane. While several methods for this were attempted, we found the best solution was to place the SiN/Sapphire sample on a glass slide and to place a small strip of Al foil with a vertical slit cut in the center (roughly 1.5 × 5 mm) over top of the SiN/Sapphire. This foil is then held securely in place via kapton tape attached to the glass slide. The foil puts enough pressure on the SiN membrane that it does not move during the deposition. This is shown schematically in **Figure B.2**. After the SiN membrane is secured, it can be loaded normally into the lab-18 thin film deposition system.

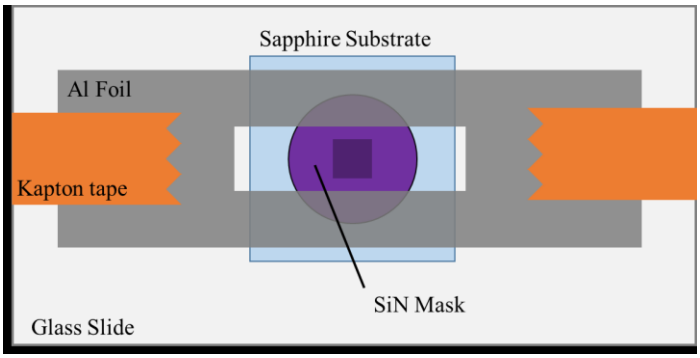

Figure B.2 *Securing SiN Membrane for Deposition.*

Schematic diagram of showing how the SiN membrane stencil is held securely in place during the Mo metal deposition.

B.2.2 *Mo Deposition*

There are several things to take note of when using electron beam (e-beam) evaporation to deposit Mo thin films. First, generally we are trying to deposit very thin films (< 1 nm) reliably. The lab-18 system is not really designed for this type of deposition, which causes some complications. In particular, the quartz crystal monitor typically used to detect the deposited material thickness (and the rate) is far from the e-beam source (~ 2 feet), close to the sample. This is excellent for thicker depositions, but for this type of deposition, where we are trying to achieve deposition rates of ~ 0.1 Å/sec, this is rather difficult because of the fact that this small deposition rate is very close to the resolution of the monitor at this distance. We attempt to overcome this issue by installing a second crystal monitor much closer to the e-beam source (~6 inches). This is a quarter of the distance, so the material flux hitting the new crystal monitor (goes as distances squared) is nearly a factor of 16 larger, making this crystal much more sensitive to the amount of material being deposited.

Both quartz crystals are replaced before Mo depositions are started to further improve the monitor readings.

For many sensitive deposition, this works very well. However, Mo has a high melting temperature of 2,600 °C and takes considerable power (18-25 % power on the lab-18) to deposit. This has the effect of quickly heating up the chamber, and in particular, this crystal monitor which is sitting quite close to the e-beam source. It is well known that crystal monitors, are strongly effected by temperature, and generally a changing temperature causes considerable accuracy issues in the reading. This is a definite problem that we have experienced. If several depositions are completed in a row, we observe the chamber temperature raise by nearly 10 °C (at a thermocouple near the sample, far from the source and the 2nd added crystal monitor). This can cause the recorded crystal thickness to vary as much as 40% between a starting deposition and a deposition once the chamber has heated up. To help combat this, we limit ourselves to 2 depositions in a row before letting the chamber cool back down (for 1-2 hours).

Another challenge with these Mo depositions is that for the thicknesses we are depositing, the shutter is open for a relatively small amount of time. When the shutter is opening and closing, the deposition is greatly perturbed, causing the amount and rate of material deposition to vary greatly during this time. At short deposition times, this opening and closing takes up a significant fraction of the total deposition time (as much as 10%). Compared to much longer deposition times, this causes inconsistencies in the deposition thickness, and makes it quite difficult to determine how much material has been deposited reliably. This is one of the reasons we cite only deposition times in the main text.

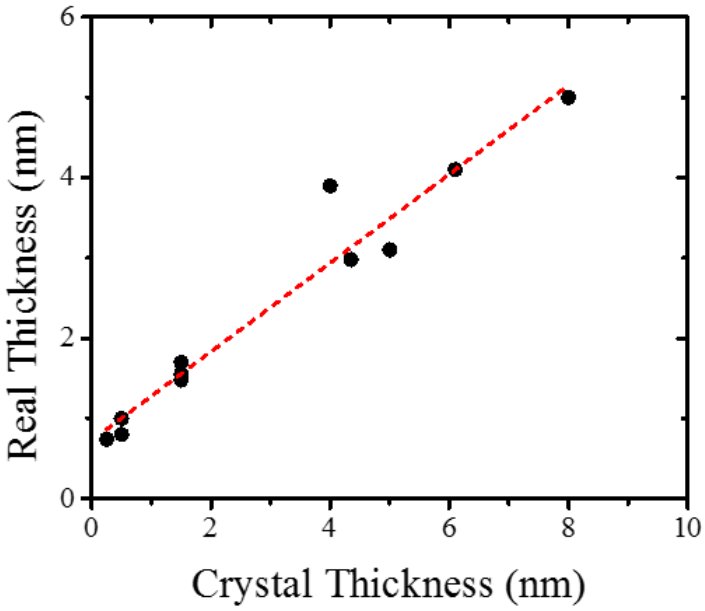

Figure B.3 *Molybdenum Depositions.*

Scatter plot of the measured Mo film thickness (via AFM) versus the thickness recorded by the crystal monitor for films thicker than 1.5 nm. A best fit line is plotted as well, which has a slope of 0.55 ± 0.04 and an intercept of 0.73 ± 0.15 nm.

A second reason that only deposition times are specified, is that for the thicknesses we're talking about (typically < 1.5 nm), it is very difficult to find locations to measure the film thicknesses in the AFM because these films have no optical contrast with the underlying substrate (unlike the sulfurized MoS_2, which is quite visible). Because of this, the crystal was calibrated at thicker higher depositions. We did many Mo depositions over a period of several weeks using the same crystal calibration factor (466.2 for the original crystal monitor, and 45.5 for the new, closer monitor), and the same deposition rate (0.1 Å/sec). After deposition, the actual thickness of the many films was measured. This data (crystal thickness of the 2nd, new monitor) is plotted along with a best fit line is plotted in **Figure B.3**. The slope of the best fit line is 0.55 ± 0.04, while the intercept is 0.73 ± 0.15

nm. The significance of the slope, is that it nominally tells us a new "ideal" crystal calibration factor (0.55 × 45.5 = 25.0), however for consistency in the deposition rate used between all of our depositions, we continue to use the old factor and just calculate the real thickness from the crystal reading using the fitted line. The significance of the intercept is a little more confusing. This implies that if 0 nm of material is deposited according to the crystal monitor, we still in reality deposited 0.73 nm of material. We believe that this "offset" is an effect which arises from shutter opening and closing. For the thicker, more standard depositions (10-100 nm) done in the lab-18 system, this small offset causes little trouble, but for our very thin depositions, this can cause a lot of confusion.

There are several challenges in doing these very fine depositions in the lab-18. To combat these we have implemented a few protocols.

1. **Consistency –** While this is important in any synthesis protocol, for these depositions it is critical to achieve reliable results. To this end we consistently use the same crystal calibration factors **(1st : 466.2/ 2nd : 45.5)**, and we use a deposition rate of **0.1 Å/sec** (via the 2nd monitor).

2. **Quartz Crystals –** These are replaced prior to each Mo deposition run (typically a day's worth of Mo depositions). This increases the accuracy of the rate and thickness readings.

3. **Timed depositions** – Since the thickness is extremely difficult to know or even extrapolate for these thin films, we do depositions based on time. Since we maintain the same rate, and crystal calibration, this is the most reliable way we have found to keep track of our depositions (though it is still inconsistent at times).

4. **Heat Limit** – Since the crystal monitor is strongly affected by the temperature, we do only two depositions in a row, stopping if the sample thermocouple reads above 25 °C (which would indicated a much higher crystal temperature). If we want to do more depositions, we wait 1-2 hours for the chamber to cool first.

5. **Rate Stabilization –** There are two shutters in the system. One right above the e-beam source (between the source and the crystal monitors), and one right below the sample. The Mo is slowly heated up until it is near the deposition temperature, and then the first shutter is opened, allowing us to get a reading from the crystal monitors. Due to the heat being generated, the crystal monitor reading varies wildly for up to 1 minute, then begins to stabilize. We make sure the deposition rate has been stable for a full minute before opening the second shutter. The total time between opening the first shutter, tuning the power to get the appropriate deposition rate, and waiting on a stabilized rate is roughly 5 minutes total.

While these protocol do not entirely solve the problems related to this deposition, they do go a long way toward making it more consistent. Our methods for Mo deposition could be improved greatly by moving to a different, more stable system or deposition mode (such as a sputtering or molecular beam epitaxy (MBE) system).